Climate engineering with stratospheric sulphate aerosol : development and application of a global atmosphere-aerosol model for studying potential efficacy and impacts

Christoph Kleinschmitt

Dissertation

submitted to the
Combined Faculties of the Natural Sciences and Mathematics
of the Ruperto-Carola-University of Heidelberg, Germany
for the degree of
Doctor of Natural Sciences

as well as to the
Doctoral School of Environmental Science of Ile-de-France (ED 129)
of the Pierre and Marie Curie University, Paris VI, France
for the degree of
Doctor of the Pierre and Marie Curie University

(International Cotutelle Doctorate)

Put forward by
Christoph Kleinschmitt
born in: Mainz
Oral examination: 21 December 2017

Climate Engineering with Stratospheric Sulphate Aerosol: Development and Application of a Global Atmosphere-Aerosol Model for Studying Potential Efficacy and Impacts

Thesis Committee:

Ulrike Lohmann	Referee
Hervé Douville	Referee
Thierry Fouchet	Examiner
Ulrich Schwarz	Examiner
Olivier Boucher	Thesis Supervisor
Ulrich Platt	Thesis Supervisor

Climate Engineering with Stratospheric Sulphate Aerosol: Development and Application of a Global Atmosphere-Aerosol Model for Studying Potential Efficacy and Impacts

The enhancement of the stratospheric sulphate aerosol layer has been proposed as a method to abate the global warming caused by anthropogenic greenhouse gas emissions. In this thesis we present a newly developed global atmosphere-aerosol model, evaluate its performance against observations, and apply it to study the effectiveness and impacts of this possible form of climate engineering. We find that the achievable cooling effect per injected sulphur mass unit may decrease more drastically for larger injections than previously estimated and that injections at higher altitude or over larger areas do not result in a stronger cooling. The effectiveness of the method may therefore be rather limited, at least when using tropical injections of sulphur dioxide as in our model experiments. In addition, there are several potentially harmful side effects, such as stratospheric heating due to absorption of radiation by the aerosol causing strong perturbations in atmospheric dynamics, composition, and high-level clouds. Furthermore, we find that the radiative effects of stratospheric aerosol injection and marine cloud brightening, another proposed geoengineering technique, would be largely additive and complementary when applying them together. This might allow the design of portfolio approaches to achieve specific climate goals and reduce unintended side effects of climate engineering.

Climate Engineering mit stratosphärischem Sulfataerosol: Entwicklung und Anwendung eines globalen Atmosphären-Aerosol-Modells zur Untersuchung der möglichen Wirksamkeit und Auswirkungen

Die Verstärkung der stratosphärischen Sulfataerosolschicht wurde als eine mögliche Methode vorgeschlagen, um die durch anthropogene Treibhausgasemissionen verursachte globale Erwärmung zu bekämpfen. In dieser Arbeit präsentieren wir ein neu entwickeltes Atmosphären-Aerosol-Modell, evaluieren es anhand von Beobachtungen und verwenden es zur Untersuchung der Wirksamkeit und Auswirkungen dieser möglichen Form von Climate Engineering. Wir stellen fest, dass der erreichbare Abkühlungseffekt pro injizierter Schwefelmasseneinheit für größere Injektionen stärker abnehmen könnte als bisher vermutet und dass Injektionen in größerer Höhe oder über größeren Gebieten keine stärkere Kühlwirkung hätten. Die Wirksamkeit der Methode könnte sich daher als relativ begrenzt erweisen, zumindest im Fall der von uns simulierten tropischen Injektionen von Schwefeldioxid. Zudem gäbe es mehrere, möglicherweise schädliche Nebenwirkungen, wie eine Erwärmung der Stratosphäre aufgrund von Strahlungsabsorption durch das Aerosol, die zu Störungen von Atmosphärendynamik, chemischer Zusammensetzung und Cirruswolken führen würde. Außerdem stellen wir fest, dass die Strahlungswirkung stratosphärischer Aerosolinjektionen und diejenige der Aufhellung von Wolken über dem Ozean, einer weiteren vorgeschlagenen Form von Climate Engineering, im Fall einer gleichzeitigen Anwendung weitgehend additiv und komplementär wären. Dies könnte die Entwicklung von Portfolioansätzen ermöglichen, um spezifische Klimaziele zu erreichen und unerwünschte Nebenwirkungen von Climate Engineering zu reduzieren.

Ingénierie climatique avec des aérosols stratosphériques de sulfate : Développement et application d'un modèle global atmosphère-aérosol pour l'étude de l'efficacité et des impacts potentiels

L'augmentation artificielle de la couche stratosphérique d'aérosol de sulfate a été proposée comme méthode pour réduire le réchauffement climatique causé par les émissions anthropiques de gaz à effet de serre. Dans cette thèse, nous présentons un modèle global atmosphère-aérosol nouvellement développé, évaluons sa performance par rapport aux observations et l'appliquons pour étudier l'efficacité et les impacts de cette forme possible d'ingénierie climatique. Nous trouvons que l'effet de refroidissement réalisable par unité de masse de soufre injectée peut diminuer de façon plus drastique qu'estimé précédemment pour des taux d'injection élevés et que des injections à plus haute altitude ou dans des régions plus grandes n'entraînent pas un refroidissement plus fort. L'efficacité de la méthode pourrait donc être plutôt limitée, tout au moins dans les cas d'injections tropicales de dioxyde de soufre que nous avons modélisées. Par ailleurs, il existe plusieurs effets secondaires potentiellement nocifs, tels que le chauffage stratosphérique dû à l'absorption de rayonnement par l'aérosol provoquant de fortes perturbations dans la dynamique atmosphérique, la composition chimique de la stratosphère et les nuages hauts. Enfin, nous trouvons que les effets radiatifs de l'injection d'aérosol stratosphérique et de l'éclaircissement des nuages marins, une autre technique de géoingénierie proposée, seraient largement additifs et complémentaires lors de leur application parallèle. Cela pourrait permettre de concevoir un port-folio d'approches pour atteindre des objectifs climatiques spécifiques et réduire les effets secondaires indésirables de l'ingénierie climatique.

Contents

1 Introduction

1.1 Climate change and the need for mitigation

The climate of the Earth has always been changing. But over the last decades the rate of warming has reached an unprecedented level. The observed increase in global mean near-surface air temperature has numerous effects, e.g. the melting of sea ice, polar ice sheets, and glaciers, sea level rise, change of precipitation patterns, and an increasing frequency of a range of extreme weather events, with probably serious consequences for humans and ecosystems. Scientists have collected overwhelming evidence that the current global warming is mainly caused by human activities and related first of all to the emission of greenhouse gases (GHGs) [IPCC, 2013]. Carbon dioxide (CO_2) is the most important of them and (focusing on anthropogenic sources) is mostly emitted through burning of fossil fuels. However, methane (CH_4), nitrous oxide (N_2O), halocarbons (halogenated carbon compounds), and ozone (O_3) also have a considerable share in the total anthropogenic radiative forcing. Another important impact of CO_2 besides its greenhouse effect is ocean acidification, which has a negative though uncertain effect on many marine organisms.

In order to mitigate global warming, it is necessary to reduce the emissions of such GHGs. But this mitigation process requires in particular major changes in the global energy supply system, which is still mainly based on fossil fuels. Despite the technological and political challenges involved, a vast majority of the world's states engaged to take the required actions to keep global warming below 2 °C at the conference of the parties (COP) that was held in Paris in 2015. They even agreed to pursue "efforts to limit the temperature increase to 1.5 °C above pre-industrial levels, recognizing that this would significantly reduce the risks and impacts of climate change". For staying below 2 °C warming until the end of the 21st century with a probability of 50 %, the total cumulated CO_2 emissions since 1870 would have to be less than 3010 $GtCO_2$ (when accounting for non-CO_2 forcings as in the ambitious RCP2.6 emission scenario, [Collins et al., 2013]). But already 2075 $GtCO_2$ had been emitted between 1870 and 2016, and humanity is currently emitting about 36 $GtCO_2$ per year [Le Quéré et al., 2016]. So without emission reductions the remaining budget for the 2 °C target would be spent within two and a half decades, and even earlier for the more ambitious 1.5 °C target.

However, examples of GHG emission reductions are limited to the recent period in industrialised countries. On the global scale, emissions are currently stagnating and it

is unclear whether the peak of emissions has been reached or will be reached soon. So it is an open question whether humanity will manage to meet the ambitious targets in the near future. Therefore, other (perhaps desperate) ways of dealing with climate change have been proposed.

1.2 Climate engineering

As GHG emissions continue to rise, the idea of deliberately altering the climate through large scale technological measures (other than emission reductions) has gained increasing interest. The proposed methods for this so-called *climate engineering* (CE) or *geoengineering* can be divided into two groups: those that tackle the root of climate change, namely the excess atmospheric concentrations of GHGs, by removing them from the atmosphere are commonly summarized under the term *carbon dioxide removal* (CDR); those that seek to cool the Earth by reducing the amount of incoming radiation are called *solar radiation management* (SRM).

Besides studies in the field of natural science and engineering investigating the feasibility, effectiveness, and side effects of such techniques, there has also been considerable research on political, legal, economical, and ethical questions related to possible deployment of CE [e.g. Schäfer et al., 2015].

One might ask, why research resources should be spent on such a science-fiction idea, which most people tend to see rather critically [Braun et al., 2017]. And there exist serious arguments against research on climate engineering. For example it is argued, that once research is started it may lead to further and further progress, development, and ultimately to an almost inevitable urge to deploy SRM (known as the *slippery slope* argument). Or the existence of SRM research programmes might cause people to reduce their efforts at reducing emissions (the *moral hazard* argument) [e.g. Preston, 2013]. But we have to admit that there is considerable uncertainty in the expectable impacts of climate change. This is because on the one hand the level of future greenhouse gas emissions is uncertain, and on the other hand the exact response of the climate system to these emissions is uncertain as well. Therefore, we have to face the reality that there is a certain probability of a global warming well above 2 °C with possibly dramatic impacts. Or it might be much more difficult to adapt to climate change than currently expected. In such a situation, future generations might feel themselves forced to take short-term measures like CE. For providing them with a profound basis of knowledge allowing an informed decision on whether and how to deploy CE techniques, research has to be conducted now.

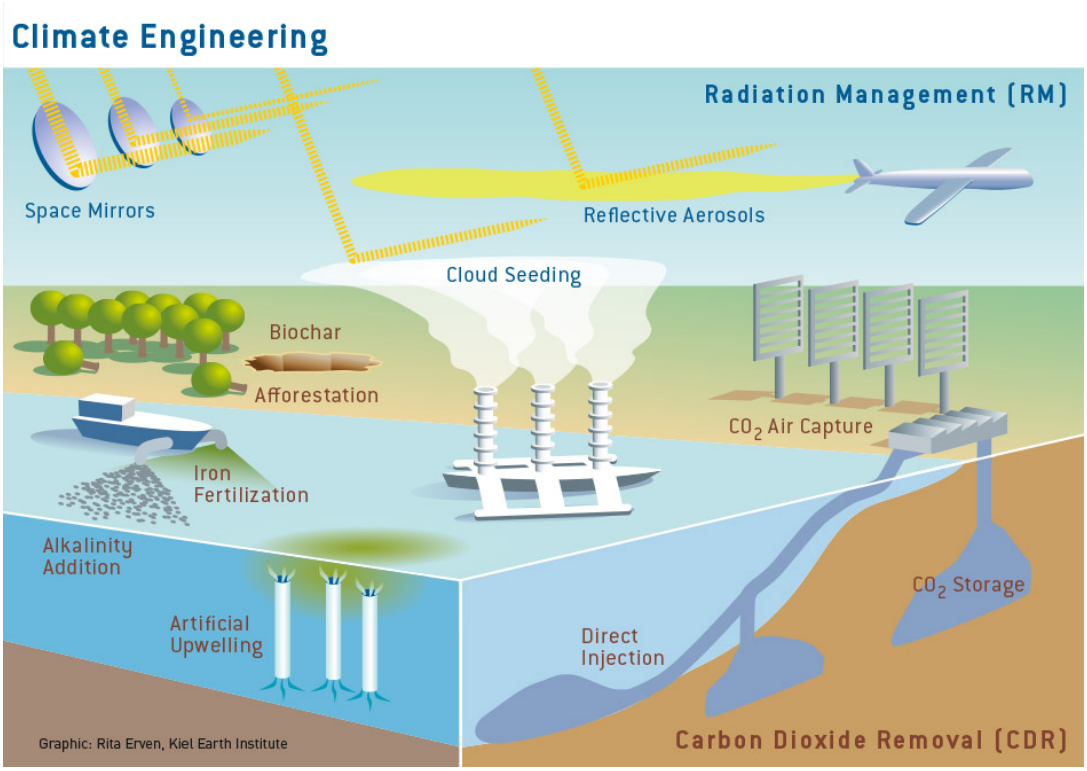

Figure 1.1: Overview of some of the proposed climate engineering techniques described in the text. Graphic taken from `www.spp-climate-engineering.de`.

1.2.1 Overview of proposed climate engineering techniques

Figure 1.1 illustrates a number of proposed SRM and CDR techniques. Numerous ways of removing GHGs from the atmosphere have been suggested. Some of them aim at converting strong short-lived GHGs into less problematic compounds (e.g. CH_4 into CO_2), but most CDR techniques seek to capture and store CO_2. The capturing could be done by technical devices directly at the source points or from ambient air, or through enhanced geochemical sinks (in the case of ocean alkalinity enhancement) or biological sinks of CO_2. Such biological sinks could operate through marine organisms, e.g. fertilised through addition of iron or artificial upwelling of nutrient-rich deep water, or terrestrial plants. The captured carbon could be stored on land (by afforestation), under ground (as charcoal or directly as CO_2 sequestered in geological storages), or in the deep ocean. All the proposed techniques have their risks and limitations (e.g. land use competition and conflicts, impact on ecosystems, limited storage capacities, residence time in the reservoir, etc.). CDR shall not be considered further in this thesis but it needs some attention as well.

This work focuses instead on SRM and especially on the technique that is studied and discussed most so far, because it has a strong natural analogue and could possibly pro-

vide a fast cooling of the Earth with relatively limited effort (i.e. with a high leverage): the injection of aerosols or aerosol precursors into the stratosphere, commonly called *stratospheric aerosol injection* (SAI). Before we present this technique in more detail in Section 1.2.2, we will have a short overview of further methods of SRM that have been proposed to increase the Earth's albedo.

The concept of *marine cloud brightening* (MCB) [Latham, 1990] is based on the fact that, for a given amount of water, clouds with smaller droplets reflect more sunlight. The size of cloud droplets could be reduced by injecting additional cloud condensation nuclei (CCN), e.g. in the form of sea salt particles, resulting in a higher cloud droplet number concentration (CDNC), i.e. in a higher cloud albedo.

Other proposed methods seek to increase the albedo either of the ocean surface, by creating small air bubbles in the surface layer [Seitz, 2011] or by covering the water with foam, or of the land surface by planting brighter plants or by painting buildings and roads. Even mirrors in space reflecting or diffracting a fraction of the sunlight away from the Earth have been suggested. Although this may be one of the technologically and economically most challenging methods, its possible impact has been studied widely with climate models, because it can be easily implemented by reducing the solar constant.

The last proposal that shall be mentioned here is the concept of *cirrus cloud thinning* (CCT) [Mitchell and Finnegan, 2009]. Strictly speaking, it is not an SRM method because it seeks to cool the Earth by increasing the amount of outgoing terrestrial infrared (LW) radiation. Cirrus clouds, which consist of ice particles and are located in the upper troposphere, can have a net heating effect if their absorption of LW radiation (greenhouse effect) dominates over the reflection of SW (solar) radiation. This is especially the case at high latitudes during winter. Therefore, reducing the cirrus cloud cover can have a cooling effect, which in principle could better compensate the warming effect of greenhouse gases because it also acts on the LW spectral range, in contrast to SRM techniques. The reduction of cirrus cloud cover could be achieved by increasing the size of the ice crystals and thereby increasing their fall speed. In regions where cirrus formation through homogeneous freezing (producing many small ice particles) dominates, the injection of ice nuclei may result in fewer, larger ice crystals with a shorter lifetime. But it is unclear in which fraction of the upper troposphere homogeneous freezing dominates and hence what the cooling potential of CCT would be. In addition, the concentration of ice nuclei would have to be chosen carefully, because they can also cause the formation of (potentially warming) additional cirrus clouds which would not have formed under unperturbed conditions [Lohmann and Gasparini, 2017].

It is important to note that all radiation management techniques can only (at least partly) compensate the warming effect of greenhouse gases. But they cannot solve other problems from high CO_2 concentrations like ocean acidification.

1.2.2 Stratospheric aerosol injection

This thesis focusses on climate engineering through stratospheric aerosol injection, which we will briefly present in this section. The potential of the stratospheric aerosol layer to reduce the Earth's surface temperature has been known for a long time. A cooling was observed after major volcanic eruptions like those of Mount Tambora (in 1815), Krakatau (in 1883), and Mount Pinatubo (in 1991), which injected large amounts of SO_2 into the stratosphere [e.g. Rampino and Self, 1982, Dutton and Christy, 1992]. The idea of stratospheric aerosol injection (SAI) is to achieve an artificial enhancement of the stratospheric aerosol layer. The deployment of SAI as a measure against global warming was first suggested by Budyko [1977], but a broader scientific debate on the subject was initiated several decades later by Crutzen [2006]. A deliberate injection of SO_2 forming sulphate aerosol would constitute a close analogue to volcanoes, but injection of other particle types is also proposed (see Chapter 2). Possible ways of delivery would be e.g. through high-altitude aircraft, tethered balloons or rockets [McClellan et al., 2012]. Although it requires more effort to bring material to the stratosphere than to emit it in the troposphere, it would be more efficient because aerosols have a longer residence time in the stratosphere. But this also means that if one wanted to stop the deployment of SAI (e.g. because of unforeseen problems), its effects would still persist on a timescale of months to years. Suddenly stopping SAI could also be problematic because the climate system would rapidly catch up on the warming compensated by SAI if GHG levels continued to rise. This is known as the *termination effect* and has been studied e.g. by Jones et al. [2013] who found a rapid temperature and precipitation increase and sea ice loss after a simulated sudden stop of SAI. Another important risk is that the additional aerosol in the stratosphere could damage the ozone layer that protects life on Earth from dangerous UV radiation [Tilmes et al., 2008]. Further aspects of SAI to consider are discussed in Chapter 2.

1.3 Atmospheric aerosols

Since the effect of SAI depends on the behaviour and effects of aerosols, we will briefly summarise the relevant aspects of atmospheric aerosols in this section, which is partly based on the textbook by Boucher [2015].

The Earth's atmosphere mainly consists of gaseous compounds, but it also contains smaller amounts of liquids and solids, which affect the Earth system considerably. In principle, a mixture of solids or liquids in the gas phase is called an *aerosol*, but it is common to use the term for the liquid or solid compound only and we will stick to this convention in the text of this thesis. Since water is an important constituent of the atmosphere, many particles consist of liquid or frozen water, e.g. rain, cloud droplets,

fog, snow, or hail. They are summarised under the term *hydrometeors* and shall not be further considered here when we write about aerosols.

1.3.1 Aerosol properties

The properties of aerosols are mainly determined by composition and particle size. The size can span many orders of magnitude, from a single nanometre to hundreds of micrometres. Depending on the atmospheric conditions, one can usually observe several relative maxima in the particle size distribution, the so-called size modes. They are not sharply separated from each other and their width and mean size can vary, but they are a useful classification. The *nucleation mode* (≈1–10 nm radius) mostly contains particles that have formed from gaseous precursors. The *Aitken mode* (≈10–50 nm radius) is made up from nucleation mode particles that have grown through condensation. In the *accumulation mode* (≈50–500 nm radius) the aerosol mass accumulates through coagulation and further condensation. Most particles that are released at the Earth's surface belong to the *coarse mode* (>0.5 µm radius) and *super-coarse mode*.

Aerosol particles can consist of a variety of different substances. The most important constituents (besides water) are crustal minerals, sea salt, sulphate, nitrate, black carbon (also known as soot) and organic compounds. Freshly formed aerosol mostly consists of only one of these components, but during their atmospheric lifetime particles are commonly mixed externally and internally. The aerosol composition determines its hygroscopicity, i.e. how easily water can condense on the particles. Depending on the ambient relative humidity, condensational particle growth can be an important process that also affects the aerosol's physical properties.

Aerosol particles interact with electromagnetic radiation and can thereby affect the Earth's radiative budget considerably. On the one hand aerosols absorb radiation and re-emit it according to their temperature. On the other hand they scatter radiation. How exactly this happens, strongly depends on the size parameter x, which is the ratio between the particle circumference $2\pi r$ (with the particle radius r) and the wavelength λ:

$$x = \frac{2\pi r}{\lambda} \tag{1.1}$$

The degree of interaction is measured by the absorption and the scattering cross section of a particle. The sum of both is called the extinction cross section. For particles much smaller than the wavelength (i.e. $x \ll 1$), scattering can be described by the Rayleigh theory, where the scattering cross section is proportional to x^4. For objects much larger than the wavelength, geometrical optics can be applied and the extinction cross section converges towards twice the geometric particle cross section $\sigma_g = \pi r^2$. The intermediate regime is described by the Mie theory in the case of spherical particles. Extinction usually reaches its maximum in this intermediate range of the size parameter, which in case of visible light corresponds to accumulation mode particle sizes. Mie

theory allows to compute aerosol optical properties based on the particle size and the complex refractive index, whose imaginary part characterises the absorption within the medium. Its numerical implementation is included in many numerical aerosol models. The assumption of spherical particles is valid for liquid atmospheric aerosols, but not for all solid aerosols (such as dust particles) and ice particles.

1.3.2 Tropospheric aerosols

The troposphere, i.e. the lowest layer of the atmosphere (reaching altitudes of 8-15 km), contains the largest part of the atmospheric aerosol burden and a large variety of aerosol species (already listed above). Some of them are already emitted as particles (*primary* aerosols), others form through condensation of gaseous precursors (*secondary* aerosols). There are numerous natural and anthropogenic sources of tropospheric aerosols and aerosol precursors: wind friction on the ocean surface (sea spray) or on the land surface (mineral dust), combustion of biomass or fossil fuels, emissions from plants and other living organisms, volcanic eruptions (ash and sulphate), as well as agricultural and industrial processes. Aerosols can have many different impacts in the troposphere: they absorb and scatter radiation, thereby changing temperature and the ratio between direct and diffuse light, affect cloud formation and properties by acting as cloud condensation or ice nuclei, play a role in atmospheric chemistry, serve as nutrients, but also act as air pollutants with adverse effects on human health. Due to efficient removal mechanisms (mostly wet deposition and boundary layer processes) tropospheric aerosols have a lifetime in the order of days or weeks. Since there is only little exchange between tropospheric and stratospheric aerosols, and the aerosol physics at play are considerably different between troposphere and stratosphere (see following section), tropospheric and stratospheric aerosols are usually considered separately. Therefore, we will now abandon tropospheric aerosols and focus on aerosols in the stratosphere.

1.3.3 Stratospheric aerosols

Aerosols are also present in the layer above the troposphere, namely the stratosphere. The stratospheric aerosol layer was discovered and first described by Junge et al. [1961] and is therefore also called the *Junge layer*. Only a minor fraction of the stratospheric aerosol is of tropospheric origin, because tropospheric air entering the stratosphere mainly in the tropics has to pass the very cold tropical tropopause, a pathway where the condensing humidity scavenges most of the aerosols. The small fraction that survives this transport includes organic aerosols and black carbon [Murphy et al., 2007]. Hence, stratospheric aerosols are mostly formed locally from gaseous compounds. There is also a source of meteoritic dust particles from above [Cziczo et al., 2001], but it is likely to be very small. Since there is no wet deposition in the extremely dry stratosphere and

stratosphere-troposphere air exchange is very limited, stratospheric aerosols have a much longer residence time in the order of months or years. Therefore, slower physical processes like particle growth and size-dependent sedimentation are more relevant than in the troposphere. Figure 1.2 illustrates the current state of knowledge about relevant processes, sources, and sinks of stratospheric aerosol, as described in the comprehensive review article by Kremser et al. [2016].

Sulphate particles are the main constituent of the stratospheric aerosol layer, but their concentration can vary strongly in time due to the sporadic nature of their main source, major volcanic eruptions. In the absence of such eruptions, which can inject large amounts of sulphur dioxide (SO_2) directly into the stratosphere, sulphur species from other tropospheric sources can enter the stratosphere, e.g. through deep convection in the tropical troposphere and subsequent slow upward transport in the tropical tropopause layer (TTL). Sulphur passes the tropopause mainly in the form of carbonyl sulphide (OCS) [Chin and Davis, 1995], but also (in smaller amounts) as SO_2, dimethyl sulphide (DMS, $(CH_3)_2S$), or hydrogen sulphide (H_2S), who all have a relatively low solubility in water that prevents them from being completely scavenged. OCS is believed to be the dominant source, because it is chemically much more stable in the troposphere than the other sulphur compounds. But the higher UV radiation fluxes in the stratosphere allow the photolysis of OCS and make it available for chemical conversion. Under non-volcanic conditions, the main sources for these sulphur compounds are marine organisms (DMS and CS_2, both at least partly converted to OCS), biomass burning (SO_2 and OCS), vegetation (DMS), and anthropogenic emissions (mostly SO_2). Ultimately, through photolytical and/or chemical conversion the sulphur-bearing compounds end up as sulphuric acid (H_2SO_4). As the formation of H_2SO_4 requires water molecules, it depends on the relative humidity. If enough water vapour is available, H_2SO_4 and H_2O rapidly form droplets of sulphuric acid solution due to their very low vapour pressure, but they can also condense on pre-existing particles.

As pressure decreases and temperature increases with increasing height in the stratosphere, the sulphate particles tend to evaporate above 25-30 km. Therefore, the Junge layer extends roughly from the tropopause to this altitude in the vertical direction. The horizontal distribution is very homogeneous in the zonal (i.e. longitudinal) direction due to strong zonal winds in the stratosphere. The meridional (i.e. latitudinal) Brewer-Dobson circulation (BDC, ascending in the tropics, moving towards the poles, and descending at high latitudes) spreads the aerosol layer over all latitudes.

Stratospheric aerosols can be observed either *in situ* or remotely. Important balloon-borne in situ measurements have been performed on a regular basis since the 1970s at the University of Wyoming [Deshler et al., 2003] using optical particle counters (OPC). This method uses aerosol forward scattering under a certain angle (25° or 40°) and Mie theory to determine the particle concentration in several (usually 12) size classes, providing vertically resolved information on the aerosol size distribution. LIDAR is a widely used remote sensing technique that measures the backscattering of laser

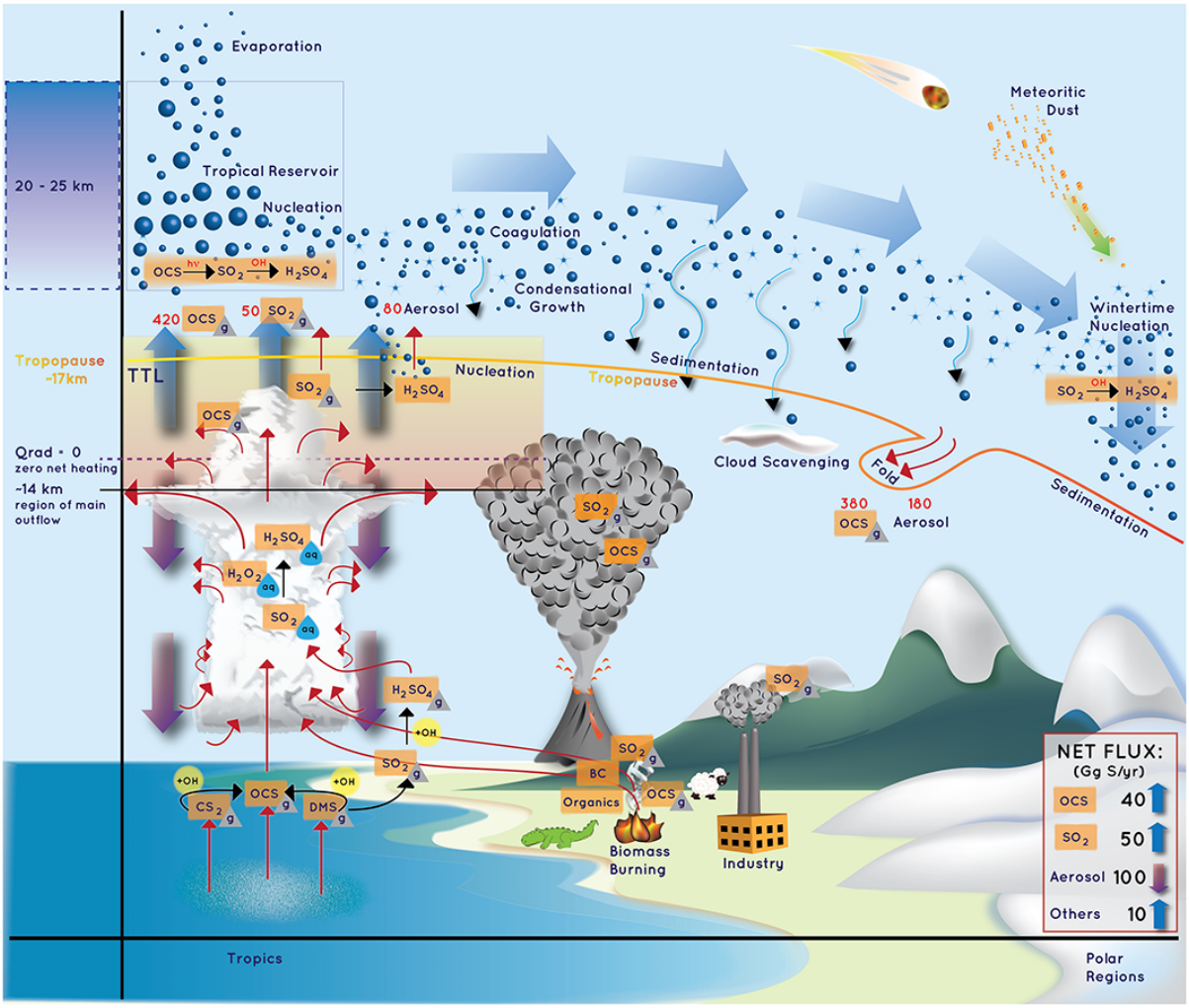

Figure 1.2: Schematic extracted from Kremser et al. [2016] with the following caption: "Schematic of the relevant processes that govern the stratospheric aerosol life cycle and distribution. The large blue arrows indicate the large-scale circulation, while the red arrows indicate transport processes. The black arrows indicate chemical conversions between compounds. The different chemical species are marked as either gas phase (grey triangle) or aqueous phase (blue drop). The blue thin arrows represent sedimentation of aerosol from the stratosphere to the troposphere. Note that due to its long tropospheric lifetime, carbonyl sulfide (OCS) does not necessarily require deep convection to be transported into the TTL (as shown in the figure). The red numbers represent the flux of OCS and sulfur dioxide (SO_2) as well as the flux of aerosol in Gg S/yr based on model simulations from Sheng et al. [2015]. The approximate net flux of sulfur containing compounds across the tropopause is shown in the grey box [Sheng et al., 2015], where the 10 Gg S/yr contribution from others can be mostly attributed to dimethyl sulfide (DMS) and hydrogen sulfide (H_2S). Other chemical compounds shown in this figure are carbon disulfide (CS_2), sulfuric acid (H_2SO_4), and black carbon (BC). [...]"

light by molecules and aerosols at a certain wavelength as a function of altitude. It can be ground based [e.g. Fiocco and Grams, 1964, Jäger, 2005], air-borne, or satellite-borne like the lidar instrument CALIOP on CALIPSO [e.g. Winker et al., 2006, Vernier et al., 2009]. Another technique to measure stratospheric aerosols from space is the solar occultation method. It determines the extinction of sunlight going through the upper layers of the atmosphere and reaching the satellite instrument that is pointing towards the sun (a so-called *limb geometry*). This technique was used for a long series of stratospheric aerosol measurements including the SAGE II instrument [e.g. McCormick, 1987, Thomason et al., 2008] that operated from 1984 to 2005. It has a nearly global coverage, but at a relatively low time resolution of roughly one month. Furthermore, the geometry only allows measurements for relatively low extinction, so that higher aerosol loadings after volcanic eruptions or in the troposphere cannot be observed. In this thesis we will use in situ OPC measurements and SAGE II satellite observations for the evaluation of the new LMDZ-S3A model, but further observations can be used for model evaluation in the future.

1.3.4 Numerical modelling of aerosols

Since we develop and use a numerical model for the study of stratospheric aerosol in this thesis, we will now shortly discuss the principles of aerosol modelling with a focus on global models of stratospheric sulphate aerosols. Existing models will be discussed in more details within the model description in Chapter 3.

Every model describing the evolution of aerosols has to include a representation of their sources, transport, transformation processes, and sinks. As stratospheric sulphate aerosols mainly form from gaseous precursors, they should also be represented together with the conversion processes leading to particle formation. The aerosol source would then be the nucleation of particles from the gas phase, but it could also include aerosol transport from the troposphere to the stratosphere or a small term for meteoritic dust particles. Transformation processes include the condensation and evaporation of sulphuric acid (and water) and the coagulation of colliding particles. The sinks of stratospheric aerosols are sedimentation, advection, and (to a small extent) diffusion of particles to the troposphere, where wet deposition (in and below clouds) and dry deposition rapidly remove sulphate particles from the air. The transport of the aerosol happens through large-scale advection with the air masses (and through convection and other mixing processes in the troposphere).

There are different approaches for representing aerosols in numerical models. The most simple one is to assume fixed aerosol properties and only track the aerosol mass in a so-called *bulk approach*, which is computationally cheap. But as this does not permit to study the evolution of aerosol properties, more sophisticated schemes have been developed (see Figure 1.3). In the *modal approach* one distributes the aerosol over several size modes (often split up into a soluble and an insoluble mode) whose shape is allowed

to adjust to a certain degree, as particle mass and number concentrations within the mode are treated separately. This makes it much more flexible and powerful than the bulk approach, but the modal approach is still based on a number of assumptions which are derived from observations. For conditions where such observations are hardly or not available (like large sulphur injections from volcanoes or SAI) it may be better to use the more flexible and accurate *sectional approach*. Here the particle size range is divided into a larger number of size bins (typically 20 to 40 in global models) and the particle mass (or number) in every single size bin is treated separately. This allows the aerosol size distribution to evolve relatively freely, as it does not prescribe the existence and shape of certain size modes. But the larger number of variables makes the sectional approach computationally more expensive and it is difficult to represent the mixing of aerosol species of different chemical composition.

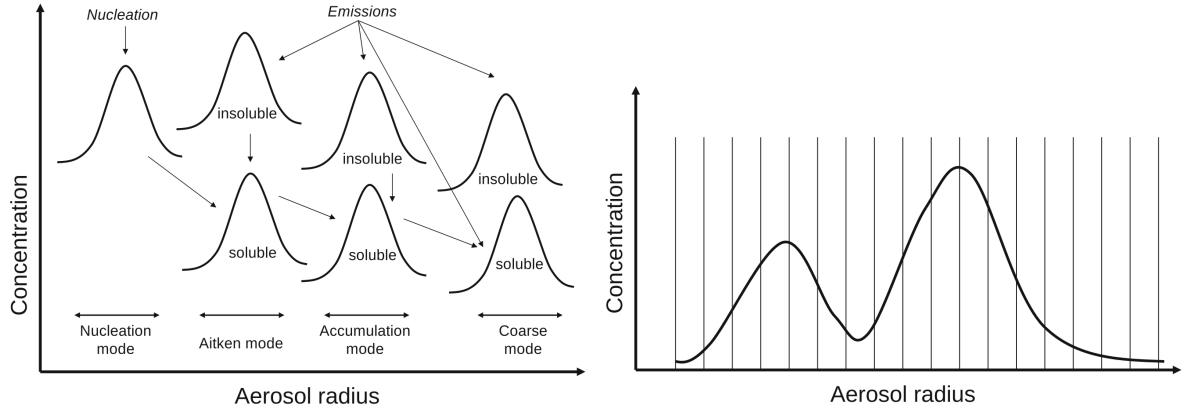

Figure 1.3: Schematic representation of the modal (left) and the sectional (right) aerosol modelling approach described in the text. Both graphics are extracted from Boucher [2015].

1.4 Outline of the thesis

This thesis focusses on studying Climate Engineering through stratospheric aerosol injections (SAI) with the global, three dimensional atmospheric general circulation model LMDZ including the new sectional stratospheric sulphate aerosol module S3A. In Chapter 2 we describe the current state of the science on SAI, including knowledge gaps and weaknesses of previous studies which motivated our own research in this field. In Chapter 3 we describe the aerosol model LMDZ-S3A, which has mainly been developed for being able to study SAI and whose development and testing was a major part of the doctorate. In Chapter 4 we validate the model under conditions of low and high stratospheric aerosol loading. In Chapter 5 we use this model to study the dependency of the radiative forcing (RF) of SAI on various parameters of the injection, the rapid adjustments of the atmosphere to the RF, and we regard some of the impacts

of SAI. In Chapter 6 we evaluate the potential of a combination of SAI and marine cloud brightening (MCB). Finally, in Chapter 7 we summarize and discuss our findings before we conclude with potential future research activities.

2 The physics of stratospheric aerosol injection

After a brief description of the basic idea behind stratospheric aerosol injection (SAI) in Section 1.2.2, we will now turn to the scientific discussion and literature on SAI. Because the Earth forms a unique system with many interconnections, studying the effects of SAI on the climate would require large-scale injection and would be practically identical to a deployment of geoengineering, including all the risks and societal difficulties. But possibly important processes on smaller scales (e.g. ozone chemistry, particle growth) could be studied through observations of natural perturbations to the stratospheric aerosol layer or through small-scale outdoor experiments with only local impact [Dykema et al., 2014].

In this context, global climate models are a good tool for evaluating the possible impacts of SAI on the global and regional scales, although it is hard to quantify the uncertainty of the model results, because there are no observations of SAI to compare with. Observations from periods following major volcanic eruptions can help to constrain the aerosol models, but there are only a limited number of measurements available. And it has to be noted that such eruptions are not a perfect analogue to SAI, because they can cover only a very limited set of conditions. In contrast, artificial injections offer many degrees of freedom in order to achieve a certain impact: the location, height, and size of the injection area, the time of the injection (e.g. continuous over the whole year or during shorter periods), the composition of the injected plume, and the amount of material injected. Furthermore, the continuous perturbation through SAI would allow the climate system to adjust even through slower processes (on annual to decadal time scales), while volcanic eruptions are mostly rather short perturbations. Modelling can thus investigate a wider set of scenarios that are not accessible through observations of natural analogues to SAI. In the following sections we will present a variety of different aspects of SAI to study.

2.1 The aerosol distribution and its properties

One of the key questions regarding SAI is, what aerosol size distribution results from the injection of particles or aerosol precursors like SO_2 or H_2SO_4. Particle size matters

so much, because it determines the optical properties and thereby the radiative forcing (RF), i.e. the cooling potential, of SAI. If particles grow too large, they scatter less solar radiation per unit mass and they have a shorter residence time in the stratosphere due to a higher sedimentation velocity. Particle size is expected to increase with increasing injection rate due to H_2SO_4 condensation on already existing particles and coagulation. Hence, there is a risk that scattering efficiency decreases with injection rate. Pierce et al. [2010] found that the optimal size of sulphate particles would be around 0.2 µm radius (see Figure 2.1). In their study, they simulated the direct injection of H_2SO_4 vapour instead of SO_2 and found that this would result in smaller particles with more favourable optical properties, but their results have not been confirmed by other studies yet. Furthermore, the optimal size of 0.2 µm is resulting from many aerosol processes and it is uncertain how to reach such an optimal size with SAI.

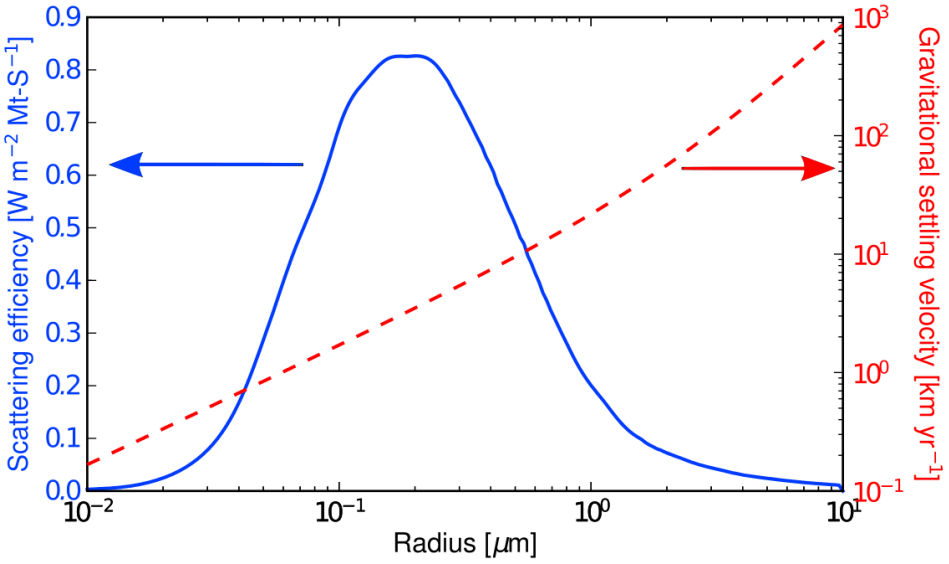

Figure 2.1: Figure extracted from Pierce et al. [2010] with the following caption: "Size dependence of factors that determine the radiative forcing of stratospheric sulphate aerosol. The blue curve and left axis show the solar-band cooling per mass (burden) of sulphate in the stratosphere as a function of aerosol size. The calculation was done assuming monodisperse aerosol and averaging over the solar spectrum. The red curve and right axis show the gravitational settling velocity at a height of 25 km."

Several studies investigated the aerosol size, its spatial distribution, and the resulting RF. Partly they also studied how sensitive the results were to certain parameters of the injection (e.g. amount, height, area, time). Heckendorn et al. [2009] found that continuous injections lead to larger particles than observed after volcanic eruptions, because the constant availability of sulphuric acid favours growth through coagulation and condensation. For the same reason Niemeier et al. [2011] found injections along the Equator to result in larger particles than injections from a single place at the Equator.

They also found that injections at higher altitude result in a considerably larger RF due to a longer residence time in the stratosphere. But higher injections would probably require a larger effort, because conventional aircraft can hardly fly higher than 15 km. Therefore, the development of a special aircraft fleet or an alternative technology aimed at higher injections, if required, would result in significantly higher economic costs [McClellan et al., 2012]. The costs as a function of injection height are nevertheless not well established, so it is not straightforward to decide if it is cheaper to inject a larger quantity at a lower altitude or a smaller quantity at a higher altitude. Likewise injection at several locations may be more expensive (because it would require more infrastructure and limit economies of scale) or less expensive (because it would be more effective to create radiative forcing). English et al. [2012] found that broadening the injection area (i.e. injecting over the whole tropics instead of only at the Equator), or injecting sulphate particles instead of SO_2 could both increase the RF of SAI.

2.2 Competing radiative effects

The competition between the (mostly negative) SW radiative forcing and the (mostly positive) LW radiative forcing due to infrared absorption (i.e. an additional greenhouse effect) of stratospheric aerosols is an important issue. As the net forcing is the sum of these partly compensating terms with considerable uncertainty, its uncertainty is even larger. Sulphate is known to absorb considerably in the infrared (see Figure 2.2), however, many studies have only considered the SW RF and may therefore overestimate the cooling capacity of SAI with sulphate aerosol. For the aerosol from the 1991 eruption of Mount Pinatubo, which had relatively small particles and therefore a high SW scattering efficiency, the LW response compensated about 50 % of the SW response [Soden et al., 2002] (also see Figure 4.1). An even larger compensation can be expected for probably larger SAI aerosol.

In order to overcome this issue, less absorbing aerosol materials such as solid TiO_2, Al_2O_3, $CaCO_3$ or diamond particles have been suggested [Weisenstein et al., 2015, Dykema et al., 2016, Keith et al., 2016]. But due to the lack of a natural analogue the research on alternatives to sulphate aerosol is problematic and in any case still in its infancy. Therefore, in this thesis we only consider SAI with sulphate aerosol.

2.3 Efficacy and scalability

For evaluating the potential of SAI to compensate the greenhouse gas warming, it is important to know how the net RF scales with the magnitude of the injection. Depending on the rate of greenhouse gas emission reductions, an SAI cooling capacity up to several $\mathrm{W\,m^{-2}}$ might be required to avoid dangerous global warming. Earlier

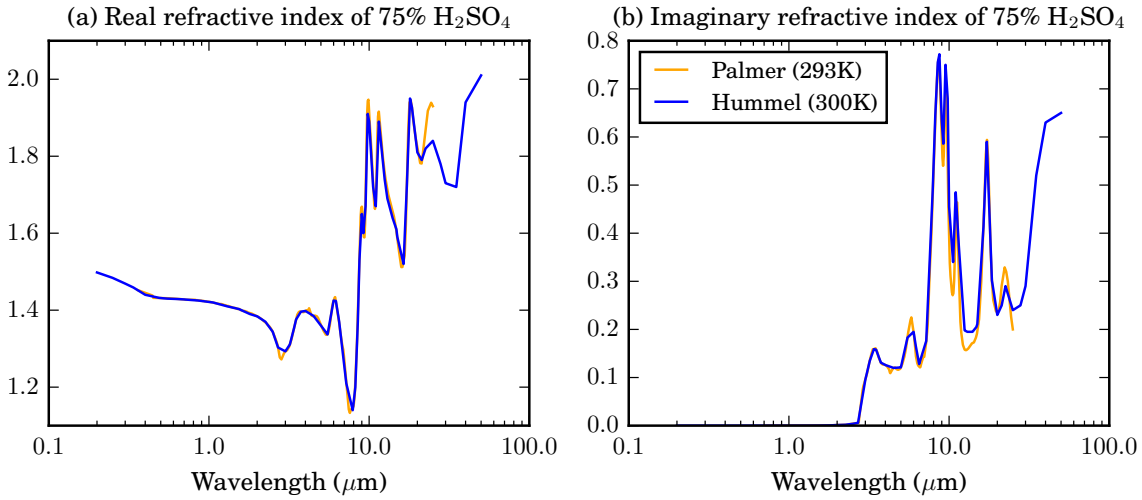

Figure 2.2: Real (a) and imaginary (b) refractive index of 75 % sulphuric acid solution in water. The values from Hummel et al. [1988] (blue lines) were used for the computation of aerosol optical properties in the LMDZ-S3A model. Values from Palmer and Williams [1975] (orange lines) were used in other models [e.g. English et al., 2012].

studies by Heckendorn et al. [2009] and Niemeier et al. [2011] already showed that the RF of SAI increases less than linearly with the amount of SO_2 injected. At large sulphuric acid concentrations, particles tend to grow larger through condensation and coagulation, resulting in a decreased mass scattering efficiency for SW radiation but constant mass absorption efficiency for LW radiation. This results in a less negative net forcing efficiency (i.e., radiative forcing per unit of injection rate) as the injection rate increases. Niemeier and Timmreck [2015] studied the relation between sulphur dioxide injection rate and global mean radiative forcing in a series of simulations and found that for a 10-fold increase in injection rate (from 5 to 50 $\mathrm{Tg(S)\,yr^{-1}}$), the net forcing efficiency is reduced by 50 %. If the efficiency reduction turns out to be larger than modelled, then it would question the effectiveness of SAI as an effective and scalable technique to compensate high greenhouse gas concentrations. Also the unintended side effects (e.g. on the ozone layer or air quality) may become more important for larger injections, if they scale linearly with the injected mass.

2.4 Short term impact on the atmosphere

Besides the intended planetary cooling, the injected aerosol would have further impacts on the atmosphere. Some of them would already occur on the short term (within days), i.e. before the cooling of the Earth's surface takes place (on the time scale of years). The

increase in aerosol surface area density can favour heterogeneous chemical reactions leading to the destruction of stratospheric ozone [Tilmes et al., 2008, 2009, Pitari et al., 2014]. Though, the expected increase in harmful UV radiation at the Earth's surface might be compensated by increased scattering of UV radiation by the stratospheric aerosol, which induces more absorption by ozone because of a longer photon path.

The heating of the lower stratosphere and upper troposphere (UTLS) through absorption of radiation by the aerosol [e.g. Ferraro et al., 2011] can have multiple effects. Aquila et al. [2014] and Niemeier and Schmidt [2017] found that the quasi-biennial oscillation (QBO) in the equatorial stratosphere would slow down for SAI injection rates below $5\,\mathrm{Tg(S)\,yr^{-1}}$ and even break down for larger injections. This change in the stratospheric dynamics may affect the tropospheric climate, but also the spatial distribution of the aerosol itself, because the speed of the meridional transport depends on the phase of the QBO. Another effect of a warmer UTLS would be an increase of the stratospheric water vapour concentration, since more water could pass the warmed tropical cold-point tropopause. The additional water would act as a greenhouse gas, thereby further reducing the cooling effect of SAI, and it could enhance ozone destruction.

Furthermore, the heating would affect cirrus clouds in the upper troposphere. Kuebbeler et al. [2012] found that the stabilisation of the UTLS due to the aerosol heating results in a thinning of cirrus clouds, which would contribute 60 % to the overall cooling effect of SAI. In contrast, the direct microphysical effect of sedimented sulphate particles on the properties of cirrus clouds (i.e. sulphate particles acting as ice nuclei) would probably be small [Cirisan et al., 2013].

2.5 Climate impact

Since the motivation for SAI would be to abate global warming, it is crucial to study its impact on climate and how well it would compensate the effects of greenhouse gases. This compensation cannot be expected to be perfect, because SAI and greenhouse gases mainly act on different spectral ranges, SW and LW radiation, respectively. The spatial distribution of the positive LW RF of greenhouse gases is similar to that of the Earth's surface temperature. But the energy transport in the ocean and in the atmosphere causes the surface temperature to be more homogeneous than the insolation, which determines the possible negative RF of SAI (see Figure 2.3). This means that greenhouse gas warming is especially effective at high latitudes, while SAI cools best in the tropics. The superposition of both can therefore lead to considerable changes in regional energy balance and circulation patterns.

Most studies evaluated the changes in global surface temperature and precipitation under certain SAI scenarios. In this context, the initiative of the Geoengineering Model Intercomparison Project (GeoMIP, Kravitz et al. [2011]) has to be mentioned. It defined

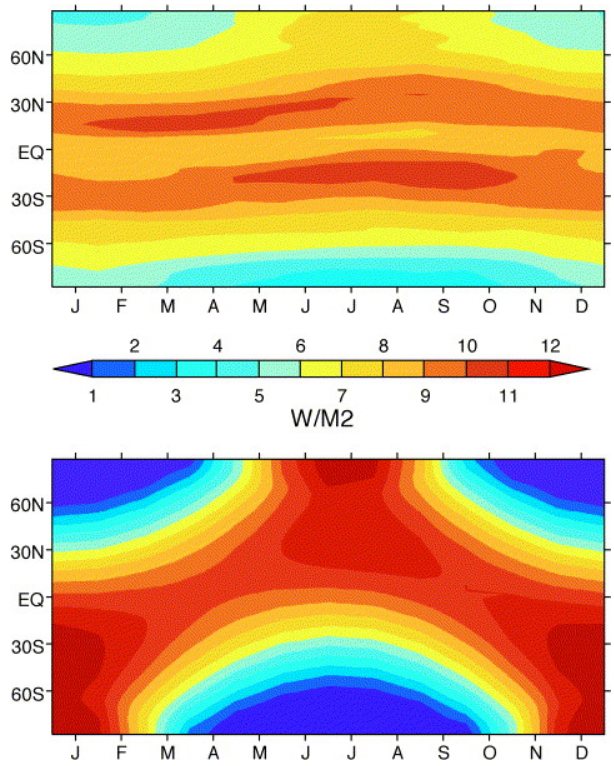

Figure 2.3: Figure extracted from Govindasamy et al. [2003] with the following caption: "Change in net long-wave radiative flux at the tropopause when CO_2 is quadrupled (top panel) with respect to the Control case and the reduction in incoming solar radiation (bottom panel) needed to compensate this forcing. Both values ($W\,m^{-2}$) are zonally averaged as a function of time of year. Change in solar radiation has a latitudinal and seasonal pattern markedly different from the radiative forcing of CO_2."

a set of different geoengineering scenarios, which have been simulated by a large number of different climate models, leading to more robust model results. One of these robust results is that it would probably be impossible to reset both, temperature and precipitation, to pre-industrial values with SAI. This is because SAI cools the Earth's surface and warms the stratosphere, thereby stabilising the troposphere and weakening the hydrological cycle (more than it is strengthened by the greenhouse gas warming). The global climate impact of SAI has been studied e.g. by Kravitz et al. [2013a] and Niemeier et al. [2013], while others like [Ricke et al., 2010] and Kravitz et al. [2014] focussed more on regional climate impacts.

At least as important as the changes in climate is the question how these changes affect ecosystems, agriculture, the global carbon cycle, and various other systems. In order to answer such questions, further modelling studies are necessary. Precipitation changes are important to look at. However, plant productivity does not necessarily decrease with decreasing precipitation, as it also depends on evaporation, incoming direct and diffuse radiation fluxes, CO_2 concentrations, and many other factors. However, these

relevant issues are out of the scope of this thesis.

2.6 Aerosol reaching the Earth's surface

Since sulphate aerosol is one of the major air pollutants in the troposphere, its fate once it left the stratosphere and the impact it may have at the Earth's surface need to be studied. Sulphate aerosol is removed from the troposphere within days, mostly through wet scavenging in and below clouds, thereby increasing the acidity of the precipitation. The deposition of acids can harm vulnerable ecosystems. In a previous study, Kravitz et al. [2009] found that the additional deposition (mainly over mid-latitude oceans) would be well below critical loadings for most ecosystems. Overall, it would be negligible in comparison to the amount coming from current anthropogenic sulphur emissions in the troposphere. This result nevertheless awaits confirmation from other models.

Another possible negative impact of SAI aerosol at the Earth's surface could be that the aerosol coming from the stratosphere might increase particle concentrations in ambient air before its deposition to the ground. Under present conditions, particulate matter with a diameter below 2.5 μm ($PM_{2.5}$) in outdoor ambient air might be responsible for about 3 million premature deaths per year worldwide [Lelieveld et al., 2015]. Most of the anthropogenic aerosol sources in the troposphere are rather close to populated areas, which causes their high impact on human health, whereas additional particles from SAI would probably be distributed over less populated areas where they would have a smaller impact. However, tropospheric pollution is expected to decrease in the future because of more stringent air quality policy and public awareness. Therefore increased pollution "from above" could be a sensitive issue that needs to be further examined.

2.7 Tailored climate engineering techniques

Given the characteristic effects and side effects of different SRM techniques and deployment strategies, one can evaluate the potential of combining several of them in portfolio approaches. It might be possible to design them in such a way that residual climatic changes on the regional scale and unintended side effects are minimised. Cao et al. [2017] recently simulated such a "cocktail" of SAI and cirrus cloud thinning (CCT) and found that this could allow restoring both, pre-industrial temperature and precipitation on the global scale, which is not possible with SAI alone. Kravitz et al. [2016] and other recent studies have put more emphasis on this design perspective on SRM. They argue for defining certain objectives and acceptable outcomes of geoengineering in the beginning and then finding the best solution to this design problem, while most other

studies just choose a rather simple SRM scenario initially and then evaluate its impact. The design issue is an important aspect of SAI to consider.

2.8 Weaknesses of previous studies

Recent reviews of the studies regarding SAI [Irvine et al., 2016, MacMartin et al., 2016, Visioni et al., 2017] highlighted the need for a more accurate representation of stratospheric aerosols in climate models. The accuracy of these models is of great importance, because the aerosol size distribution and also its spatial distribution are crucial for the impact of SAI, both the intended cooling and the unintended side effects. But most of the models used for previous studies had at least one or even several of the following weaknesses:

- They use a rather constrained and possibly less accurate modal aerosol scheme (see Sect. 1.3.4) [e.g. Ferraro et al., 2011, Aquila et al., 2014, Niemeier and Timmreck, 2015], which might not produce realistic aerosol size distributions under the exceptional conditions of SAI. Some models are even based on simplistic bulk aerosol schemes with prescribed aerosol properties. Only few models use the probably most accurate, though computationally more expensive, sectional modelling approach, which allows a free evolution of the aerosol properties. Among these, some reduce the computational cost by assuming complete zonal symmetry and using a two-dimensional aerosol model [e.g. Heckendorn et al., 2009, Weisenstein et al., 2015].
- They have a coarse spatial resolution on the vertical [e.g. Niemeier and Timmreck, 2015]. They are therefore not able to simulate realistic stratospheric dynamics and have to prescribe features like the quasi-biennial oscillation (QBO).
- The feedback of the aerosol's radiative effects (e.g. stratospheric heating) on the atmospheric dynamics is missing [e.g. Tilmes et al., 2009, English et al., 2012]. This may result in unrealistic spatial aerosol distributions and the underestimation of climate impacts.
- They focus on the negative SW forcing of the aerosol and do not consider to which extent it is compensated by the positive LW forcing, i.e. the additional greenhouse effect of the aerosol [e.g. Heckendorn et al., 2009, Pierce et al., 2010].

2.9 Research questions addressed in this thesis

Given the deficiencies of previous studies presented above, we decided to develop a new aerosol module within the atmospheric general circulation model LMDZ as

a more appropriate tool for studies of SAI. The model called LMDZ-S3A (Sectional Stratospheric Sulphate Aerosol) tries to overcome the weaknesses of other models mentioned above by using a sectional aerosol scheme, with particles active in the SW and LW spectral range, full interaction of the aerosol with radiation allowing feedback on the dynamics, and a high vertical resolution. The details of the model are described in Chapter 3, which is based on the publication by Kleinschmitt et al. [2017a]. We use this tool to provide some answers to the following questions:

- How does the RF of SAI scale with the amount of SO_2 injected?
- How sensitive is the RF to the injection height and strategy?
- What is the impact of the resulting stratospheric heating on the dynamics, especially the QBO?
- What impact of the aerosol at the Earth's surface can be expected?
- What are the rapid atmospheric adjustments to the aerosol, i.e. how do temperature, clouds, and stratospheric water vapour concentration change? And how do these changes contribute to the effective radiative forcing (ERF) of SAI?
- What would be the potential of combining SAI and marine cloud brightening (MCB) and how would their RF add up?

After the description and evaluation of the model in the following chapters, we will present and discuss the results of various SRM model experiments with respect to the questions presented above.

3 Description of the LMDZ-S3A atmosphere-aerosol model

In this chapter we offer a full and detailed description of the stratospheric sulphate aerosol module S3A and an overview of the relevant aspects of its host atmospheric model LMDZ, based on the publication by Kleinschmitt et al. [2017a]. But before doing so, we will briefly summarise how stratospheric aerosols in global climate models have been modelled so far.

3.1 Overview of previous modelling efforts

The study of stratospheric aerosols has traditionally been a separate activity to that of tropospheric aerosols, *inter alia* because of different observing methods and observing systems. This has also been true for the modelling efforts because, due to different residence times of aerosols in the troposphere and stratosphere, the relevance and relative importance of the various processes at play are different. Resolving accurately the size distribution of aerosol particles is crucial to calculate correctly the lifetime, vertical distribution and radiative properties of aerosol particles in the stratosphere, whereas tropospheric aerosol models can in first approximation rely on the assumption of self-preserving modes in the aerosol size distribution. Gravitational sedimentation, which is the main loss process for aerosols in the stratosphere [Deshler, 2008], is extremely dependent on the size of the aerosol particles. Coagulation, a fairly non-linear process, is also dependent on the details of the aerosol size distribution. The importance of resolving accurately the size distribution, notably the large particles tail of the distribution where most the sedimentation mass flux takes place, was already identified in the early modelling studies [Turco et al., 1979, Pinto et al., 1989], which used sectional aerosol models with a relatively high resolution in aerosol size but only one dimension (i.e. height) in space.

An accurate representation of dynamical processes in the stratosphere (e.g., subtropical meridional transport barriers, Brewer-Dobson circulation, stratosphere-troposphere exchange) is also paramount to properly simulate the distribution of stratospheric aerosols and their dispersion following volcanic eruptions. Representing accurately the interplay between aerosol microphysical and dynamical processes can be presumed to

be computationally very expensive as it involves at least five dimensions: three space dimensions, the aerosol size dimension, and the time dimension. This means that, for a given computational cost, some trade off is necessary between the representation (or discretisation) of these dimensions and/or the length of the simulation and the number of simulations. One possibility is to exploit the approximately zonal symmetry in the stratosphere to reduce the atmosphere to the height and latitude dimensions. This approach was used in particular by Bekki and Pyle [1992] and Mills et al. [1999] who retained the sectional approach to represent aerosol size.

The increase in computational capability has progressively allowed the development of three-dimensional models of stratospheric aerosols in the late 1990s / early 2000s. Most of these models were initially chemistry-transport models (CTMs). This so-called offline approach was often preferred because chemistry-transport models are cheaper to run, as wind and temperature fields are specified according to meteorological analyses instead of being calculated prognostically like in climate-chemistry models. In addition, since the transport of tracers is driven by meteorological analyses, the observed day-to-day variability in chemical composition can be reproduced (at least to some extent), facilitating the comparisons with measurements. While chemistry-transport models are suitable for a broad range of studies, they do not include any radiative feedback between chemical composition and dynamics, and notably ignore the radiative effects of aerosols onto atmospheric dynamics.

Given the importance of stratospheric aerosols for the Earth's radiative budget, there is also a need to represent stratospheric aerosols in climate models. The volcanic aerosol forcing is important to simulate the temporal evolution of the climate system over the last millennium in general, and over the instrumental period (1850 to present-day) in particular. This was initially done by prescribing the amount and properties of stratospheric aerosols as (time-varying) climatologies derived from observations. This was the case in most if not all of the climate models involved in the 5th phase of the Climate Model Intercomparison Project (CMIP5) as discussed in Flato et al. [2013], and it is still expected to be the case in the forthcoming sixth phase (CMIP6) [Eyring et al., 2016]. However capabilities to simulate stratospheric aerosols within global climate models are continuously improving.

The SPARC stratospheric aerosol assessment report [Thomason and Peter, 2006] provides a review of stratospheric aerosol models as of 10 years ago. It clearly represents a milestone and stimulated significant further model development since then. As a result, the recent review by Kremser et al. [2016] lists more than a dozen global three-dimensional stratospheric aerosol models. It should be noted however that several of these configurations share the same atmospheric general circulation model (GCM) or the same aerosol module and not all of them include the interaction of aerosols with radiation.

The sectional approach has been adopted by a number of these three-dimensional stratospheric aerosols [e.g., Timmreck, 2001, Pitari et al., 2002, Sheng et al., 2015].

Stratospheric aerosols have also been modelled in climate models as an extension of schemes initially designed for tropospheric aerosols. Simple mass-based (i.e., bulk) aerosol schemes modified to account for gravitational settling of the sulphate aerosols have been used occasionally [Oman et al., 2006, Haywood et al., 2010, Aquila et al., 2012]. Such models do not represent the growth of aerosol particles but rely instead on a fixed size distribution for each aerosol type. More sophisticated approaches have also been developed, whereby the aerosol size distribution is approximated by a statistical function with a pre-defined shape and a few variable parameters. The evolution of the size distribution is governed through variations in these selected parameters but, by construction, it has only a few degrees of freedom, which may lead to discrepancies and artefacts in the simulated size distribution. Examples include two-moment modal aerosol microphysics schemes such as the M7 model [Vignati et al., 2004, Stier et al., 2005] and the GLOMAP model [Mann et al., 2010, Dhomse et al., 2014], whereby each aerosol mode is represented prognostically by a number and a mass concentration.

A key question relates to the performance of the different approaches for representing the aerosol size distribution. Weisenstein et al. [2007] compared sectional and modal aerosol schemes. They found that the modal aerosol schemes performed adequately against the sectional aerosol schemes for aerosol extinction and surface area density but less so for effective radius. Kokkola et al. [2009] found considerable deviations in the simulated aerosol properties between sectional and modal aerosol schemes for elevated SO_2 concentrations but they focused on very short timescales after a SO_2 burst, and it could be that the discrepancy is less on longer timescales. The modal schemes have the advantage of being computationally cheap (relative to the sectional schemes), but may have to be "tuned" against results of the sectional scheme. The sectional approach has the advantage that the number of size bins can be increased to increase the accuracy of the aerosol scheme. If the scheme is numerically stable, it should converge to a (numerical) solution when the number of size bins increases. It is thus possible to evaluate the uncertainty induced by limiting the number of size bins, whereas it is difficult, if not impossible, in the modal approach to assess the uncertainty induced by the assumption of pre-defined aerosol modes with pre-defined shape. This does not mean however that aerosol sectional scheme will always be superior, as in the end, it will be subject to the same computational trade off as other models, and the relatively large cost of the sectional approach may limit the horizontal or vertical resolutions of the atmospheric model.

A climate model with a well established stratospheric aerosol capability is the WACCM/CARMA model described by English et al. [2011] (for WACCM see Garcia et al. [2007] and for CARMA see Toon et al. [1988]) which includes a sectional stratospheric aerosol with all the relevant chemistry and microphysics, along with a high vertical resolution. However the model does not consider aerosol radiative heating. Recently Mills et al. [2016] used the WACCM model to simulate the time evolution of the stratospheric aerosol over the period 1990–2014. They find a good agreement in stratospheric aerosol optical depth (SAOD) with SAOD derived from several available lidar measurements

by Ridley et al. [2014] and in surface area density (SAD) with balloon-borne optical particle counter (OPC) measurements at the University of Wyoming [Kovilakam and Deshler, 2015].

3.2 The host atmospheric model LMDZ

The newly developed sectional stratospheric sulphate aerosol (S3A) module is now part of the three-dimensional atmospheric general circulation model (GCM) LMDZ described in Hourdin et al. [2006] and Hourdin et al. [2013]. LMDZ itself can be coupled to the ORCHIDEE land surface model [Krinner et al., 2005], the oceanic GCM NEMO [Madec, 2008] and other biogeochemical or chemical model components to form the IPSL Earth System Model [Dufresne et al., 2013]. It is thus possible to use the S3A module to study the climate response to volcanic eruptions or SAI. We briefly describe below the relevant aspects of the host atmospheric model in this section and make a comprehensive description of the S3A module in Section 3.3.

3.2.1 Model physics and resolution

LMDZ is an atmospheric general circulation model (GCM) developed at the Laboratoire de Météorologie Dynamique (LMD) in France. It is separated into two parts. The first one is a three-dimensional dynamical core using the *primitive equations* to describe atmospheric flows. The equations include the conservation of important quantities like air mass, momentum, and water. For solving them, the hydrostatic approximation and the thin layer approximation (i.e. that the horizontal scale is much larger than the vertical) are used. The numerical integration requires a discretisation in space, for which LMDZ uses the finite difference method and a so-called Arakawa-C latitude-longitude grid. LMDZ offers a special *zoom* option to increase the horizontal grid resolution regionally (therefore the Z in LMDZ). The second part of the model, called the *physics*, includes all the physical parametrisations of processes that are not resolved by the dynamical core, e.g. clouds, convection, boundary layer processes, and radiative transfer. In LMDZ they are treated in each vertical model column separately. The time resolution of the physics in LMDZ is generally lower than that of the dynamics, in which the finite difference method requires a small timestep to converge.

A full description of the LMDZ model in its LMDZ5A configuration is available in Hourdin et al. [2006] and Hourdin et al. [2013]. We do not repeat the description here but instead focus on the evolutions of the model since Hourdin et al. [2013] and the specificities of the LMDZ configuration considered in this thesis.

In the configuration tested here with the S3A module, LMDZ is run with 96×96 grid-points, i.e. a horizontal resolution of 1.89° in latitude and 3.75° in longitude –which is

the same as for LMDZ5A–, but with a vertical resolution increased to 79 layers and a model top height of 75 km. The additional layers are mostly located in the stratosphere so that in the lower stratosphere (between 100 and 10 hPa) the vertical spacing Δz is approximately 1 km in this model setup. The increased resolution on the vertical aims to "close" the stratospheric circulation. It is also necessary to generate a realistic quasi-biennial oscillation (QBO) as discussed below. de la Cámara et al. [2016] provide a more extensive description of the stratospheric dynamics modelled with this vertically enhanced configuration of LMDZ.

Our configuration of the LMDZ model differs from that described in Hourdin et al. [2013] in that it has a different radiative transfer code. In the shortwave (SW), the code is an extension to 6 spectral bands of the initial 2-band code that is used in LMDZ5A [Fouquart and Bonnel, 1980], as implemented in a previous version of the ECMWF numerical weather prediction model. In the longwave (LW), we use the ECMWF implementation of the RRTM radiative transfer scheme [Mlawer et al., 1997] with 16 spectral bands. This change in radiative transfer scheme is motivated by the necessity to account for the radiative effects of the stratospheric aerosols both in the SW and LW part of the spectrum with sufficient spectral resolution.

Finally it should be noted that the time step for the model physics, Δt_{phys}, is unchanged at 30 minutes, which is also the main timestep used for the S3A module.

3.2.2 Tropopause recognition

As the model focuses on stratospheric aerosols, the separation between troposphere and stratosphere (i.e. the location of the tropopause) is of special importance. The S3A module requires the knowledge of whether a particular model grid box is located in the troposphere or the stratosphere, because the processes of nucleation, condensation, evaporation and coagulation are only activated in the stratosphere. Tropospheric aerosols are treated separately by a standard bulk aerosol model [e.g., Escribano et al., 2016]. Also we have a set of stratospheric aerosol variables that are only diagnosed in the stratosphere.

To this effect we use the algorithm by Reichler et al. [2003] which is based on the WMO definition of the tropopause as "the lowest level at which the lapse-rate decreases to 2 K km^{-1} or less, provided that the average lapse-rate between this level and all higher levels within 2 km does not exceed 2 K km^{-1}". We use the FORTRAN code provided by Reichler et al. [2003] which we have adapted to the LMDZ model. With this the tropopause pressure is computed at each timestep. In the rare case that the algorithm does not find the tropopause in a grid column, it is set to a default value that only depends on the latitude φ (in radians) through the relationship:

$$p_{\text{TP}}\ [\text{hPa}] = 500 - 200 \cdot \cos(\varphi) \tag{3.1}$$

In this case the tropopause is assumed to vary between 300 hPa at the Equator to 500 hPa at the Poles, independently of the season. This assumption is rather conservative, as the modelled and observed tropopause is generally higher.

3.2.3 Quasi-biennial oscillation in the stratosphere

The vertical extension to the LMDZ domain, as discussed above, is accompanied by a new stochastic parametrisation of gravity waves produced by convection which is documented in Lott and Guez [2013]. This is another difference to the original LMDZ5A model configuration described in Hourdin et al. [2013] which did not include this parametrisation. The combination of the extended vertical resolution in the lower stratosphere and the gravity wave parametrisation generates a QBO in the model, as shown in Figure 3.1 and documented in Lott and Guez [2013]. The amplitude of the QBO around 10 hPa is around 10–15 $\mathrm{m\,s^{-1}}$ and is smaller than observed (20–25 $\mathrm{m\,s^{-1}}$). The easterly phases are also stronger and longer in duration than the westerly phases, which is realistic. One subtle difference with the QBO shown in Lott and Guez [2013] is that here the connection with the semi-annual oscillation (SAO) above is quite pronounced, whereas it was not so evident in Lott and Guez [2013]. This is because the characteristic phase speed we have recently adopted for the convective gravity waves $C_{\mathrm{max}} = 30\,\mathrm{m\,s^{-1}}$ [de la Cámara et al., 2016] is smaller than for the convective gravity waves parameter we used in Lott and Guez [2013]. The stronger connection can be further explained by the fact that more waves travelling through the QBO sector will likely be absorbed by the critical levels produced by the SAO. Finally, it is worthwhile to recall that our QBO does not extend down to 100 hPa, in contradiction with observations. In our model, it is probably due to the fact that we underestimate the explicit slow Kelvin waves that play a crucial role in the lower stratosphere (Giorgetta et al. [2006], for the Kelvin waves in models, see Lott et al. [2014]).

It is noticeable that the period of our simulated QBO in Figure 3.1 shortens and its amplitude increases during the second half of the simulation, i.e. as the aerosol layer builds up in the lower stratosphere. More precisely, the QBO has a period well above 26 months during the first five years before evolving to an almost purely biennial oscillation by the end of the simulation. This could be due to the warming of the stratosphere induced by the developing stratospheric aerosol layer (up to 1.5 K in the tropical lower stratosphere), which would be consistent with the opposite behaviour found when the stratosphere cools, e.g. in response to an increase in greenhouse gases (for the intensity and period see de la Cámara et al. [2016], for intensity only, see the observations in Kawatani and Hamilton [2013]). As our simulation is quite short, this result should be consolidated by longer runs. It should also be kept in mind that since the QBO in our model is probably oversensitive to changes in greenhouse gases, it may also be oversensitive to the aerosol content.

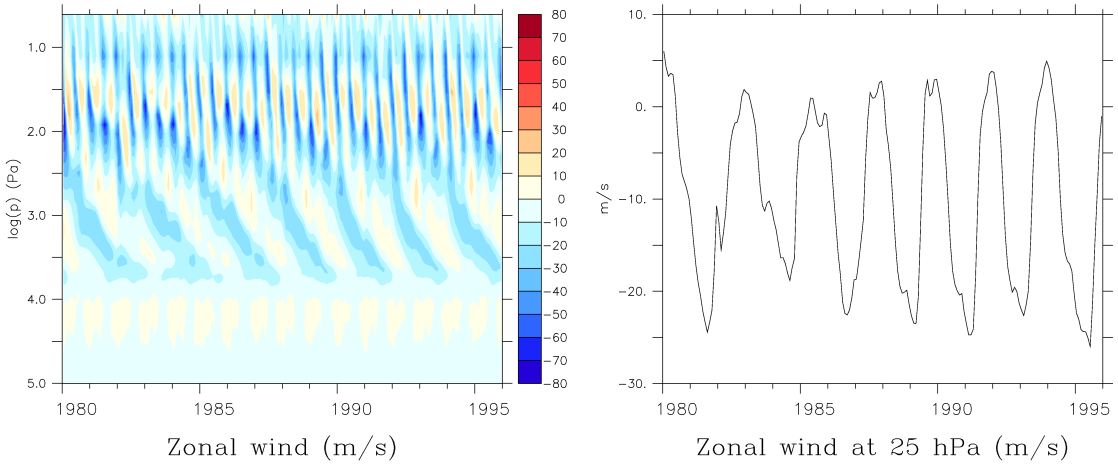

Figure 3.1: Left panel: Altitude-time profile of the zonal wind (in $\mathrm{m\,s^{-1}}$), averaged between 10° S and 10° N, from an LMDZ-S3A simulation with evolving background aerosol. The vertical axis shows the logarithm of the pressure in Pa. Right panel: Zonal wind at 25 hPa, averaged between 10° S and 10° N.

Despite these shortcomings, the self-generated QBO is an attractive feature of the LMDZ model to study stratospheric aerosols and different SAI scenarios. A more realistic simulation of the QBO would require a higher horizontal resolution.

3.2.4 Nudging to meteorological reanalysis

As an option, the LMDZ model can be nudged to a meteorological reanalysis. This is useful to simulate a historical situation with particular meteorological conditions. Only the horizontal wind components u and v are nudged. Nudging is performed by adding an additional term to the governing differential equations for u and v which relaxes the wind towards a meteorological reanalysis:

$$\frac{\partial u}{\partial t} = \frac{\partial u}{\partial t}_{\mathrm{GCM}} + \frac{u_{\mathrm{reanalysis}} - u}{\tau} \quad ; \quad \frac{\partial v}{\partial t} = \frac{\partial v}{\partial t}_{\mathrm{GCM}} + \frac{v_{\mathrm{reanalysis}} - v}{\tau} \tag{3.2}$$

where the relaxation time τ is taken to 30 minutes. Nudging is activated in the model calculations described in Sect. 4.3 using the ERA-Interim reanalysis reprojected onto the LMDZ grid. In this case, the reanalysed QBO prevails over the model self-generating QBO described in the previous section.

3.3 The sectional stratospheric sulphate aerosol module S3A

3.3.1 Prognostic variables

The S3A module in the configuration introduced here represents the stratospheric aerosol size distribution with $N_B = 36$ size bins of sulphate particles with dry radius ranging from 1 nm to 3.3 µm (i.e., $r_1 = 1\,\text{nm}$ and $r_N = 3.3\,\mu\text{m}$ for particles at 293 K consisting of 100 % H_2SO_4) and particle volume doubling between successive bins (i.e., $R_V = V_{k+1}/V_k = r_{k+1}^3/r_k^3 = 2$ for $1 \leq k < N_B$). The number of size bins N_B and the corresponding value of R_V represent a compromise between the accuracy of the scheme, which increases with higher resolution in size, and the computational cost of the model.

It should be noted that the r_k are the radius of the "middle" of the size bins. The radii of the lower and upper boundaries of bin k are

$$r_k^{\text{lower}} = \begin{cases} r_k / \sqrt{R_V^{1/3}} & \text{for } k = 1 \\ \sqrt{r_{k-1}\, r_k} & \text{for } 1 < k \leq N_B \end{cases} \quad ; \quad r_k^{\text{upper}} = \begin{cases} \sqrt{r_k\, r_{k+1}} & \text{for } 1 \leq k < N_B \\ r_k \cdot \sqrt{R_V^{1/3}} & \text{for } k = N_B \end{cases} . \tag{3.3}$$

Other global stratospheric models with sectional aerosol schemes have resolutions ranging from 11 to 45 size bins [Thomason and Peter, 2006]. Our model resolution of 36 size bins is therefore on the high end of this range. A relatively high size resolution is required for an accurate modelling of stratospheric aerosols because coagulation, an important process in the stratosphere, and gravitational sedimentation, the main loss process in the stratosphere, are very strongly dependent on the aerosol size.

The lower end of our size range (1 nm) was chosen to be close to the size of typical freshly-nucleated particles. We have tried to limit the number of bins by increasing the minimum aerosol size to 10 nm or more and feeding the nucleation term directly into this bin. However this resulted in inaccuracies in the size distribution both at small and large aerosol sizes, so this simplification was eventually not adopted. Large particles have short residence times and therefore very low concentrations in the stratosphere. As a result they do not contribute much to the aerosol optical depth, hence it is acceptable to set an upper range to 3.3 µm for our modelled size distribution. While 36 size bins correspond to our current configuration, the size range and size resolution can easily be changed in our model by adjusting the number of size bins (N_B), the minimum dry aerosol size (r_1), and the volume ratio between bins (R_V). All the parametrisations described below then adjust to the new size discretisation.

Aerosol amount in each of the size bins is treated as a separate tracer for atmospheric transport in the unit of particle number per unit mass of air as required by our mass-flux scheme [Hourdin and Armengaud, 1999].

3.3.2 Semi-prognostic sulphur chemistry

Besides the concentrations of aerosol particles in each bin, the module also represents the sulphate aerosol precursor gases OCS and SO_2 as semi-prognostic variables and gaseous H_2SO_4 as a fully-prognostic variable. The mass mixing ratios of OCS and SO_2 are initialised to climatological values at the beginning of a simulation. They are also prescribed throughout the simulation to climatological values below 500 hPa, but they evolve freely above that pressure level where they are subject to advection, convective transport, wet deposition, and chemical transformations. The chemical reactions transforming one species to another (OCS into SO_2 and SO_2 into H_2SO_4) during one model timestep are parametrised as exponential decay terms with prescribed chemical lifetimes:

$$\Delta[\mathrm{SO_2}] = \frac{M(\mathrm{SO_2})}{M(\mathrm{OCS})} \cdot [\mathrm{OCS}] \cdot \left[1 - \exp\left(-\frac{\Delta t_{\mathrm{phys}}}{\tau_{\mathrm{OCS}}}\right)\right] \tag{3.4}$$

$$\Delta[\mathrm{H_2SO_4}] = \frac{M(\mathrm{H_2SO_4})}{M(\mathrm{SO_2})} \cdot [\mathrm{SO_2}] \cdot \left[1 - \exp\left(-\frac{\Delta t_{\mathrm{phys}}}{\tau_{\mathrm{SO_2}}}\right)\right] \tag{3.5}$$

with $[X]$ being the mixing ratio, $\Delta[X]$ the change in mixing ratio, $M(X)$ the molecular mass and τ_X the chemical lifetime of species X.

Both the climatological values of OCS and SO_2 and their chemical lifetimes are taken from a latitude-altitude climatology at monthly resolution from the UPMC / Cambridge global two-dimensional chemistry-aerosol-transport model [Bekki and Pyle, 1992, 1993]. These quantities are shown in Figure 3.2. Using prescribed chemical lifetimes means that the OCS and SO_2 concentrations do not feed back onto concentrations of oxidants which oxidise these species. This is a limitation of our model, especially in situation of large OCS or SO_2 injection rates, which we discuss further in Sect. 4.4.2. In a future study the LMDZ-S3A model will be coupled to the REPROBUS (Reactive Processes Ruling the Ozone Budget in the Stratosphere) model for stratospheric chemistry that is also available in the LMDZ model [Lefèvre et al., 1994, 1998].

A schematic of the model species and physical processes is shown in Figure 3.3. The following processes are represented: aerosol nucleation from gaseous H_2SO_4, condensation and evaporation of gaseous H_2SO_4, coagulation and sedimentation of aerosol particles. Dry and wet deposition of gas-phase species and aerosols in the troposphere are also considered as we are interested in the tropospheric fate of the stratospheric aerosols.

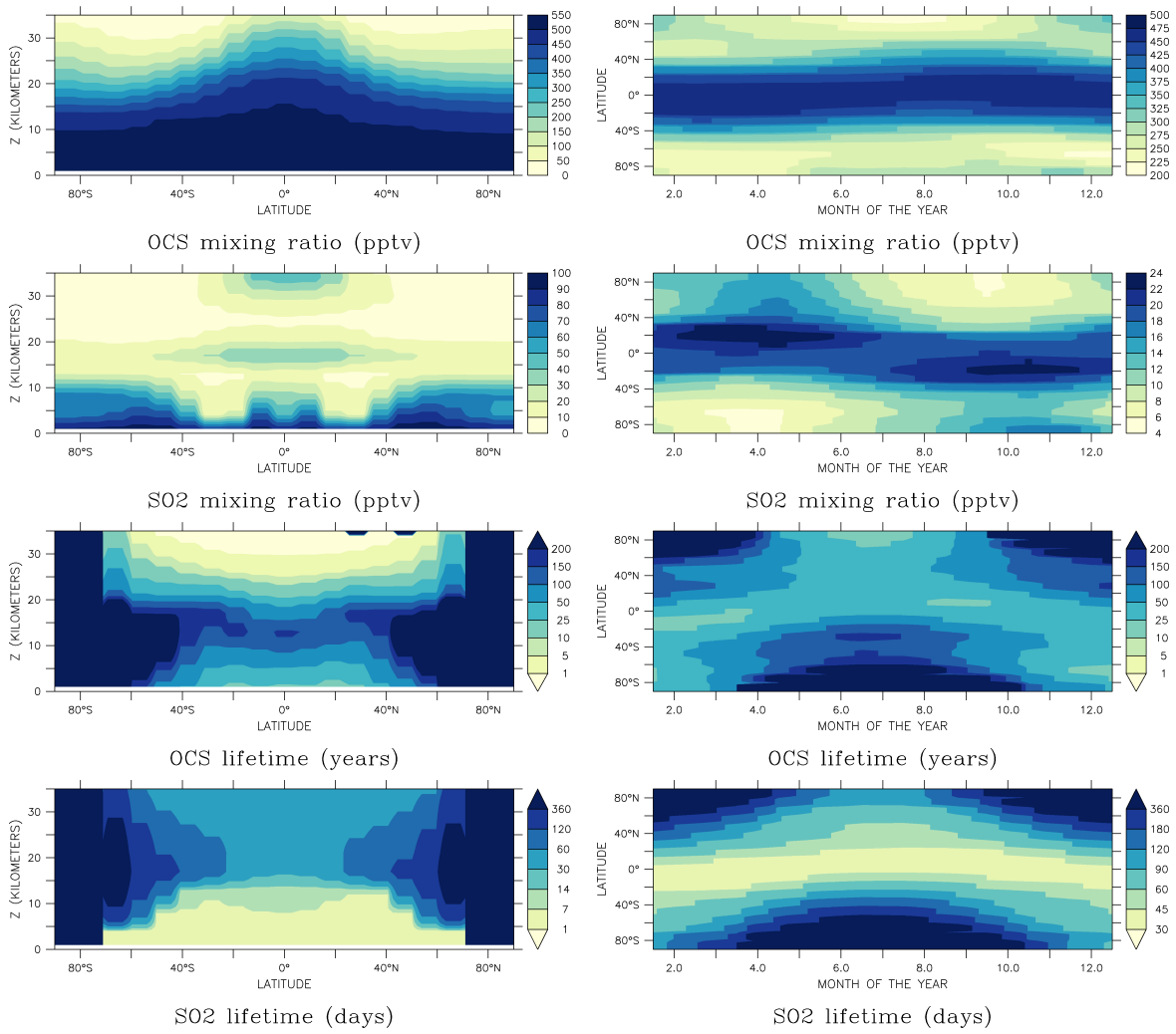

Figure 3.2: Climatological volume mixing ratios (upper half, in pptv) and lifetimes (lower half, in years or days) of OCS and SO_2 produced by the UPMC / Cambridge model and used as initial and boundary conditions for the LMDZ-S3A model. The left column shows the zonal and annual mean latitude-height distribution, while the right column shows an annual cycle of the zonal mean value at 20 km altitude.

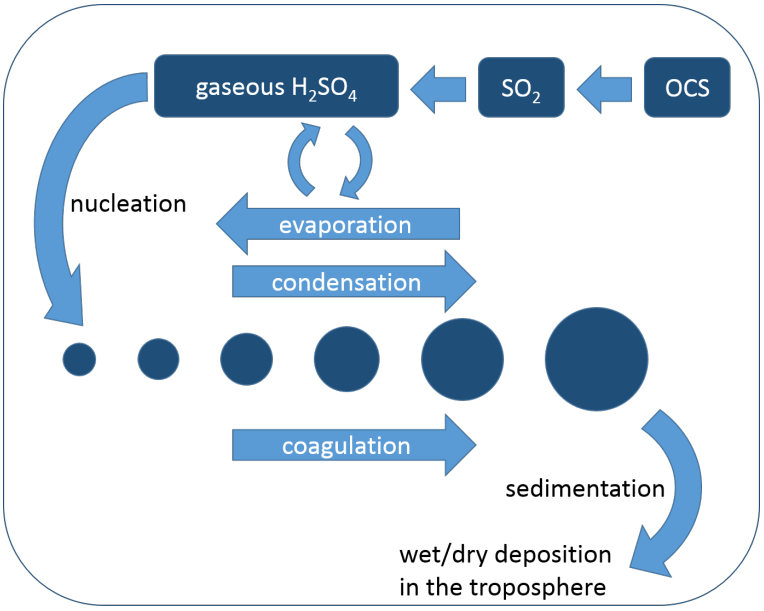

Figure 3.3: Schematic representation of the sulphur species and the processes affecting them that are represented in the LMDZ-S3A model.

3.3.3 Nucleation

The formation rate of new particles via binary homogeneous nucleation of sulphuric acid and water vapour is parametrised as a function of the sulphuric acid gas phase concentration, the relative humidity and the absolute temperature as described by Vehkamäki et al. [2002]. This parametrisation provides the nucleation rate J_{nuc} in unit of particles $\text{cm}^{-3}\,\text{s}^{-1}$, the total number of molecules in each nucleated particle N_{tot} and the mole fraction x of H_2SO_4 in the new particle. The equations are cumbersome and not repeated here, but it should be noted that we rely on the Fortran code provided by Vehkamäki et al. [2002].

The parametrisation is not valid any more under conditions where the number of molecules in the critical cluster is below 4 (which occurs mainly at large H_2SO_4 vapour concentrations). Under such conditions, we take the collision rate of two H_2SO_4 molecules as the nucleation rate instead [Hanna Vehkamäki, personal communication, 2015], i.e. $N_{\text{tot}} = 2$, $x = 1$ and

$$J_{\text{nuc}}\,(N_{\text{tot}} < 4) = [H_2SO_4]^2 \cdot \left(\frac{3\,\pi}{4}\right)^{1/6} \cdot \left(\frac{12\,k_B\,T}{M(H_2SO_4)}\right)^{1/2} \cdot (2\,V(H_2SO_4)^{1/3})^2 \quad (3.6)$$

with $M(H_2SO_4)$ the molecular mass of sulphuric acid, $[H_2SO_4]$ the concentration of H_2SO_4 (in molecules cm^{-3}), k_B the Boltzmann constant, and $V(H_2SO_4)$ the molecular volume of H_2SO_4 which is computed using Vehkamäki's density parametrisation.

In order to sort the new particles into the model size bins in a mass-conserving way, their volume is computed as

$$V_{\text{new}}^{\text{nuc}} = \frac{M(\text{H}_2\text{SO}_4)\; N_{\text{tot}}\; x}{\rho(\text{H}_2\text{SO}_4)} \tag{3.7}$$

with the density of sulphuric acid $\rho(\text{H}_2\text{SO}_4)$ taken at the reference temperature 293 K. The new particles are distributed among the size bins using a method inspired by the distribution factor $f_{i,j,k}$ from Jacobson et al. [1994] described in Sect. 3.3.6 and Eq. (3.19). Hereby for each new particle we add $f_k^{\text{nuc}} \cdot V_{\text{new}}^{\text{nuc}} / V_k$ particles to bin k, with $V_k = \frac{4}{3}\,\pi\, r_k^3$ and

$$f_k^{\text{nuc}} = \begin{cases} \left(\dfrac{V_{k+1} - V_{\text{new}}^{\text{nuc}}}{V_{k+1} - V_k}\right) \dfrac{V_k}{V_{\text{new}}^{\text{nuc}}} & \text{for } V_k \le V_{\text{new}}^{\text{nuc}} < V_{k+1}\ ;\ k < N_B \\ 1 - f_{k-1}^{\text{nuc}} & \text{for } V_{k-1} \le V_{\text{new}}^{\text{nuc}} < V_k\ ;\ k > 1 \\ 1 & \text{for } [V_{\text{new}}^{\text{nuc}} \le V_k\ ;\ k = 1] \text{ or } [V_{\text{new}}^{\text{nuc}} \ge V_k\ ;\ k = N_B] \\ 0 & \text{otherwise} \end{cases} \tag{3.8}$$

As a result the actual particle nucleation rate may deviate from Vehkamäki's parametrised value. For example, if the nucleated particles have only half the volume of a particle in the smallest model size bin, the number of new particles is only half of the parametrised value, but the H_2SO_4 flux from the gas to the particle phase is the same. We favoured conserving sulphur mass over conserving particle number concentration. This approximation on the exact value of the nucleation rate is not expected to have a very significant impact on the results because the particle size distribution is mainly determined by coagulation and condensation [English et al., 2011]. Furthermore this approximation is justified in the light of the large uncertainties arising from parametrizing nucleation rates using grid-box quantities (temperature, H_2O, H_2SO_4) that neglect sub-grid scale variations.

3.3.4 Condensation and evaporation of sulphuric acid

The change in size of the sulphate particles through gain from or loss towards the H_2SO_4 gas phase is computed based on the UPMC / Cambridge model parametrisation [Bekki and Pyle, 1992, 1993].

First the saturation vapour pressure of H_2SO_4 over a flat surface is calculated from a relationship given by Ayers et al. [1980] using the values of H_2SO_4 chemical potentials in aqueous phase listed in the work of Giauque et al. [1960, Table I]:

$$p_{\text{H}_2\text{SO}_4}^{\text{sat}}\ [\text{Pa}] = \frac{101325}{0.086} \cdot \exp\left(-\frac{10156}{T} + 16.259 + \frac{\mu - \mu_0}{R\,T}\right) \tag{3.9}$$

with T the temperature, μ the chemical potential and R the ideal gas constant. However, as recommended in Hamill et al. [1982], vapour pressures of H_2SO_4 from the Ayers et al. [1980] relationship are divided by 0.086 to obtain values close to the measurements of Gmitro and Vermeulen [1964].

We account for the Kelvin effect, whereby the saturation vapour pressure of H_2SO_4 over a curved surface is higher than the saturation vapour pressure over a flat surface. The saturation vapour pressure over a sulphate aerosol particle in size bin k, with radius r_k, is:

$$p^{\mathrm{sat},k}_{\mathrm{H_2SO_4}} = p^{\mathrm{sat}}_{\mathrm{H_2SO_4}} \cdot \exp\left(\frac{2\,\sigma\,M(\mathrm{H_2O})}{\rho_\mathrm{p}\,k_\mathrm{B}\,T\,r_k}\right) \tag{3.10}$$

with $M(H_2O)$ the molecular mass of water, σ the surface tension of the sulphuric acid solution (which is set to $72\,\mathrm{mN\,m^{-1}}$, the value for water at 20° C) and ρ_p the density of the sulphate particles. The corresponding H_2SO_4 number density at saturation is then

$$[\mathrm{H_2SO_4}]^{\mathrm{sat},k} = \frac{p^{\mathrm{sat},k}_{\mathrm{H_2SO_4}}}{k_\mathrm{B}\,T} \tag{3.11}$$

Then the flux of H_2SO_4 between the particle and the gas phase, $J_k(H_2SO_4)$, in molecules particle^{-1} s^{-1} is computed individually for every size bin k following Seinfeld and Pandis [2006, p. 542-547]

$$J_k(\mathrm{H_2SO_4}) = \pi\,r_k^2\,\bar{v}(\mathrm{H_2SO_4})\,\alpha \cdot \left([\mathrm{H_2SO_4}] - [\mathrm{H_2SO_4}]^{\mathrm{sat},k}\right) \cdot \frac{1 + Kn_k}{1 + Kn_k + \alpha/(2\,Kn_k)} \tag{3.12}$$

with the molecular accommodation coefficient $\alpha = 0.1$, $\bar{v}(H_2SO_4)$ the thermal velocity of a H_2SO_4 molecule and $Kn_k = \lambda/r_k$ the Knudsen number, where we use the parametrisation from Pruppacher and Klett [2010, p. 417] for the mean free path of air

$$\lambda = \lambda_0 \cdot \left(\frac{p_0}{p}\right) \cdot \left(\frac{T}{T_0}\right) \tag{3.13}$$

with $\lambda_0 = 6.6 \cdot 10^{-8}\,\mathrm{m}$ for air at the standard conditions $p_0 = 1013.25\,\mathrm{hPa}$ and $T_0 = 293.15\,\mathrm{K}$.

The growth (loss) rate due to condensation (evaporation) for typical stratospheric conditions is shown in Figure 3.4. It also illustrates the Kelvin effect, i.e. that the sulphuric acid vapour concentration threshold between evaporation and condensation is higher for smaller particles.

Evaporation from a particle over one time step is limited to its actual H_2SO_4 content and condensation is limited by the available H_2SO_4 vapour. How this is dealt with is further described in Sect. 3.3.5.

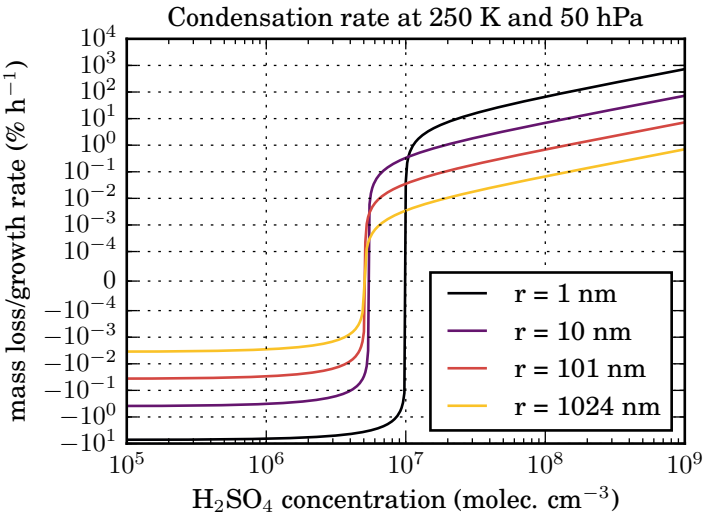

Figure 3.4: Mass growth rate (condensation rate relative to the particle mass, in % per hour) as a function of sulphuric acid vapour concentration for different particle radii at typical stratospheric conditions of 250 K and 50 hPa. A negative growth rate corresponds to evaporation. Note that the logarithmic y scale is linear between -10^{-4} and $+10^{-4}$ % h^{-1}.

Condensation (evaporation) has an impact on the particle size distribution, shifting particles to larger (smaller) size. To account for this, we first compute the new particle volume after adding the flux $J_k(H_2SO_4)$ over the timestep Δt:

$$V_{k,\text{new}}^{\text{c/e}} = V_k \cdot \left(1 + \frac{J_k(H_2SO_4)\Delta t}{N_k(H_2SO_4)}\right) \tag{3.14}$$

where $N_k(H_2SO_4)$ is the number of sulphuric acid molecules in a particle for bin k. Knowing this new volume of a particle coming from bin k and experiencing condensation or evaporation, the distribution among all the size bins (index l) can then be computed analogously to Eq. (3.8) and (3.19) using a factor:

$$f_{k,l}^{\text{c/e}} = \begin{cases} \left(\dfrac{V_{l+1} - V_{k,\text{new}}^{\text{c/e}}}{V_{l+1} - V_l}\right) \dfrac{V_l}{V_{k,\text{new}}^{\text{c/e}}} & \text{for } V_l \leq V_{k,\text{new}}^{\text{c/e}} < V_{l+1}\ ;\ l < N_B \\ 1 - f_{k,l-1}^{\text{c/e}} & \text{for } V_{l-1} \leq V_{k,\text{new}}^{\text{c/e}} < V_l\ ;\ l > 1 \\ 1 & \text{for } \left[V_{k,\text{new}}^{\text{c/e}} \leq V_l\ ;\ l = 1\right] \text{ or } \left[V_{k,\text{new}}^{\text{c/e}} \geq V_l\ ;\ l = N_B\right] \\ 0 & \text{otherwise} \end{cases} \tag{3.15}$$

3.3.5 Competition between nucleation and condensation

As both processes, nucleation and condensation, consume H_2SO_4 vapour while having very different effects on the particle size distribution, the competition between the two processes has to be handled carefully in a numerical model. Furthermore, this has to be done at an affordable numerical cost as we aim to perform long global simulations. We address this in the S3A module using an adaptive sub-timestepping. After computing the H_2SO_4 fluxes due to nucleation and condensation in kg H_2SO_4 s^{-1} from the initial H_2SO_4 mixing ratio, a sub-timestep, Δt_1, is computed such that the sum of both the nucleation and condensation fluxes consumes no more than 25% of the available ambient H_2SO_4 vapour:

$$\Delta t_1 = \min\left(0.25 \cdot \frac{[H_2SO_4]_0}{J_{\text{nuc}} + J_{\text{cond}}}\ ,\ \Delta t_{\text{phys}}\right) \tag{3.16}$$

where Δt_{phys} is the main timestep (30 minutes in our case), and $[H_2SO_4]_0$ is the H_2SO_4 mixing ratio at the beginning of the timestep. Hence, neither one of the two processes can use up all the sulphuric acid at the expense of the other process. This sub-timestepping procedure is repeated up to 4 times with a sub-timestep equal to

$$\Delta t_{1<i<4} = \min\left(0.25 \cdot \frac{[H_2SO_4]_0}{J_{\text{nuc}} + J_{\text{cond}}}\ ,\ \Delta t_{\text{phys}} - \sum_{j=1}^{i-1} \Delta t_j\right) \tag{3.17}$$

where J_{nuc} and J_{cond} are updated at each timestep according to the updated value of $[H_2SO_4]$. The fourth and final sub-timestep is chosen so that the sum of all sub-timesteps is equal to one timestep of the model atmospheric physics Δt_{phys}.

$$\Delta t_4 = \max\left[\min\left(0.25 \cdot \frac{[H_2SO_4]_0}{J_{\text{nuc}} + J_{\text{cond}}}, \Delta t_{\text{phys}} - \sum_{j=1}^{3} \Delta t_j\right)\ ,\ \Delta t_{\text{phys}} - \sum_{j=1}^{3} \Delta t_j\right] \tag{3.18}$$

This joint treatment of nucleation and condensation is imperfect but it has the advantage of being much more computationally efficient than usual solutions consisting of taking very short timesteps and much simpler than a simultaneous solving of nucleation and coagulation. The number of sub-timesteps could be increased for increased numerical accuracy, however a number of 4 sub-timesteps was considered to be sufficient. It should be noted that the processes of nucleation and condensation, as well as their competition, are only activated in the stratosphere.

3.3.6 Coagulation

The growing of sulphate particles through coagulation is represented through the semi-implicit, volume-conserving numerical scheme described in Jacobson et al. [1994]. It is unconditionally stable even for timesteps of the order of hours. We restricted the coagulation kernel only to its main component, i.e. Brownian motion. Secondary components of coagulation due to convection, gravitation, turbulence or inter-particle van der Waals forces are neglected, which may partly explain the underestimation of particle size in Chapter 4. Sensitivity studies performed by English et al. [2013] and Sekiya et al. [2016] simulating the 1991 eruption of Mount Pinatubo found that including inter-particle van der Waals forces increased the peak effective radius by 10 % and decreased stratospheric AOD and burden by 10 %. Given that there are only few measurements on the van der Waals coagulation term, and the mixed results obtained in our model (see Sect. 4.4.1), we do not include this process in our default model, but offer it as an option in the code of the model (using the enhancement factors from Eq. (29) and (30) in Chan and Mozurkewich [2001]). Coagulation is only activated in the stratosphere.

For convenience, we repeat here the equations from Jacobson et al. [1994]. New particles resulting from the coagulation of particles from size bins i and j have a combined particle volume $V_{i,j} = V_i + V_j$. They are distributed among the size bins according to the following definition of the distribution factor $f_{i,j,k}$:

$$f_{i,j,k} = \begin{cases} \left(\dfrac{V_{k+1} - V_{i,j}}{V_{k+1} - V_k} \right) \dfrac{V_k}{V_{i,j}} & \text{for } V_k \leq V_{i,j} < V_{k+1} \; ; \; k < N_B \\ 1 - f_{i,j,k-1} & \text{for } V_{k-1} \leq V_{i,j} < V_k \; ; \; k > 1 \\ 1 & \text{for } V_{i,j} \geq V_k \; ; \; k = N_B \\ 0 & \text{otherwise} \end{cases} \tag{3.19}$$

As discussed previously, the same distribution factor is applied for the other physical processes affecting particle size (i.e., nucleation, and the net effect from condensation and evaporation). To our knowledge, this is an original feature of our model. It should be noted that we have favoured conservation of aerosol mass (and volume) over conservation of aerosol number in all these processes.

The semi-implicit approach gives the following equation for the concentration of particles in bin k after coagulation over a timestep Δt:

$$V_k \, C_k^{(t+1)} = \frac{V_k \, C_k^{(t)} + \Delta t \sum\limits_{j=1}^{k} \left(\sum\limits_{i=1}^{k-1} f_{i,j,k} \, \beta_{i,j} \, V_i \, C_i^{(t+1)} \, C_j^{(t)} \right)}{1 + \Delta t \sum\limits_{j=1}^{N_B} \left(1 - f_{k,j,k} \right) \beta_{k,j} \, C_j^{(t)}} \tag{3.20}$$

with $C_k^{(t)}$ the particle concentration in bin k at timestep t, $C_k^{(t+1)}$ the particle concentration in bin k at timestep $t+1$, and $\beta_{i,j}$ the coagulation kernel. For purely Brownian coagulation, the kernel has the form

$$\beta_{i,j}^{B} = \frac{4\,\pi\,(r_i + r_j)(D_i + D_j)}{\dfrac{r_i + r_j}{r_i + r_j + (\delta_i^2 + \delta_j^2)^{1/2}} + \dfrac{4(D_i + D_j)}{(\bar{v}_{\mathrm{p},i}^2 + \bar{v}_{\mathrm{p},j}^2)(r_i + r_j)}} \tag{3.21}$$

with the particle diffusion coefficient

$$D_i = \frac{k_\mathrm{B}\,T}{6\,\pi\,r_i\,\eta}\left[1 + Kn_i\left(1.249 + 0.42\cdot\exp\left(\frac{-0.87}{Kn_i}\right)\right)\right] \tag{3.22}$$

where η is the dynamic viscosity of air, the thermal velocity of a particle in bin i with mass m_i

$$\bar{v}_{\mathrm{p},i} = \sqrt{\frac{8\,k_\mathrm{B}\,T}{\pi m_i}} \tag{3.23}$$

the mean distance from the centre of a sphere reached by particles leaving the surface of the sphere and travelling a distance of the particle mean free path $\lambda_{\mathrm{p},i}$

$$\delta_i = \frac{(2\,r_i + \lambda_{\mathrm{p},i})^3 - (4\,r_i^2 + \lambda_{\mathrm{p},i}^2)^{3/2}}{6\,r_i\,\lambda_{\mathrm{p},i}} - 2\,r_i \tag{3.24}$$

and the particle mean free path

$$\lambda_{\mathrm{p},i} = \frac{8\,D_i}{\pi\,\bar{v}_{\mathrm{p},i}} \tag{3.25}$$

The Brownian coagulation kernel β^B for typical stratospheric conditions is shown in Figure 3.5. The coagulation probability is highest if one particle is small and the other one is large, while it is several orders of magnitude lower for particles of identical size.

3.3.7 Aerosol chemical composition and density

The weight fraction of H_2SO_4 in the aerosol as a function of temperature and H_2O partial pressure is computed following the approach described in Steele and Hamill [1981] and also used in Tabazadeh et al. [1997]. In this approach, the water content of the aerosol particles is assumed to be in equilibrium with the surrounding ambient water vapour. The composition is assumed to be constant over the whole particle size range.

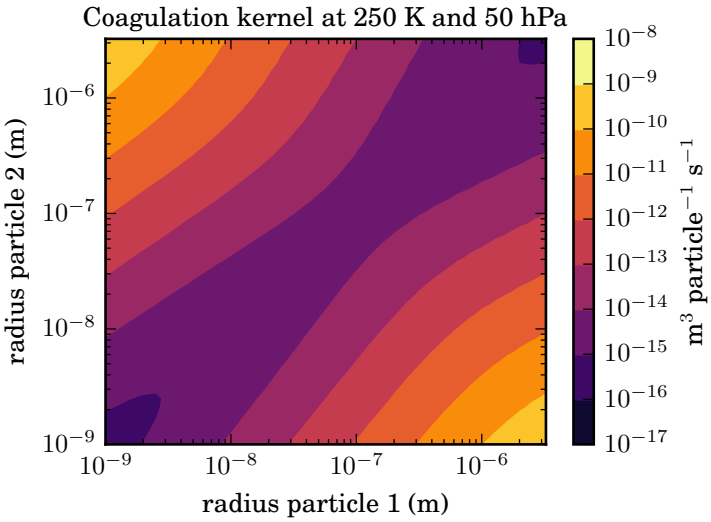

Figure 3.5: Brownian coagulation kernel for particles in the size range covered by the LMDZ-S3A model at typical stratospheric conditions of 250 K and 50 hPa.

The aerosol particle density as a function of temperature and H_2SO_4 weight fraction $w_{H_2SO_4}$ (in %) can then be computed from the rough approximation

$$\rho_p = \left(A \cdot w_{H_2SO_4}^2 + B \cdot w_{H_2SO_4} + C\right) \cdot \left(1 - \frac{0.02}{30}\left(T - 293\right)\right) \tag{3.26}$$

with the constants $A = 7.8681252 \cdot 10^{-6}$, $B = 8.2185978 \cdot 10^{-3}$, $C = 0.97968381$, and T in K.

3.3.8 Sedimentation

Particles in the stratosphere sediment due to gravity with a velocity depending on their size and density and ambient pressure. The Stokes sedimentation velocity (with Cunningham correction) of a particle in size bin k is given by

$$v_{\text{sed},k} = \frac{2\,g\,r_k^2\,(\rho_\text{p} - \rho_\text{air})}{9\,\eta}\left[1 + Kn_k\left(1.257 + 0.4 \cdot \exp\left(\frac{-1.1}{Kn_k}\right)\right)\right] \tag{3.27}$$

with the gravity g, the particle density ρ_p and the air density ρ_air.

The sedimentation process is computed with a semi-implicit scheme as described in Tompkins [2005]. The concentration of particles in a bin k (omitted here for clarity) in the model layer j (with j numbered from the top of the atmosphere to the surface) after

sedimentation at timestep $t+1$ is given by:

$$C_j^{(t+1)} = \frac{C_j^{(t)} + C_{j-1}^{(t+1)} \cdot \frac{\rho_{j-1}\, v_{j-1}}{\rho_j\, \Delta z_j} \Delta t_{\text{phys}}}{1 + \frac{\rho_j\, v_j}{\rho_j\, \Delta z_j} \Delta t_{\text{phys}}} \tag{3.28}$$

with v_j the sedimentation velocity, ρ_j the air density and Δz_j the thickness of layer j. The scheme is solved downwards, it is very stable, and a timestep Δt_{phys} of 30 minutes is appropriate for our model vertical resolution. Unlike the aerosol processes described above, it is active not only above but also below the tropopause. It is applied to all bins of the aerosol size distribution but only has a noticeable impact on larger particle bins.

Once the particles cross the tropopause they are rapidly removed from the troposphere through wet and dry deposition. Parametrisations of dry and wet scavenging are those of the LMDZ model and are not described here as they have minimal impact on the aerosol stratospheric aerosol layer. They are nevertheless important to model the tropospheric fate and impact at the surface of aerosols or aerosol precursors injected in the stratosphere.

3.3.9 Aerosol optical properties

Averaged optical properties of the particles (extinction cross section σ_i in m^2 per particle in bin i, asymmetry parameter g_i and single scattering albedo ω_i) are computed for each of the 6 SW and 16 LW spectral bands of the radiative transfer scheme using refractive index data from Hummel et al. [1988]. We use our own Mie routine derived from Wiscombe [1979]. In the SW, we account for variations of the incoming solar radiation within each band by computing aerosol optical properties at a higher spectral resolution (24 spectral bands) and weighting the properties with a typical solar spectrum. In the LW, we account for variations in the refractive index of the aerosols within each band by computing aerosol optical properties at a higher spectral resolution and weighting the properties with a black body emission spectrum using a typical stratospheric temperature of 220 K. To avoid Mie resonance peaks in the aerosol optical properties, we subdivide each aerosol size bin into 10 intervals which are logarithmically spaced and assume a uniform distribution within the size bin for computing average properties. For very small Mie parameters ($x < 0.001$), which occurs for the smallest particle bins and the longest wavelengths in the infrared, we extrapolate the Mie properties computed for $x = 0.001$ for numerical stability using the known asymptotic behaviour of the scattering and absorption properties. Aerosol optical properties are computed once for each aerosol bin assuming a constant sulphuric acid mass mixing ratio of 75% and a temperature of 293 K (conditions for which the refractive index was measured).

Figure 3.6 shows as an example the sulphate mass extinction coefficient over the modelled particle size range and in all the SW and LW spectral bands.

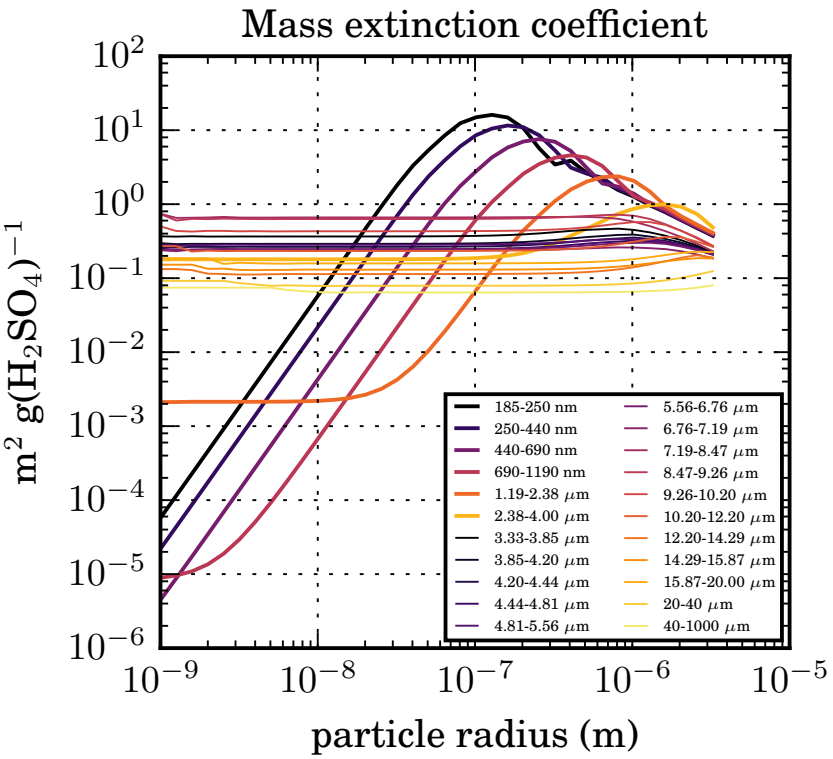

Figure 3.6: Modelled mass extinction coefficient of sulphate aerosol in $m^2\,g(H_2SO_4)^{-1}$ as a function of dry particle radius in the 6 SW (bold lines) and 16 LW (thin lines) spectral bands of the LMDZ-S3A model.

The bin-wise optical properties are then integrated over the size distribution at every time step according to the actual local size distribution. Hence, the optical depth τ_k, the single scattering albedo ω_k and the asymmetry parameter g_k in model layer k with particle concentrations $C_{i,k}$ (in particles m^{-3}) and the vertical extent Δz_k (in m) can be computed for each spectral band as

$$\tau_k = \sum_{i=1}^{N_B} \sigma_i\, C_{i,k}\, \Delta z_k \tag{3.29}$$

$$\omega_k = \frac{1}{\tau_k} \sum_{i=1}^{N_B} \omega_i\, \sigma_i\, C_{i,k}\, \Delta z_k \tag{3.30}$$

$$g_k = \frac{1}{\tau_k\, \omega_k} \sum_{i=1}^{N_B} g_i\, \omega_i\, \sigma_i\, C_{i,k}\, \Delta z_k \tag{3.31}$$

Aerosol optical properties are also computed at specific wavelengths (443, 550, 670, 765, 865, 1020 nm and 10 μm) for diagnostic purpose. It should be noted that in the LW, the RRTM model neglects scattering and only accounts for absorption. Hence we only feed the model with the LW absorption optical depth at each model layer.

3.3.10 Model code availability

The code of S3A can be downloaded along with the LMDZ model from `http://lmdz.lmd.jussieu.fr`. S3A code is mostly contained within a separate directory (StratAer) of the model physics and is activated at compilation with a CPP key. A model configuration (LMDZORSTRATAER_v6) containing the S3A module is also available within the modipsl/libIGCM model environment of the IPSL Earth System Model (`http://forge.ipsl.jussieu.fr/igcmg_doc`).

3.4 Conclusions on the model

In this chapter we presented the newly developed sectional stratospheric sulphate aerosol (S3A) module as part of the LMDZ atmospheric general circulation model. A strength of our model is that it can readily be coupled to other components of the IPSL climate (and Earth system) model to perform climate studies. The S3A module includes a representation of sulphate particles with dry radii between 1 nm and 3.3 μm in currently 36 size bins, as well as the precursor gases OCS, SO_2 and H_2SO_4. The aerosol-relevant physical processes of nucleation, condensation, evaporation, coagulation and sedimentation are represented in accurate, mass-conserving routines with reasonable computational cost, together with interactive aerosol optical properties and radiative transfer in 6 solar (SW) and 16 terrestrial (LW) spectral bands. The tropospheric fate of stratospheric sulphate aerosols is also simulated. Our model strength lies in the representation of aerosol microphysics with robust numerical schemes, but the model also has a few limitations. In particular it is simplified in terms of stratospheric chemistry, but this may be the subject of future work, as LMDZ-S3A can be coupled to the REPROBUS model which is also part of the IPSL Earth system model. Further developments may also include a more comprehensive treatment of the coagulation kernel and the possible interactions with other aerosol types (organics and meteoritic dust) in the stratosphere. In the following chapter, we will describe the validation of the model by comparing simulation results with observations from periods of low and high stratospheric aerosol loading.

4 Evaluation of the LMDZ-S3A model

In this chapter, which is also based on the publication by Kleinschmitt et al. [2017a], we will evaluate the performance of the LMDZ-S3A model against available observations. The eruption of Mount Pinatubo in June 1991 is the last major eruption experienced by the Earth and was relatively well observed. As such it is a useful case study for any stratospheric aerosol model and is discussed in Section 4.1 and Section 4.3, whereas we analyse the modelled non-volcanic background aerosol in Section 4.2.

4.1 Validation of aerosol optics and radiative transfer

In a first step, we validate the part of the model computing the optical properties and the radiative forcing of the stratospheric sulphate aerosol. For this purpose, we performed a simulation of the period 1986 to 1994 including the eruption of Mount Pinatubo with a model version without any microphysics and with prescribed historical sea surface temperatures (SSTs). The spatial and temporal distribution of the stratospheric aerosol optical depth (AOD) at 550 nm was taken from the observation-based NOAA-GISS model data by Sato [2012]. The AOD in the model's 6 SW and 16 LW spectral bands was then calculated relative to 550 nm for a bimodal particle size distribution adapted from Deshler et al. [2003] (with radii $r_1 = 0.13\,\mu m$, $r_1 = 0.41\,\mu m$, see Figure 5a therein). In order to compare the simulated radiative forcing to satellite observations from the Earth Radiation Budget Experiment (ERBE), the anomalies in SW and LW fluxes at the top of the atmosphere (TOA) were calculated by removing a linear trend and subtracting a mean annual cycle from 1986 to 1990 (as it was done by Soden et al. [2002]). Averages are given for 60°S to 60°N, because the ERBE data are restricted to these latitudes. Figure 4.1 shows a similar evolution of the observed and the modelled anomalies for the three ensemble members, i.e. model experiments with slightly different initial conditions. It has to be noted that the decrease in outgoing LW radiation is partly due to the aerosol's LW absorption and partly due to the surface cooling following the eruption. Given the limitations of the measurements, of the input AOD distribution, and of the prescribed fixed particle size distribution, the agreement can be qualified as good, suggesting that the interactions of the stratospheric aerosol with SW and LW radiation are well represented in our model.

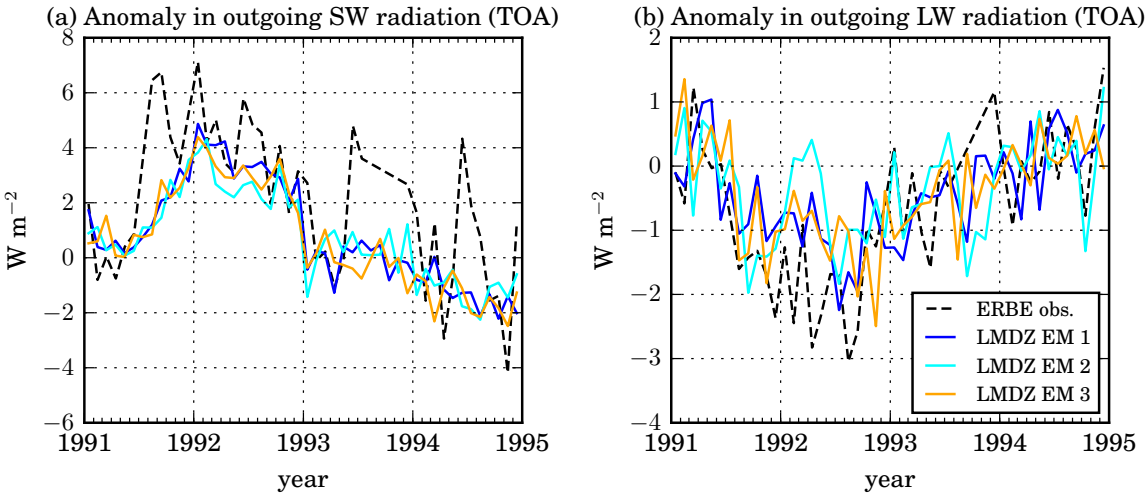

Figure 4.1: Comparison of the observed and the simulated top-of-the-atmosphere (TOA) anomaly in the outgoing (a) SW and (b) LW radiation following the eruption of Mount Pinatubo in June 1991. The black dashed line shows the ERBE satellite measurements, while the coloured solid lines show model results from three different ensemble members (EM) with slightly different initial conditions.

4.2 Non-volcanic background aerosol

The capability of our model to simulate a reasonable background stratospheric sulphate aerosol is tested by running the full model for a decade with climatological OCS and SO_2 concentrations and lifetimes as the only boundary conditions. In this setup the model is not nudged to meteorological reanalysis.

The self-evolving aerosol distribution reaches a steady state or equilibrium (subject to seasonal variations) after about 5 years. In this steady state the global mean stratospheric aerosol optical depth (SAOD) at 550 nm is 0.002, which is in good agreement with the observed SAOD of 0.002-0.0025 at 525 nm (in the tropics and at mid-latitudes) during the period of very low stratospheric sulphur loading around the year 2000 [e.g., Vernier et al., 2011]. The global stratospheric aerosol burden is 0.08 Tg S and the mean dry effective radius is 62 nm. The dry effective radius increases to 106 nm if only particles with radius larger than 50 nm, which make up 84 % of the burden, are taken into account.

Figure 4.2 shows that the aerosol layer is distributed over the whole globe, but is thicker and lower in altitude at high latitudes than in the tropics. The SAOD is highest at the summer pole. Unfortunately, there are too few observations and datasets (with a clear delineation of the tropopause) to validate or invalidate the latitudinal and seasonal background aerosol distribution generated by our stratospheric aerosol model.

The comparison of the modelled particle size distribution at different latitudes shows that there are almost as many small particles at the Equator as at mid and high latitudes, but considerably less in the optically relevant size range. The aerosol layer is zonally quite homogeneous with deviations from the zonal mean value within $\pm 15\,\%$ for optical depth and $\pm 25\,\%$ for effective radius around 30° N/S and within $\pm 5\,\%$ at low and high latitudes.

In Figure 4.3 we compare the modelled size of the background aerosol to OPC measurements in May 2000, a period of very low stratospheric sulphate aerosol burden. While the modelled concentrations of particles with radius $r > 0.01\,\mu m$ and $r > 0.15\,\mu m$ in the lower stratosphere (below 19 km) match the observations quite well, the deviation increases with altitude. The concentration of larger particles with radius $r > 0.5\,\mu m$ is underestimated everywhere by the model by roughly one order of magnitude. This may be due to the fact that the observations are from a period still slightly influenced by precedent eruptions, i.e. not from pure background conditions. But the model is also missing secondary sources of stratospheric aerosol (e.g., tropospheric aerosols and meteoritic dust), which might be relevant in such a background case.

Figure 4.4 shows the modelled stratospheric sulphur budget under background conditions in steady state (11^{th} year). Interestingly, the major part of the stratospheric SO_2 comes from the troposphere and only a minor part from the conversion of OCS occurring above the tropopause. This might be partly caused by the relatively long lifetime of OCS (here 8 years on average). The SO_2 is converted to H_2SO_4 with a lifetime of 36 days, while sulphuric acid has a lifetime of 44 days with respect to conversion into particles (considering both nucleation and condensation). The relatively short aerosol lifetime of 233 days can be explained by the fact that most of the aerosol is only slightly above the tropopause and at high latitudes, where it can enter the troposphere more easily and gets removed quickly via wet and dry deposition.

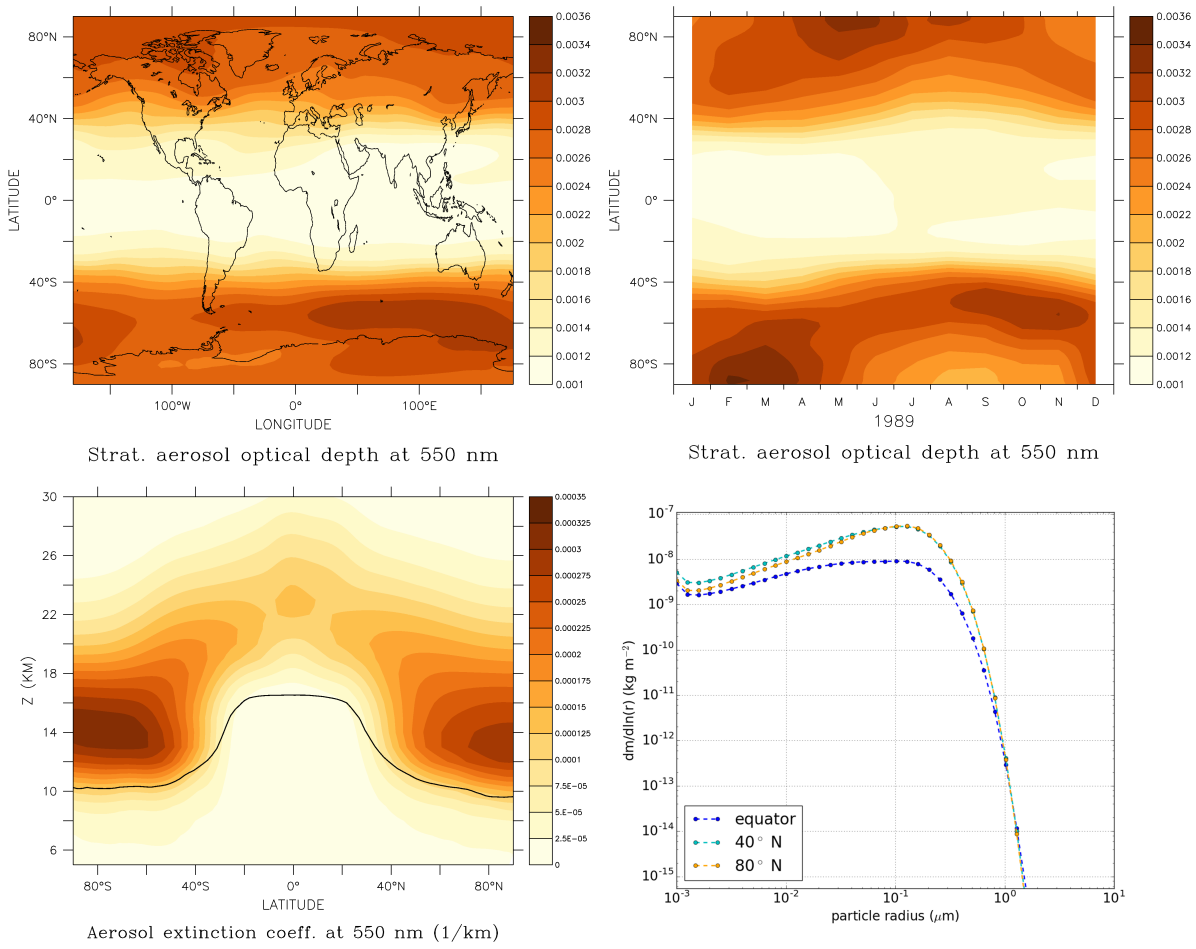

Figure 4.2: Upper left panel: Annual mean latitude-longitude distribution of the stratospheric AOD at 550 nm. Upper right panel: Zonal mean latitude-time distribution of the stratospheric AOD at 550 nm. Lower left panel: Zonal mean latitude-height distribution of stratospheric aerosol extinction coefficient (km^{-1}) at 550 nm. Lower right panel: Vertically integrated mass size distribution at different latitudes (in $kg\,m^{-2}$). All variables are from the 10^{th} year of the simulation with no volcanic input in the stratosphere and are assumed to represent a steady state.

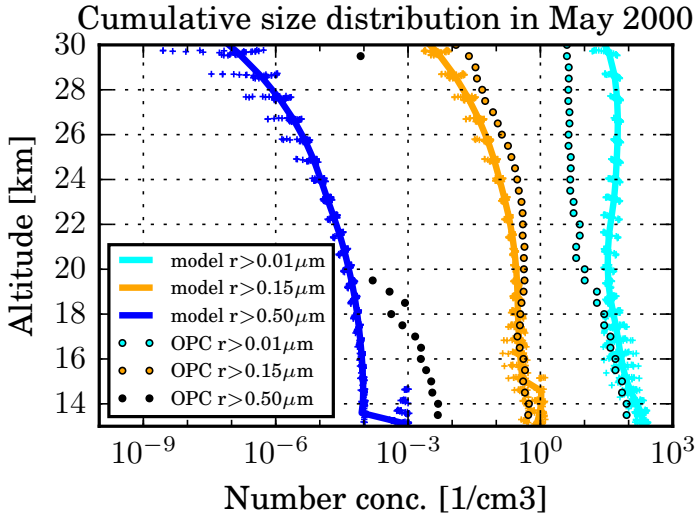

Figure 4.3: Vertical profile of the cumulative aerosol number concentration (cm^{-3}) for three channels ($r > 0.01$ µm in light blue, $r > 0.15$ µm in orange, and $r > 0.5$ µm in dark blue) at Laramie, Wyoming (41° N, 105° W) plotted in the style of Sekiya et al. [2016]. Solid lines show the modelled monthly mean, while the crosses indicate the range of daily mean concentrations within that month. Optical particle counter (OPC) measurements from Deshler et al. [2003] are shown as circles.

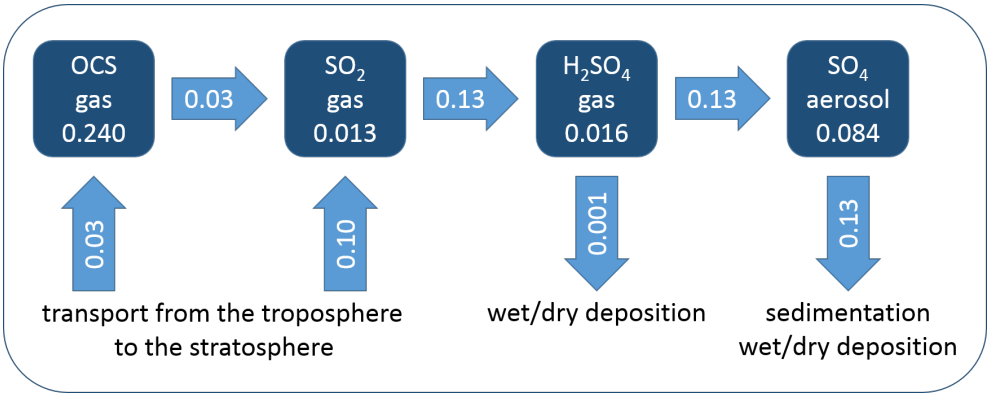

Figure 4.4: Modelled annual mean stratospheric burden (in Tg S) and fluxes (in Tg S yr^{-1}) of the represented sulphur species. The values are given for steady state background conditions without any stratospheric volcanic emissions. Sedimentation and advection can take the species out of the stratosphere into the troposphere, where they can be removed by wet and dry deposition.

4.3 Mount Pinatubo 1991 eruption

The eruption of Mount Pinatubo (Philippines) in June 1991 was the largest of the 20th century. Observations of the volcanic aerosols in the following months and years offer a unique opportunity to evaluate the performance of stratospheric aerosol models such as LMDZ-S3A under conditions of relatively high stratospheric sulphate loading.

In order to get a realistic spatial distribution of the aerosols in the simulation, horizontal winds are nudged to ECMWF ERA-interim reanalysis fields and sea surface temperatures (SSTs) are prescribed to their historical values. The simulation is initialised in January 1991 from the end of the 10 year spin up simulation with background conditions (see Sect. 4.2). On June 15 1991, 7 Tg S in the form of SO_2 are injected into the grid cell including Mount Pinatubo at 15° N and 120° E over a period of 24 hours and vertically distributed as a Gaussian profile centred at 17 km altitude with a standard deviation of 1 km. This initial height was adjusted as a free parameter after comparing the resulting aerosol distribution of simulations with emission at 16, 17 and 18 km to observations (see Figure 4.5). This injection height may seem quite low compared to other simulations of the eruption, but it should be recalled that our model takes into account the interaction of aerosols with the radiation. The evolving aerosol has a net heating effect on the surrounding air through absorption of solar and terrestrial radiation (only partly compensated by emission of terrestrial radiation), which (together with the ascending branch of the Brewer-Dobson circulation) causes a significant uplift of the volcanic aerosol plume to more than 25 km altitude three months after the eruption. This radiatively driven uplift was already described by Aquila et al. [2012], who also found the best agreement between the simulated and the observed sulphate cloud if the SO_2 is injected at an altitude of 16 to 18 km.

4.3.1 Aerosol distribution and size

The resulting spatial distribution of the aerosol extinction coefficient is compared to satellite and ground-based observations that are compiled in the CMIP6 aerosol data set [Luo Beiping, personal communication, 2016; also see Revell et al. [2017]] in Figure 4.5. The simulation with emission of SO_2 at 17 km was selected as the best fit, because the height of the maximum extinction coefficient at 1020 nm in September and December 1991 is closest to the CMIP6 data. In contrast, emission at 16 km results in faster meridional transport in the lower stratosphere and therefore a too fast decrease in aerosol extinction after the eruption, while emission at 18 km produces an aerosol layer considerably higher in altitude than observed.

The modelled evolution of the SAOD at 550 nm is also compared to a climatology from Sato [2012] and to SAOD simulated with the WACCM model by Mills et al. [2016] in Figure 4.6. The global mean SAOD increases a little faster in LMDZ-S3A than in the

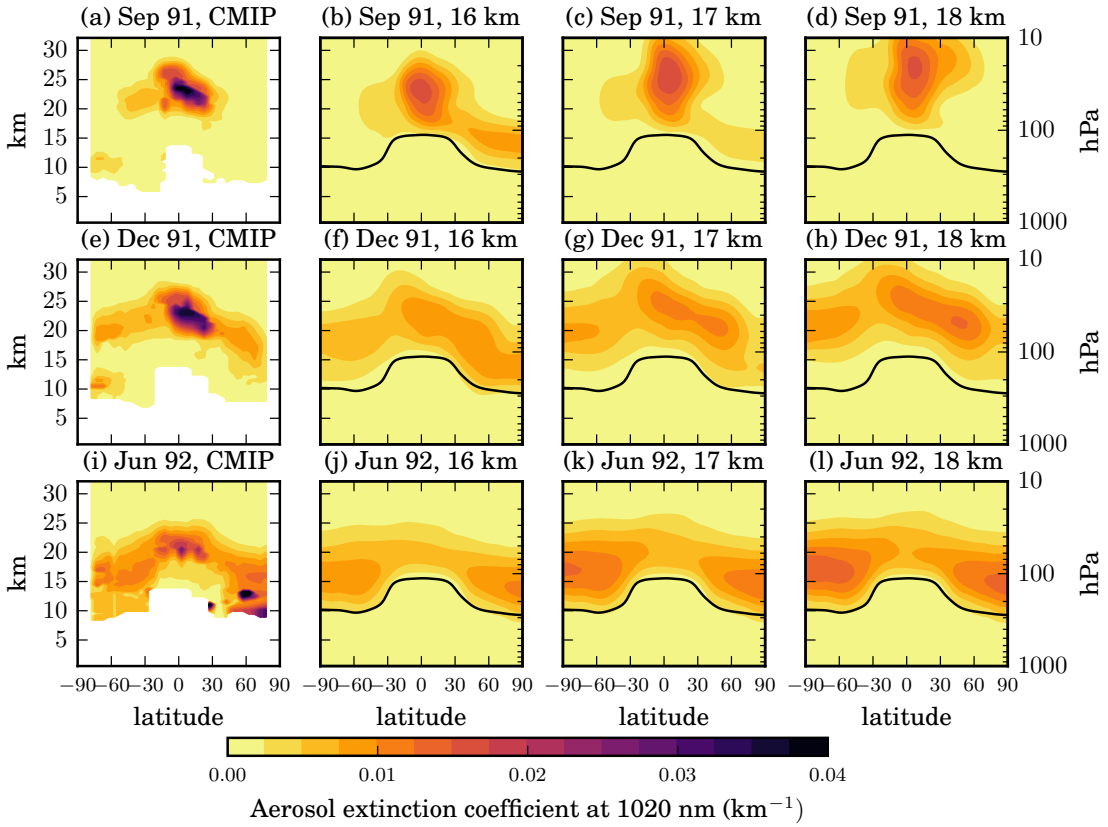

Figure 4.5: Temporal evolution of the zonal mean aerosol extinction coefficient (km^{-1}) at 1020 nm. Monthly mean latitude-height distributions in September 1991 (first row), December 1991 (second row) and June 1992 (third row). Observation-based CMIP6 aerosol data set (first column), simulations with emission of SO_2 at 16 km (second column), 17 km (third column) and 18 km (fourth column). The vertical axis shows the height in km and the black line indicates the modelled tropopause.

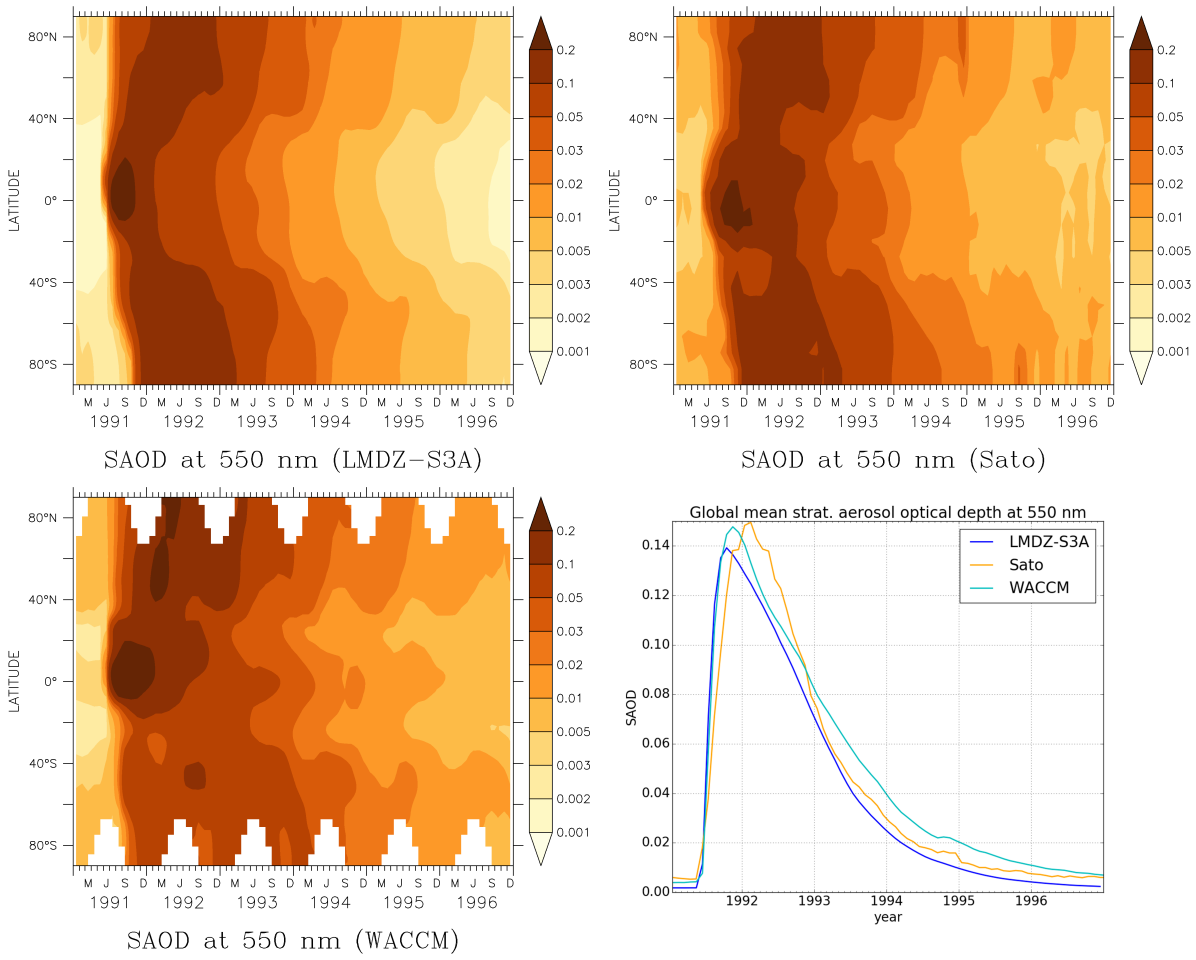

Figure 4.6: Evolution of the zonal mean stratospheric aerosol optical depth (SAOD) at 550 nm modelled with LMDZ-S3A (upper left panel) compared to the climatology from Sato [2012] (upper right panel) and to SAOD simulated with WACCM by Mills et al. [2016] (lower left panel), as well as the global mean SAOD (lower right panel). Note that unlike our simulation, WACCM includes small volcanic eruptions that occurred after that of Mount Pinatubo.

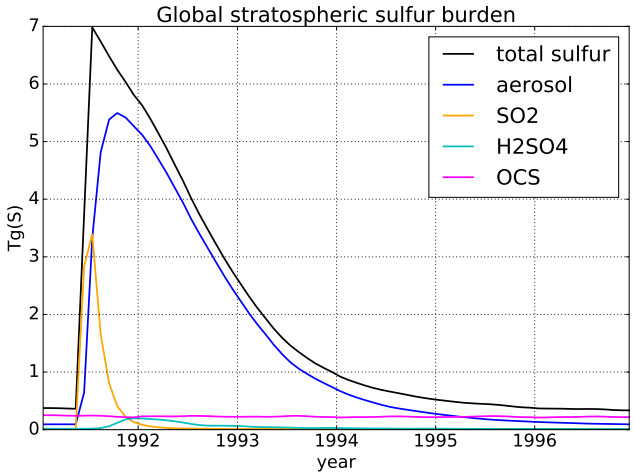

Figure 4.7: Evolution of the stratospheric sulphur burden and its distribution among the different species modelled with LMDZ-S3A for the period from January 1991 to December 1996, including the Pinatubo eruption (but no other eruptions).

Sato climatology, but just as fast as in WACCM. LMDZ-S3A slightly underestimates the maximum value of 0.15 from the Sato climatology and decreases at approximately the same rate of 7-8 % per month, while the decrease in WACCM, which includes several minor volcanic eruptions after Pinatubo, is slower. All three latitudinal distributions of the zonal mean SAOD are overall in good agreement, but with an earlier decrease in the tropics in LMDZ-S3A and with a stronger asymmetry towards the northern hemisphere in the WACCM simulation (probably also due to the included minor volcanic eruptions after Pinatubo).

Figure 4.7 shows that the 7 Tg S emitted as SO_2 during the eruption are quickly converted into particles. The aerosol burden reaches its maximum 4 months after the eruption and then decreases slowly until it reaches a background value again after 4 to 5 years. The H_2SO_4 burden increases more slowly than the aerosol, probably because it requires more time to transport the sulphur to the higher stratosphere. This is the only region where a larger reservoir of sulphuric acid vapour can remain because particles tend to evaporate at the local temperature and pressure.

Particle size is compared to the continuous optical particle counter (OPC) measurements by Deshler et al. [2003] at 41° N in Figure 4.8 and Figure 4.9. The modelled stratospheric effective particle radius in the grid cell containing Laramie, Wyoming (41° N, 105° W) is somewhat lower than measured by the OPC, but mostly within the given uncertainty of the measurement, if one takes into account particles of all sizes. However the sensitivity of the OPC to small particles with a radius below 0.15 µm (the smallest size class measured directly by the OPC) is not very well known. If only particles with a dry radius above 0.15 µm are considered and the smaller ones are completely ignored in the model, the effective radius is mostly overestimated by the

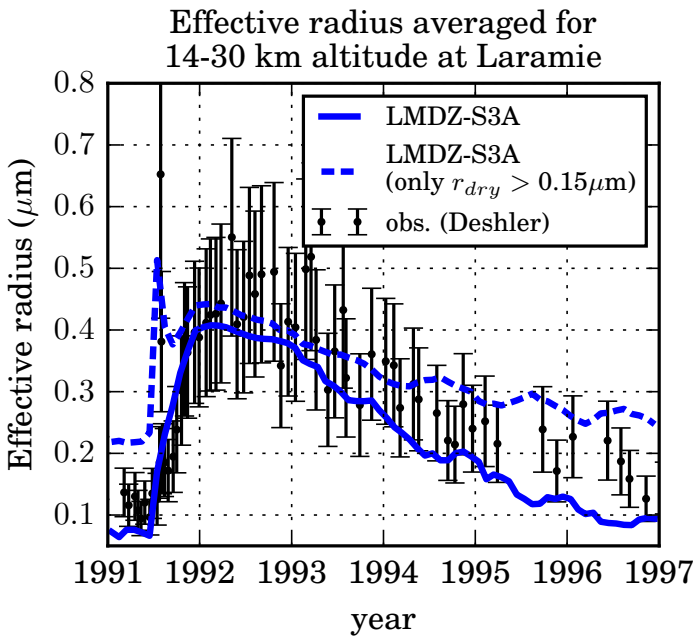

Figure 4.8: Stratospheric effective particle radius (in µm) at Laramie, Wyoming (41° N, 105° W) as simulated by the LMDZ-S3A model and observed with optical particle counters [Deshler et al., 2003]. Error bars of the measurements were determined from the 40 % uncertainty in aerosol surface area A and volume V assuming a correlation coefficient of 0.5 between A at different altitudes, V at different altitude and A and V at the same altitude.

model. But as the OPC's sensitivity to the small particles can be assumed to lie in between these two extreme cases (all or nothing), the agreement between modelled and observed particle size may be judged as good.

In Figure 4.9 the modelled and the observed particle size distributions 5, 11 and 17 months after the eruption are compared. The model tends to overestimate particle concentrations of all size bins in the higher stratosphere, but reproduces the observations of $r > 0.01$ µm and $r > 0.15$ µm particles fairly well at lower levels. The concentration of $r > 0.5$ µm particles is underestimated at the height of highest concentrations (17–21 km).

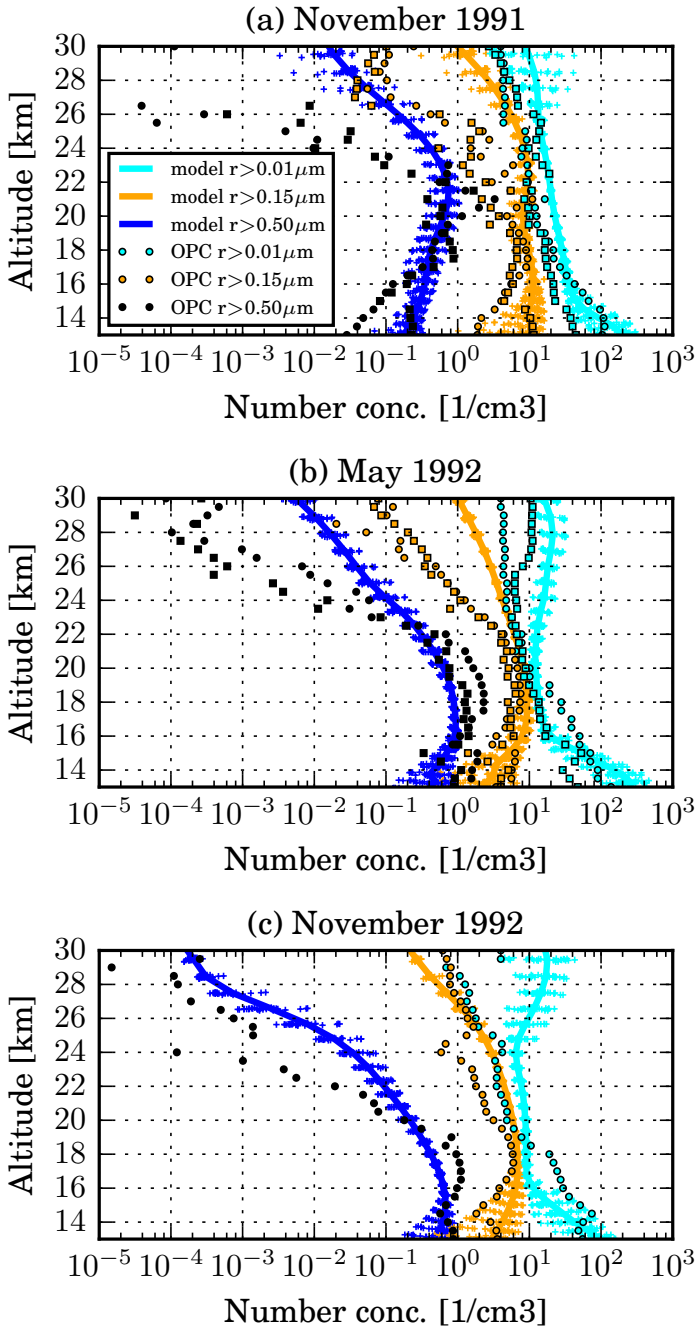

Figure 4.9: Vertical profile of the cumulative aerosol number concentration (cm^{-3}) for three channels ($r > 0.01$ µm in light blue, $r > 0.15$ µm in orange, and $r > 0.5$ µm in dark blue) in November 1991, May 1992 and November 1992 at Laramie, Wyoming (41° N, 105° W) in the style of Sekiya et al. [2016]. Solid lines show the modelled monthly mean, while the crosses indicate the range of daily mean concentrations within that month. Optical particle counter (OPC) measurements from Deshler et al. [2003] are shown as symbols.

4.3.2 Stratospheric temperature anomaly

We also compare simulated and observed lower stratospheric (LS) temperature anomalies following the Pinatubo eruption, although this is far from being straightforward. A few studies report LS temperature changes following Mt. Pinatubo's eruption as measured from satellite with a microwave sounding unit (MSU) instrument [Randel et al., 1995, Zhang et al., 2013]. As it relies on microwave, MSU has the advantage of not being influenced by the presence of aerosols, but it has the disadvantage of having a relatively broad weighting function on the vertical that encompasses both the upper troposphere (UT) and a large fraction of the stratosphere. Because stratospheric temperatures in climate models are generally biased one way or the other, it is not meaningful to compare absolute values of temperature. Rather we should compare temperature anomalies with and without the Pinatubo aerosols. There is a methodological issue here however. In the case of observations, one can only compare years 1991/1992 against a climatology from previous or following years. We could do the same in the model but lack a long enough simulation, so we compare two simulations with and without the Pinatubo aerosols and infer the temperature anomaly due to the aerosols.

Despite the intrinsic limitations of such a comparison, we compare here the model temperature anomaly (with and without Pinatubo aerosols) in nudged mode with the observed temperature anomaly (relative to baseline years) in Figure 4.10. This is not equivalent because the stratospheric heating may have changed (and probably has changed) the stratospheric circulation, and therefore the temperature anomalies, which is not the case in the model. Zhang et al. [2013] report a peak warming of about 2 K after Pinatubo in the global mean for MSU channel 4 that encompasses both the upper troposphere and lower stratosphere. This is a bit more warming than shown in an earlier study by Randel et al. [1995]. CMIP5 models show up to 3 K anomaly (see Figure 2 in Zhang et al. [2013]), while Revell et al. [2017] found up to 4 K when using the CCMI (Chemistry-Climate Model Initiative) aerosol data set as input for their chemistry-climate model (with the same radiative transfer scheme as LMDZ-S3A) and only 2 K when using the CMIP6 data set.

The temperature anomaly in the LMDZ-S3A simulation, convoluted with the MSU channel 4 weight function to make things comparable, is larger with a peak warming of 4.0 K, which may indicate an overestimated radiative heating in the model. One reason for the discrepancy in peak warming is likely due to the fact that O_3 is prescribed in the model to a constant climatology whereas, in the real world, O_3 has decreased by up to 15% after the Pinatubo eruption (according to Randel et al. [1995]). Since a large fraction of the SW heating rate induced by aerosols is actually related to an increase in gaseous absorption due to an increase in photon path upon aerosol scattering, the observed decrease in O_3 is expected to lead to a decrease in shortwave heating rates. We would need to couple an interactive O_3 scheme to our model to test this hypothesis. Finally it is also worth mentioning that the simulated temperature anomaly spreads

from the tropics to the high latitudes within about a month (at least in nudged mode), that is more rapidly than the sulphate aerosol itself and the corresponding AOD in the visible spectral range. This behaviour may be caused by the nudging scheme, or by a relatively strong diffusion of the temperature field in the model –which is required to stabilize the model dynamics– while the aerosol is transported through a less diffusive numerical scheme. The negative trend in the observed LS temperature anomaly in the years after the eruption is probably due to increasing concentrations of well-mixed greenhouse gases (GHG). The model does not show this behaviour because GHG concentrations do not vary in this experiment.

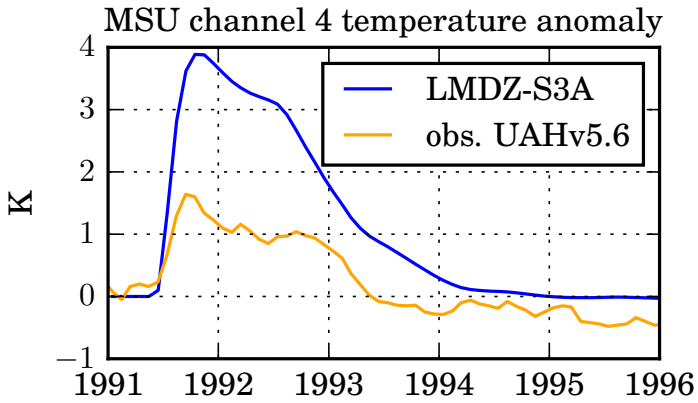

Figure 4.10: Global mean MSU channel 4 (upper tropospheric and lower stratospheric) temperature anomaly. The modelled anomaly due to the Pinatubo sulphate aerosol is computed as the difference between simulations with and without volcanic aerosol, while the observed anomaly reported by the UAH [Spencer and Christy, 1993] is with respect to the 1981–2010 base period.

4.4 Sensitivity studies under Pinatubo conditions

4.4.1 Sensitivity to van der Waals coagulation enhancement factor

In LMDZ-S3A we have only considered Brownian coagulation [Jacobson et al., 1994]. Other terms for coagulation include those due to van der Waals forces, sedimentation and turbulence. Among these additional terms, only that due to van der Waals forces has been considered by some authors [English et al., 2013, Sekiya et al., 2016]. Both studies rely on the calculations of Chan and Mozurkewich [2001], who measured coagulation for sulphuric acid particles of identical size end inferred an enhancement factor over Brownian coagulation for the limit cases of the diffusion (continuum) regime ($E(0)$) and the kinetic (free molecular) regime ($E(\infty)$). These enhancement factors are

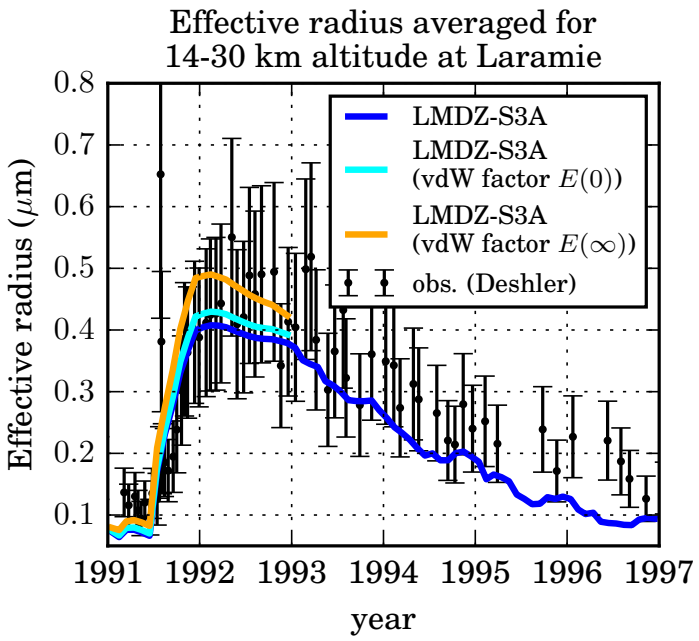

Figure 4.11: Stratospheric effective particle radius (in μm) at Laramie, Wyoming (41° N, 105° W) as simulated by the LMDZ-S3A model and observed with optical particle counters [Deshler et al., 2003]. The light blue (resp. orange) line shows the model result for coagulation enhanced by the continuum regime van der Waals enhancement factor $E(0)$ (resp. the kinetic regime enhancement factor $E(\infty)$).

not directly usable in our model because stratospheric conditions encompass both the continuum and the free molecular cases and the equations in Jacobson et al. [1994] cover the general case. But in order to determine the impact of neglecting van der Waals forces, we applied the parametrizations of the enhancement factor of Chan and Mozurkewich [2001] to the coagulation kernels of Jacobson et al. [1994] and performed two additional simulations of the Pinatubo eruption: a first one with coagulation enhanced uniformly by the factor $E(0)$ and a second one with coagulation enhanced uniformly by the factor $E(\infty)$ (which is generally larger than $E(0)$). The actual enhancement factor for stratospheric conditions can be expected to lie in between these two cases.

As in previous studies, the van der Waals coagulation term improves the comparison to observation for particle number concentration (not shown) and particle average size (shown in Figure 4.11), but it makes it a little worse for AOD as shown in Figure 4.12, with the global-mean stratospheric AOD peaking too low (and too early) compared to the Sato climatology. Given that there are only few measurements on the van der Waals coagulation term, and the mixed results obtained in our model, we do not include this process in our default model, but offer it as an option in the code of the model.

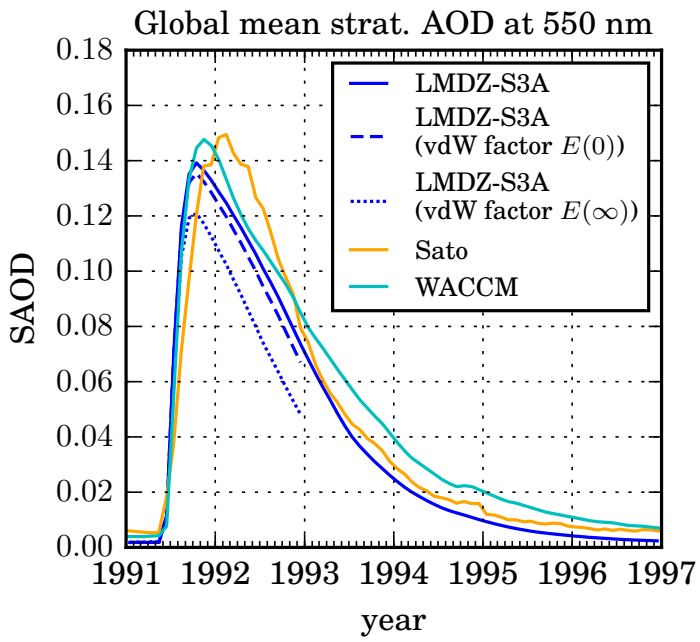

Figure 4.12: Evolution of the global mean stratospheric aerosol optical depth (SAOD) at 550 nm modelled with LMDZ-S3A compared to the climatology from Sato [2012] and to SAOD simulated with WACCM by Mills et al. [2016]. The dashed (resp. dotted) line shows the model result for coagulation enhanced by the continuum regime van der Waals enhancement factor $E(0)$ (resp. the kinetic regime enhancement factor $E(\infty)$).

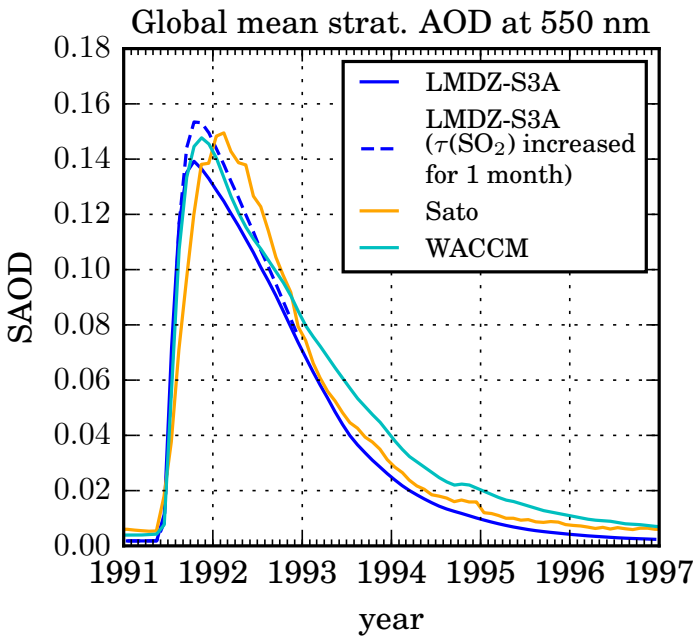

Figure 4.13: Same as Figure 4.12, but here the dashed line shows the model result for an SO_2 lifetime doubled on the day of the eruption, decreasing linearly to climatological values within one month.

4.4.2 Sensitivity to the sulphur dioxide chemical lifetime

A limitation of our model when simulating very large SO_2 injections might be the assumption of a constant SO_2 chemical lifetime (and hence a constant OH mixing ratio). Bekki [1995] showed that a constant SO_2 lifetime is not justified for an eruption as large as that of the Tambora. In order to test the sensitivity of our results to the assumed global SO_2 removal rate, we performed another Pinatubo simulation with SO_2 lifetimes increased by a factor 2 on the day of the eruption and decreasing linearly to normal values within one month. It appears unlikely that the OH effect impacted the global SO_2 lifetime beyond this factor 2, notably when compared with observational studies of the volcanic SO_2 decay. Analyses of SO_2 observations after the eruption give a global SO_2 lifetime ranging from 23 to 35 days [Bluth et al., 1992, Read et al., 1993]. We find that the increase in assumed SO_2 lifetime delays and slightly increases the peak of the global-mean AOD (shown in Figure 4.13). However, overall the sensitivity to the SO_2 lifetime appears to be small. Therefore, we conclude that using a prescribed chemical lifetime is probably not a major limitation of our model except for very large SO_2 injection rates, although it is desirable to improve the model in that respect in future studies.

4.5 Conclusions on the model evaluation

The model evaluation performed in this chapter shows that LMDZ-S3A reasonably reproduces aerosol observations in periods of low (background) and high (volcanic) stratospheric sulphate loading. But the model tends to overestimate the number of small particles and to underestimate the number of large particles, so that the modelled effective particle radius is slightly smaller than observed. This might be partly improved by considering currently neglected terms of coagulation. Other limitations of the model are that it uses prescribed chemical lifetimes of precursor gases and that it probably overestimates stratospheric heating by the aerosol, which might improve when including an ozone feedback.

Further evaluation of the model against other aerosol observations (e.g. from periods following smaller volcanic eruptions) would increase the robustness of its results. But in this context it has to be stated that it is a non-trivial task to gather observations of stratospheric aerosols for model evaluation. A fully validated, gridded stratospheric aerosol climatology (e.g. including aerosol extinction at wavelengths in the SW and LW, as well as information on aerosol concentration and size) in an easily usable format (like netCDF) with information on how gap filling is performed would tremendously facilitate the evaluation of model results. The stratospheric aerosol dataset produced for CMIP6 [Luo Beiping, personal communication, 2016] is a significant step in the right direction. Knowledge of (average) tropopause height would be particularly useful, so that vertically integrated quantities like AOD can be compared between model and observations and potential biases coming from differences in tropopause height can be detected. A more systematic reporting of observational uncertainties from both in situ and satellite data would also be helpful.

Despite this possible further model evaluation and improvement, LMDZ-S3A can already be seen as an appropriate tool for studying stratospheric sulphate aerosols with a focus on the evolution of particle size distribution and the resulting radiative effects. Therefore, we will use the model in the following chapter to study the efficacy and side effects of artificial stratospheric sulphur injections.

5 Studying stratospheric aerosol injection with LMDZ-S3A

In this chapter we will use the new LMDZ-S3A model, presented and evaluated in the previous chapters, to address the scientific questions regarding SAI that we formulated in Section 2.9. By performing model experiments with different scenarios of SAI using SO_2, we investigate how the radiative forcing of SAI depends on the injected amount of sulphur, the injection height, the number of injection points, and the temporal pattern of the injection. The content of this chapter is largely borrowed from the publication by Kleinschmitt et al. [2017b].

5.1 Simulation setup

We use the same configuration of LMDZ-S3A as for the simulations of the Pinatubo eruption shown in Section 4.3, although it has the limitation of a fixed chemical timescale for the SO_2 to H_2SO_4 conversion neglecting the possible depletion of oxidants. While this effect has been shown to be important for exceptional eruptions such as that of Tambora [Bekki, 1995], we found that this effect only limits oxidation for a short period after an eruption of the size of Pinatubo (see Section 4.3) with simulated maximum grid-box SO_2 mass mixing ratios of 71 ppm (in daily mean) and 2.6 ppm (in monthly mean). We therefore expect this effect to be smaller for our continuous SAI experiments where maximum SO_2 mixing ratios do not exceed 3.4 ppm in daily mean (and 2.2 ppm in monthly mean) for a continuous injection rate of $10\,\mathrm{Tg\,S\,yr^{-1}}$ and 16 ppm in daily mean (8.4 ppm in monthly mean) for $50\,\mathrm{Tg\,S\,yr^{-1}}$.

We define a STANDARD SAI scenario, upon which we then base sensitivity studies to estimate the role of certain parameters and features of the injection strategy. In this standard scenario, an amount of $10\,\mathrm{Tg\,S\,yr^{-1}}$ is injected in the form of SO_2 gas into one equatorial grid cell (at 1°N, 120°E). The equatorial injection takes advantage of the ascending branch of the Brewer-Dobson circulation (BDC) that contributes to lift the aerosol. The aerosol lifetime in the stratosphere in this configuration can be expected to be longer than for injection at higher latitudes, because of the poleward transport and subsequent removal through the BDC. Furthermore, the radiative forcing of the aerosol is generally larger (i.e., more negative) in the tropics because of the

Table 5.1: Description of the experiments performed in this study.

Experiment	Description
CONTROL	Control experiment with background stratospheric sulphate aerosols
STANDARD	Continuous equatorial injection of 10 $\mathrm{Tg\,S\,yr^{-1}}$ as SO_2 at 17±1 km into one equatorial grid cell
x_TGS	Same as STANDARD, but with different injection rates, where x = 2, 5, 20, 50 $\mathrm{Tg\,S\,yr^{-1}}$
z_KM	Same as STANDARD, but with different injection heights, where z = 15, 19, 21, 23 km
BROAD	Same as STANDARD, but injection distributed at 28 locations around the globe between 30°N and 30°S
SEASONAL	Same as STANDARD, but injections into one grid cell limited to two months of the year (at 5°N in April and at 5°S in October)
NORAD	Same as STANDARD, but with radiatively non-interactive aerosol and an injection height of 21 km

maximum in insolation there on an annual mean. The injection is constant in time, i.e. we add the same amount of SO_2 at every single time step of 30 min. Vertically the injection is distributed with a Gaussian profile in altitude centred at 17 km with a standard deviation of 1 km (similarly to our setup of the 1991 eruption of Mount Pinatubo discussed in Section 4.3).

In a first series of model experiments the magnitude of the stratospheric injection is varied between 2 and 50 $\mathrm{Tg\,S\,yr^{-1}}$, while all the other parameters are kept constant (experiments labelled x_TGS, see Table 5.1). In a second series the central injection height is varied between 15 and 21 km (still with a standard deviation of 1 km) for a default injection rate of 10 $\mathrm{Tg\,S\,yr^{-1}}$ (experiments labelled z_KM).

In addition to the sensitivity studies for injection magnitude and height, we performed experiments with different spatio-temporal injection patterns (BROAD and SEASONAL). In BROAD, the injection is spread equally in 28 locations with 7 latitudes (30°S, 20°S, 10°S, 1°N, 10°N, 20°N, 30°N) and 4 longitudes (120°W, 30°W, 60°E, 150°E). In SEASONAL, the injection is performed in the months of April and October only, switching from a location at 5°N to a location at 5°S, so as to always emit from the summer hemisphere. The STANDARD, BROAD and SEASONAL simulations therefore represent different injection strategies in terms of locations and logistics.

Each simulation is performed for 5 years and the results are shown for the 5$^{\mathrm{th}}$ year of the simulation, when the aerosol layer has clearly reached a steady state regarding burden, particle size and spatial distribution. The stratospheric model fields are generally averaged over all the grid cells above the tropopause (diagnosed at the grid cell and

timestep resolution).

We define the radiative forcing as the all-sky aerosol direct radiative effect (ADE) at the top of the atmosphere (TOA) in $\mathrm{W\,m^{-2}}$ for shortwave (SW), longwave (LW) and net (i.e. SW+LW) radiation. At each time step the radiative forcings are computed as the difference of two calls of the radiation code (one including sulphate aerosol, one not). Therefore the radiative forcing does not include any rapid adjustments that take place in the land-atmosphere system, including changes in stratospheric temperature and water vapour. The differences between this instantaneous radiative forcing (IRF) and the effective radiative forcing (ERF) that includes rapid adjustments are discussed in Section 5.9. It should also be noted that the change in stratospheric water vapour may also feed back onto stratospheric chemistry and SO_2 oxidation, which is not accounted for in our simulations.

In order to get a better understanding of the relation between forcing efficiency (in $\mathrm{W\,m^{-2}}$ / $\mathrm{Tg\,S\,yr^{-1}}$) and injection rate magnitude, we decompose it in the following way:

$$\begin{aligned} \text{forcing efficiency} &= \frac{\text{radiative forcing}}{\text{injection rate}} \\ &= \frac{\text{radiative forcing}}{\mathrm{AOD(550\,nm)}} \cdot \frac{\mathrm{AOD(550\,nm)}}{\text{burden}} \cdot \frac{\text{burden}}{\text{injection rate}} \end{aligned} \tag{5.1}$$

The first term (radiative forcing/AOD(550 nm) in $\mathrm{W\,m^{-2}}$ / unit AOD) reflects how a certain optical depth translates into a radiative forcing and is related to the model's radiative transfer code, to the distribution of the stratospheric aerosols in space and time, but also to particle size (since for a given AOD(550 nm), larger particles have a larger LW forcing than small particles). The second term (AOD(550 nm)/burden in unit AOD / Tg S) shows how effectively the particles extinguish visible light and is related to particle size (and hence to the model's aerosol microphysics). The third term (burden/injection rate in Tg S / $\mathrm{Tg\,S\,yr^{-1}}$ = yr) is equal to the effective lifetime of the injected sulphur in the stratosphere and therefore strongly depends on the modelled transport and removal processes. It should be noted that this decomposition is similar to the one used by Schulz et al. [2006] but is applied here to stratospheric aerosols.

5.2 Results from the reference experiment

The stratospheric burdens and the fluxes of the represented sulphur species for the STANDARD SAI simulation with an equatorial injection of $10\,\mathrm{Tg\,S\,yr^{-1}}$ at 17 km altitude are shown in Figure 5.1. The injected SO_2 is converted to H_2SO_4 after a mean lifetime of 41 days, while a fraction of roughly 4 % leaves the atmosphere without being converted (mostly because it is injected below the tropopause and rapidly removed

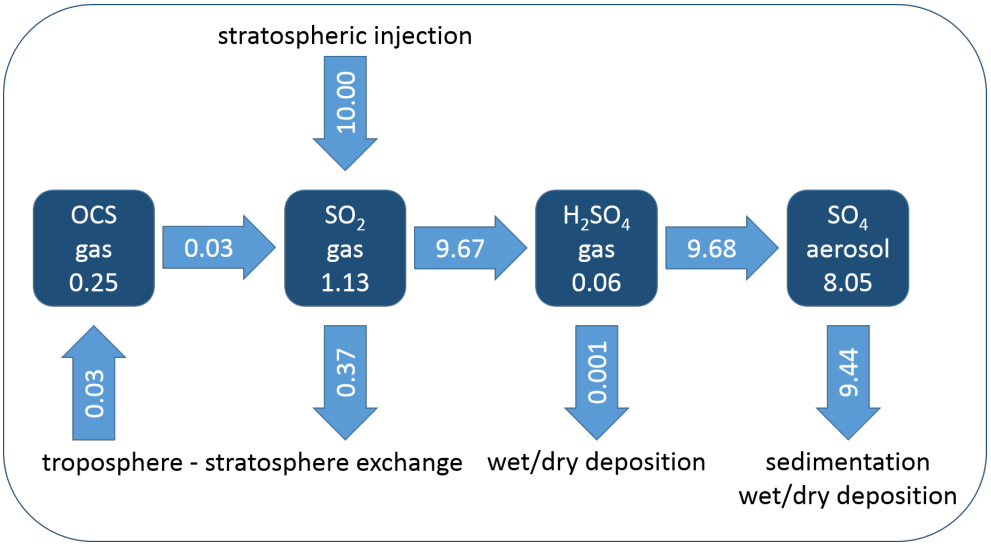

Figure 5.1: Annual mean stratospheric burdens (boxes, in Tg S) and fluxes (arrows, in Tg S yr^{-1}) of the represented sulphur species from the 5th year (quasi-steady state) of the STANDARD experiment. Minor discrepancies in the fluxes indicate that the steady state is not entirely reached after 5 years.

from the troposphere through wet scavenging). Conversion of OCS to SO_2 in the stratosphere (after a mean lifetime of 8 years) adds only 0.3 % to the injected sulphur mass. Therefore, the stratospheric sulphur budget can be considered as completely anthropogenic in this scenario. H_2SO_4 vapour has a lifetime of 2 days, with the nucleation and condensation processes converting H_2SO_4 vapour to the particulate phase. Thus 85 % of the stratospheric sulphur exists in the form of H_2SO_4 aerosols which has a mean lifetime in the stratosphere of about 10 months.

The spatial distribution of the sulphate aerosol mass mixing ratio in Figure 5.2 shows a pronounced maximum in the tropical stratosphere around 21±4 km altitude, i.e. well above the injection zone at 17±1 km. Outside the tropics the sulphate mixing ratio is much lower, characteristic of a relatively strong tropical transport barrier, and decreases further towards the poles. The spatial distribution of the injected SO_2 (not shown) is much more confined to the latitudinal band corresponding to the injection zone although it expands vertically a few km above the injection altitude. This is because the injected SO_2 is almost completely converted to sulphuric acid gas before significant latitudinal transport to higher latitudes can take place. The mixing ratio of sulphuric acid vapour (not shown either) is very low in the lower stratosphere due to its rapid consumption through particle formation and growth, but it increases above 30 km, where the aerosol evaporates.

The absorption of SW and LW radiation by the aerosol can heat up the surrounding air considerably. The temperature anomaly in the STANDARD SAI scenario with respect to the CONTROL run is shown in Figure 5.3. It reaches up to 16 K in the

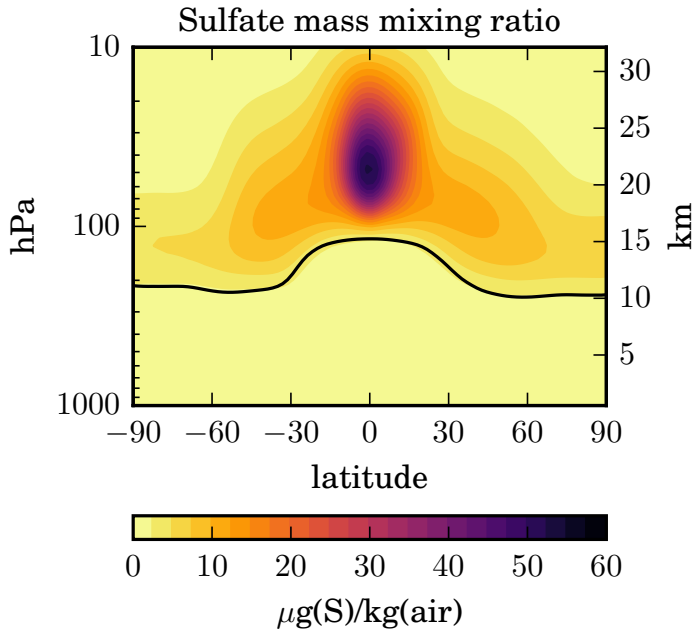

Figure 5.2: Latitude-height cross-section of the zonal and annual mean sulphate aerosol mass mixing ratio (in $\mu g\,S\,kg\,air^{-1}$) for the STANDARD experiment.

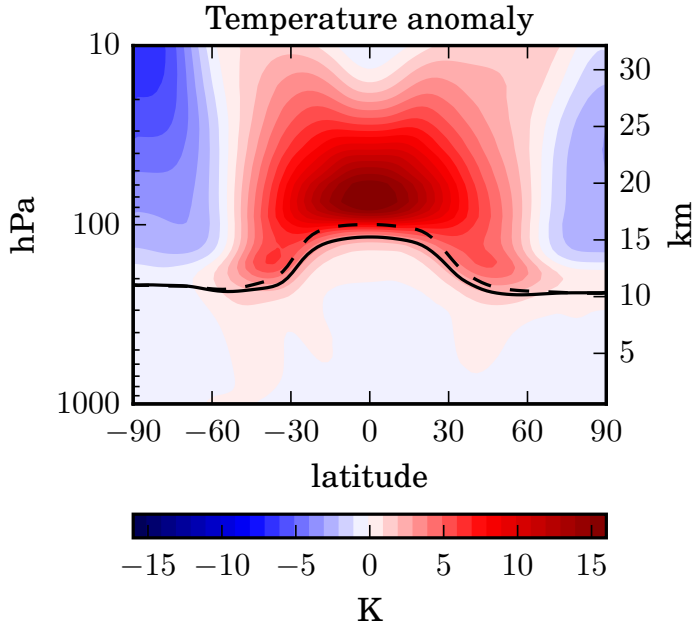

Figure 5.3: Latitude-height cross-section of the zonal and annual mean temperature anomaly (in K) in the STANDARD experiment relative to the CONTROL experiment.

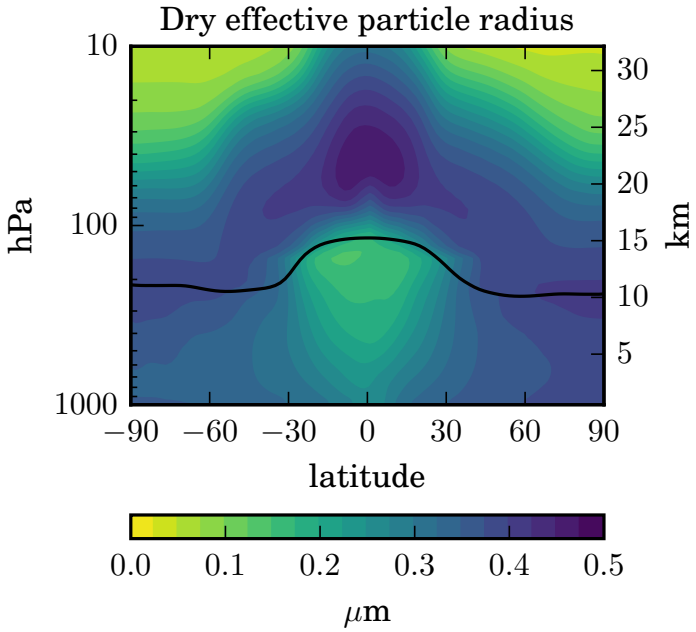

Figure 5.4: Latitude-height cross-section of the zonal and annual mean effective radius (in μm) of dry sulphate particles in the STANDARD experiment. The effective radius is computed from the zonal and annual means of the aerosol volume and surface area.

lower tropical stratosphere and decreases with increasing altitude and latitude. In the upper troposphere the heating is weaker due to the low particle concentrations, but it can reach up to 3 K just below the tropopause. This heating is significant and contributes to the lifting of the injected SO_2 and the aerosol. As discussed in Section 4.3, the LMDZ-S3A model may overestimate the temperature anomaly considerably. One possible reason for the discrepancy is that we prescribe O_3 to its climatological values whereas O_3 mixing ratios are known to have decreased after Pinatubo, thus decreasing absorption of SW radiation. Therefore, the effects of SAI presented in this study that critically depend on the radiative heating may not be as important in reality and should be studied with other models as well.

The tropopause itself, which is diagnosed within the model following the WMO definition based on the lapse-rate, descends by about 1 km in the tropics due to the heating of the lower stratosphere and the upper troposphere. Santer et al. [2003] studied the contribution of various forcings to observed tropopause height changes. They showed that after the Mount Pinatubo eruption a tropopause descent of 5–10 hPa (roughly 0.2–0.4 km) was observed. This was probably caused by a heating of the stratosphere and a parallel cooling of the troposphere by the volcanic sulphate aerosol. But the underlying trend over the last decades is an increase in tropopause height caused by well-mixed greenhouse gases, which heat the troposphere and cool the stratosphere. Hence, this observed increase due to global warming might be compensated (or even overcompensated) by the effect of SAI. But it should also be noted that our simulations are based on fixed SST, while an interactive ocean might have an impact on temperature changes and therefore on the tropopause height.

The spatial distribution of particle size (i.e., effective radius r_{eff}) is shown in Figure 5.4. With effective radii up to 0.5 μm the particles are largest above the injection region where the sulphate concentrations are the largest. The region with the largest particles descends towards higher latitudes due to ongoing particle growth and sedimentation during the meridional transport through the BDC.

5.3 Sensitivity to the injected sulphur dioxide mass

The relation between the magnitude (i.e. the injected mass) of the stratospheric sulphur injections and the resulting net radiative forcing is shown in Figure 5.5. The most surprising observation is that the forcing does not exceed the –1.9 W m^{-2}, which is reached in the 20_TGS experiment, but decreases (in absolute value) for an even larger injection rate of 50 Tg S yr^{-1}. This is because the SW forcing does not increase as strongly with injection magnitude as the LW forcing (with opposite sign), due to the increase in particle size.

In order to illustrate the non-linear impact of the injection magnitude on the spatial distribution of the stratospheric aerosol, we plotted the sulphate aerosol mass mixing

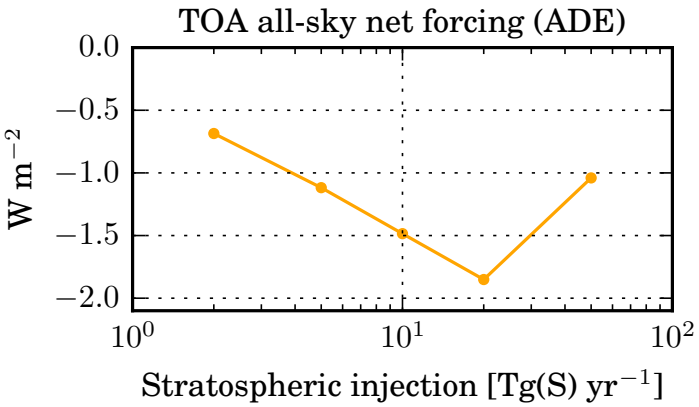

Figure 5.5: Global mean instantaneous net radiative forcing (aerosol direct effect = ADE) at the top of the atmosphere (TOA) in W m^{-2} for the *x*_TGS experiments with different injection rates.

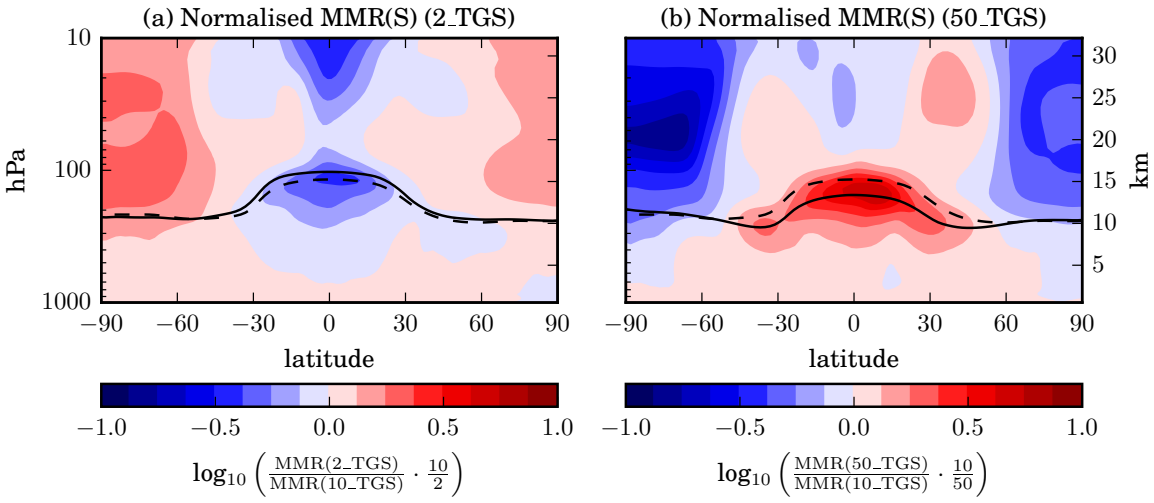

Figure 5.6: Latitude-height cross-sections of the zonal and annual mean sulphate aerosol mass mixing ratio (a) for the 2_TGS and (b) for the 50_TGS experiment, normalised by the value in the STANDARD (= 10_TGS) experiment and the ratio of the injection rates. The base-10 logarithm of the ratio is plotted as indicated below the color scale, so that positive (negative) values indicate larger (smaller) values than implied by a linear scaling. The mean tropopause level in the experiment is indicated by a solid line and the tropopause in the STANDARD simulation by a dashed line.

ratio (MMR) normalised by the value in the STANDARD experiment and the ratio of the injection rates in Figure 5.6. For a linear scaling of MMR with injection rate, this ratio would be unity everywhere (so the base-10 logarithm of the ratio –which is the quantity plotted– would be zero). In our model simulations, for a small injection of $2\,\mathrm{Tg\,S\,yr^{-1}}$, the ratio is well below 1 above and below the injection region, while it is above 1 in the polar stratosphere. For a large injection of $50\,\mathrm{Tg\,S\,yr^{-1}}$, the ratio shows the opposite pattern (apart from the zone immediately above the injection region). From this we can conclude that in relative terms with increasing magnitude of the injection rate 1) more sulphur accumulates below the injection region because of increasing sedimentation of larger particles and 2) less sulphur reaches the high latitudes because of the induced changes in stratospheric dynamics (discussed in Sect. 5.8) and/or because of faster sedimentation during the meridional transport. The sulphate MMR above the injection region is largest (in relative terms) in the 10 and $20\,\mathrm{Tg\,S\,yr^{-1}}$ scenario, probably because in these cases the updraft by aerosol heating is strong enough to lift the particles while the sedimentation is still relatively slow.

The mean forcing efficiency and its decomposition described above for the simulations with varying injection magnitude are shown in Figure 5.7. The forcing efficiency in the SW decreases by roughly 50 % between 2 and $50\,\mathrm{Tg\,S\,yr^{-1}}$, while in the LW it stays rather constant. As a result, the net forcing efficiency decreases dramatically for larger injection rates (by 94 % between 2 and $50\,\mathrm{Tg\,S\,yr^{-1}}$). Even the absolute forcing decreases from 20 to $50\,\mathrm{Tg\,S\,yr^{-1}}$ (see Figure 5.5). The decomposition shows that this decrease is mainly due to a decreasing net forcing/AOD (by 87 % between 2 and $50\,\mathrm{Tg\,S\,yr^{-1}}$ injection rates), which itself is caused by an increasing LW forcing/AOD combined with a rather constant SW forcing/AOD. The AOD/burden also decreases by more than 50 % due to larger particles (see Figure 5.8). Despite this finding, the lifetime of the particles does not clearly decrease for larger injection magnitude. This may be explained by the superposition of two opposed effects: increasing sedimentation velocity and increasing updraft through heating of the air. Both can be seen in Figure 5.6a, where the sulphate mixing ratio increases disproportionately with the injection rate above the injection region (due to updraft) and below it (due to sedimentation). But for the largest injection rate simulated, enhanced sedimentation starts to dominate (see Figure 5.6b) so that the particle lifetime can be expected to decrease further for even larger injections.

Figure 5.8 shows the impact of the injection magnitude on particle size. The global mean effective radius (computed for all the aerosol above the tropopause) almost triples between 2 and $50\,\mathrm{Tg\,S\,yr^{-1}}$. The mass size distribution shown in Figure 5.9 mainly differs in the size range above 0.1 μm such that the mode radius grows and is shifted towards larger radius with increasing injection rate. This explains the increase in LW forcing and therefore the decreasing forcing efficiency.

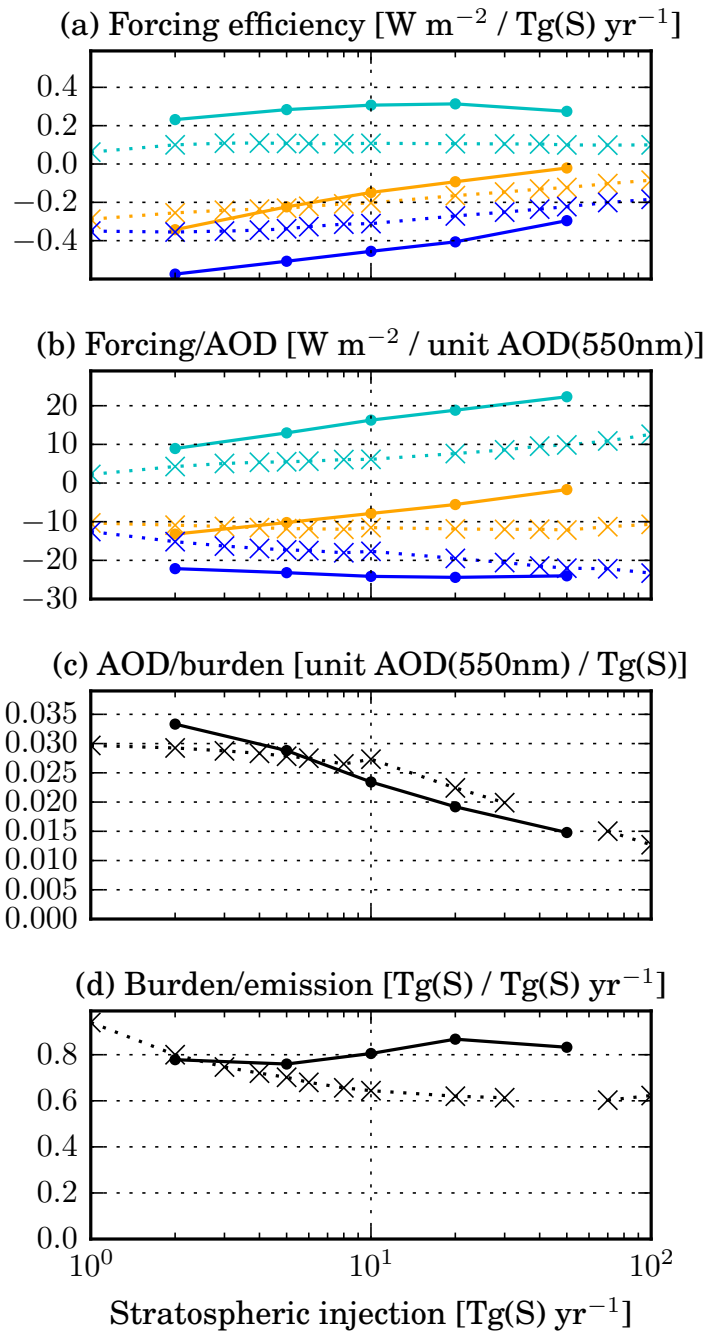

Figure 5.7: (a) Forcing efficiency (i.e., ratio of global mean instantaneous radiative forcing by the global sulphur injection rate) for the *x*_TGS simulations with different injection rates. The SW component is shown in dark blue, the LW component in light blue and the net flux in orange. Panels (b) to (d) show the decomposition of the forcing efficiency as described in the text (see Eq. 5.1). The solid lines show the results from the described LMDZ-S3A simulations, while the crosses show results from a previous study by Niemeier and Timmreck [2015].

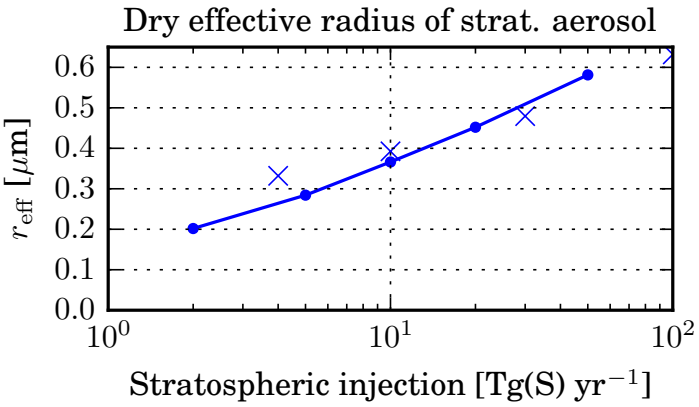

Figure 5.8: Global mean dry effective radius (in µm) of the stratospheric sulphate aerosol as a function of sulphur injection rate (Tg S yr^{-1}). The solid lines show the results from the *x*_TGS experiments using LMDZ-S3A, while the crosses show results from a previous study by Niemeier and Timmreck [2015].

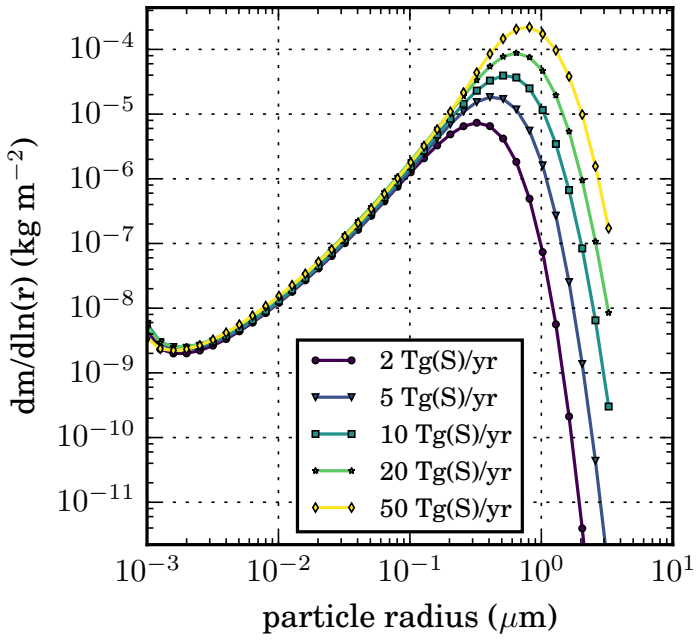

Figure 5.9: Column-integrated global and annual mean stratospheric aerosol mass size distribution ($\mathrm{d}m/\mathrm{d}\ln r$, in kg($H_2SO_4$) m^{-2}) for the *x*_TGS experiments with varying sulphur injection rate.

5.4 Comparison with results from Niemeier and Timmreck [2015]

Niemeier and Timmreck [2015] performed a similar sensitivity study for the SAI injection rate with the ECHAM model using a modal aerosol module. Their results deviate from ours in that the absolute net forcing increases monotonically with injection rate up to $100\,\mathrm{Tg\,S\,yr^{-1}}$, while the forcing efficiency decreases only moderately (see crosses in Figure 5.7).

One important difference in the results of the two models is the evolution of particle size with increasing injection rate. Figure 5.8 shows that in LMDZ-S3A the particles are smaller than in ECHAM for small injections and larger for large injections. Therefore the SW forcing efficiency decreases more in LMDZ-S3A, resulting in a lower net forcing efficiency. This difference in particle growth may partly be caused by differences in aerosol microphysics (modal versus bin scheme) and/or differences in meridional transport between the two models. The transport barrier is quite weak in the ECHAM version with 39 vertical levels (without a generated QBO) used by Niemeier and Timmreck [2015] and transport is hardly affected by the aerosol, while in LMDZ-S3A the barrier is strengthened for larger injection rates because of the impact of the radiative heating on the stratospheric dynamics. Therefore, the aerosol plume is even more confined for larger injections in LMDZ-S3A, leading to enhanced particle growth. In a recent study, Niemeier and Schmidt [2017] used a version of ECHAM with higher vertical resolution (L90) and more realistic stratospheric dynamics and also found that heating by aerosols slows down the meridional transport, making larger injections even less efficient.

We also found that the maximum extinction coefficient (in $\mathrm{km^{-1}}$) in both the SW and the LW bands is about a factor of 2 larger in LMDZ-S3A for a given injection rate. This causes a stratospheric heating which is also about twice as strong as in ECHAM. The stronger heating may explain why aerosol lofting plays a more important role in LMDZ-S3A, such that increasing sedimentation can be partly compensated (resulting in a longer aerosol lifetime). The difference in extinction between the models might be due to different particle size distributions, different computations of the aerosol optical properties or due to differences in the radiative transfer scheme.

Another difference may also partly explain the differing model results: In ECHAM, the global mean SW forcing/AOD increases for larger injections, keeping the net forcing/AOD rather constant. In contrast, in LMDZ-S3A the SW forcing/AOD is rather independent of the injection rate, which in combination with increasing LW forcing/AOD causes the net forcing/AOD to decrease drastically. It remains unclear why the SW forcing/AOD increases with injection rate in ECHAM.

5.5 Sensitivity to injection height

Earlier model studies found a strong dependence of the forcing efficiency on the injection height, therefore we conducted a series of simulations with different injection heights.

Figure 5.10 shows that both the SW and the LW forcings increase with increasing injection height, but the net forcing (sum of SW and LW components) is almost completely independent of the injection height. Considering again the decomposition of the forcing efficiency given in Eq. 5.1, it appears that the net forcing/AOD decreases for higher injections, implying a less optimal size and spatial distribution of the aerosol. The AOD/burden ratio decreases as well due to larger particles (see Figure 5.11), while the lifetime increases, as one would expect. There are various reasons for a shorter aerosol lifetime in the stratosphere for lower injection height. On the one hand, a larger fraction of the sulphur is injected below the tropopause, so most of it does not enter the stratosphere at all and is rapidly removed from the troposphere. In the 15_KM experiment 72 % of the sulphur are injected below the tropopause, while in the 17_KM (STANDARD) experiment it is only 4 %. On the other hand, the tropical meridional transport barrier is less pronounced in the lower stratosphere than above 20 km. Therefore, the sulphur is transported more effectively to higher latitudes, where it leaves the stratosphere again.

The lifetime increases for higher injections, but the mean effective particle radius increases as well. Particles might grow larger because the aerosol does not spread as rapidly as in the lower stratosphere and the larger local concentrations favour coagulation and condensation. Additionally, in the case of higher injections the mean stratospheric size distribution contains more particles which had more time to grow due to their longer lifetime.

The effects of longer lifetime and less optimal optical properties (larger particles) just cancel out each other, such that the overall radiative forcing does not increase with injection height. As higher injections can be expected to be technically challenging, the effort to produce a certain forcing even increases. Therefore our modelling results imply that it would not be worthwhile to inject the aerosol at altitudes higher than 19 km. However the simulations show that injections at less than 17 km altitude would probably be very inefficient, because they result in a small stratospheric aerosol burden.

The particle size, i.e. the effective radius, shown in Figure 5.11 appears to approach a saturation level of slightly below 0.5 μm with increasing injection height. Only the aerosol mass on the lower end of the size range decreases further (see Figure 5.12), probably because of faster coagulation. The particle concentration in all the size bins decreases when going from the tropics to mid and high latitudes, except for the 15_KM experiment, where the concentration of particles around 0.1 μm slightly increases

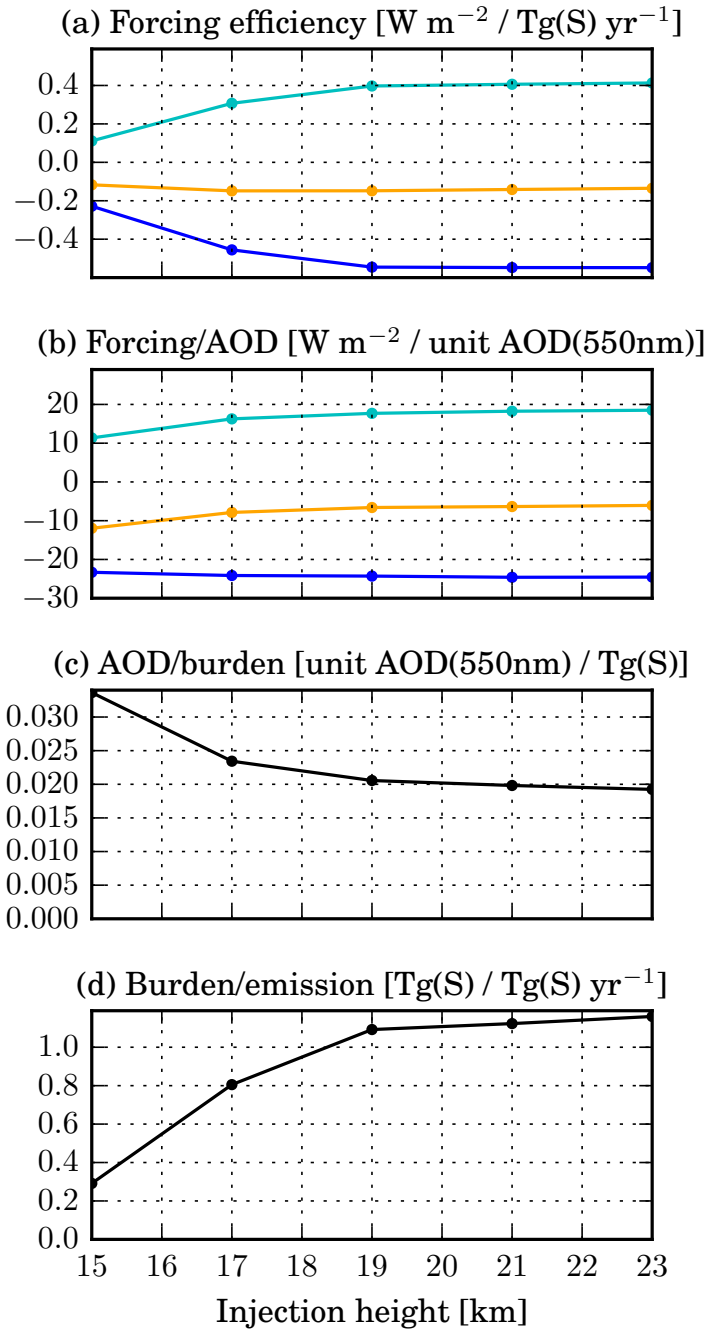

Figure 5.10: Forcing efficiency and its decomposition (as in Figure 5.7) for the *z*_KM simulations with different injection heights.

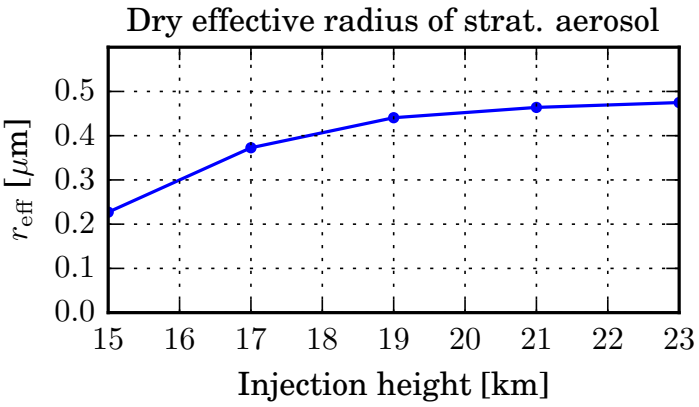

Figure 5.11: Global mean effective radius (µm) of the dry stratospheric sulphate aerosol as a function of injection height (in km) of the z_KM experiments.

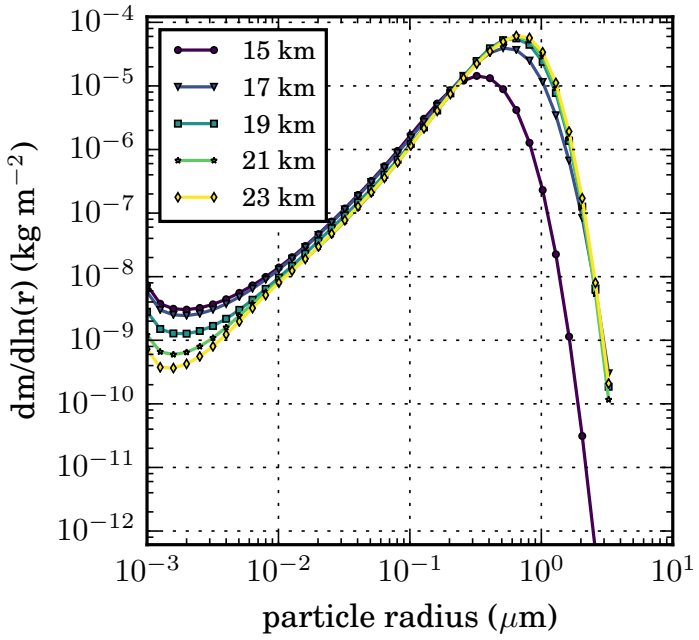

Figure 5.12: Column-integrated global and annual mean stratospheric aerosol mass size distribution ($\mathrm{d}m/\mathrm{d}\ln r$, in kg m^{-2}) for the z_KM experiments with varying injection height.

towards mid latitudes. This may be due to relatively fast meridional transport of the aerosol through the lower branch of the BDC in this case.

5.6 Sensitivity to spatio-temporal injection pattern

Previous model studies [e.g., Niemeier and Timmreck, 2015] indicate that the choice, when and where to inject a given mass of SO_2, can affect the forcing efficiency considerably. Therefore we simulated two additional scenarios with an injection rate of $10\,\mathrm{Tg\,S\,yr^{-1}}$, but with injection patterns differing in time and space, called BROAD and SEASONAL (see Table 5.1). The resulting global mean values of relevant quantities are shown in Table 5.2.

Table 5.2: Global mean quantities for experiments with $10\,\mathrm{Tg\,S\,yr^{-1}}$ injection rate but different spatio-temporal injection patterns.

Experiment	forcing ($\mathrm{W\,m^{-2}}$)			AOD at 550 nm	r_{eff} (µm)	burden (Tg S)
	SW	LW	net			
STANDARD	–4.6	+3.1	–1.5	0.19	0.37	8.1
BROAD	–3.7	+2.2	–1.5	0.16	0.30	5.7
SEASONAL	–4.8	+3.1	–1.6	0.20	0.38	8.4

In the BROAD scenario, in which the sulphur mass is distributed over 28 points covering a larger area in the tropics, the effective particle radius r_{eff} is almost 20 % below the one in the STANDARD scenario with injection into one equatorial grid box. However, the net forcing is almost equal in the two experiments, because the more favourable optical properties in the BROAD simulation are compensated by a smaller stratospheric aerosol burden. One reason for the smaller burden (and shorter lifetime) is the shorter average travel time from the injection region (30°N to 30°S) to mid/high latitudes where the aerosol is removed from the stratosphere. Another cause is that most of the aerosol remains below 20 km altitude, because it is not lifted by the BDC at the Equator and the more distributed injection pattern produces smaller radiative heating rates and therefore less updraft than in the STANDARD scenario. The AOD at 550 nm is much smaller in the tropics, but larger at mid latitudes.

In the SEASONAL scenario, where the sulphur mass is wholly injected during only two months of the year, the particles are slightly larger than in the STANDARD scenario. But because the burden is also a bit larger, the resulting net forcing is about 10 % larger than in the STANDARD scenario. The larger burden may result from a stronger updraft (due to larger aerosol concentrations in the short injection periods) that transports the aerosol to higher altitudes. This small increase in forcing efficiency seems to contradict a recent study by Laakso et al. [2017] who did not find a larger SW radiative forcing for seasonally varying injection scenarios. But it may be that the small increase

that we find is only caused by the stronger updraft / longer lifetime and not by the seasonal variations. And we have to keep in mind that the LMDZ-S3A model probably overestimates the radiative heating and therefore the aerosol lifting.

5.7 Effect of radiatively interactive aerosol

We will now discuss the impact of having radiatively interactive aerosols in our model simulations. Indeed the heating of the stratosphere and the upper troposphere described above can be expected to have a considerable impact on the atmospheric dynamics and thereby on the distribution and evolution of the aerosol distribution itself. In order to quantify this impact, we performed an SAI simulation called NORAD in which the aerosol does not interact with radiation (only the instantaneous radiative forcing is computed from a double radiation call, but the model integration is performed with stratospheric aerosols that are invisible to the radiation). In this scenario, we chose a relatively high injection height of 21 km, because without any aerosol-induced heating an important factor for the vertical transport from the tropical tropopause layer (TTL) to the stratosphere is missing.

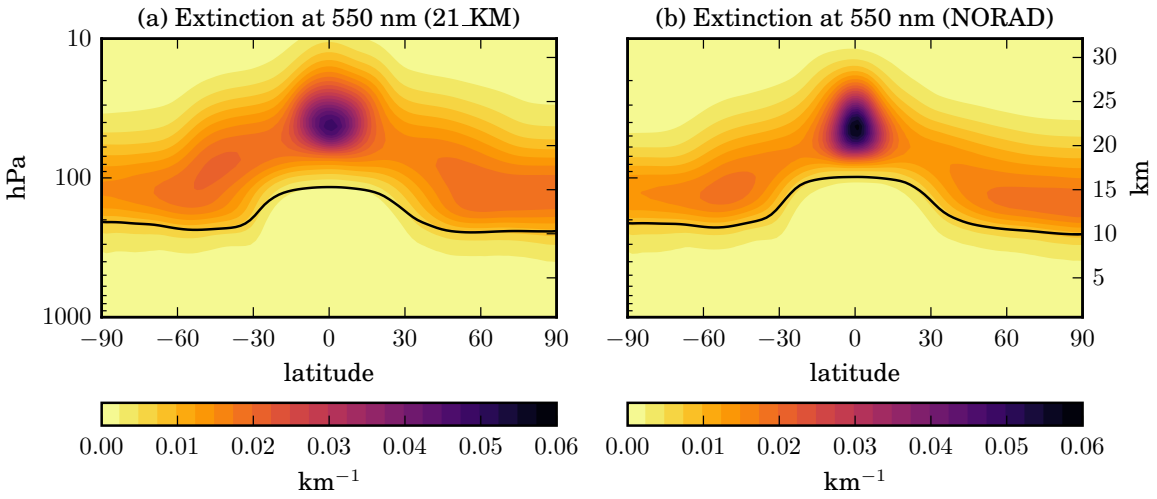

Figure 5.13: Latitude-height cross-section of the zonal and annual mean distribution of the aerosol extinction coefficient (km^{-1}) at 550 nm for equatorial stratospheric aerosol injections at 21 km from (a) a simulation with radiatively interactive aerosol (21_KM) and (b) a simulation with non-radiatively interactive aerosol (NORAD).

The resulting vertical distributions of the aerosol extinction coefficient with and without radiative interaction are shown in Figure 5.13. The heating causes the aerosol to

rise higher and spread more meridionally. This may also be related to the changes in stratospheric dynamics described below. The spatial distribution in the NORAD (at 21 km) experiment is closer to the one in the 17_KM or 19_KM experiments, but with a more pronounced maximum in extinction coefficient. Due to the more confined spatial distribution in the NORAD simulation, local concentrations of sulphuric acid and particles are larger, causing the particles to grow larger through condensation and coagulation. Many of the larger particles leave the stratosphere through sedimentation already in the tropics, so that the stratospheric aerosol burden in the NORAD experiment is smaller than in the 21_KM, 19_KM and even 17_KM experiments. Therefore, the resulting global mean net radiative forcing is significantly smaller in the NORAD experiment (–0.9 $\mathrm{W\,m^{-2}}$) than in the 21_KM simulation with radiatively interactive aerosols (–1.4 $\mathrm{W\,m^{-2}}$).

5.8 Impact on the quasi-biennial oscillation

The locally very strong heating of the lower stratosphere and upper troposphere due to the aerosol-radiation interactions (up to 16 K for the standard SAI scenario relative to the control run) can be expected to have a considerable impact on atmospheric dynamics. The quasi-biennial oscillation (QBO) in the equatorial stratosphere is an important dynamical feature of the stratosphere. It consists of easterly and westerly winds alternating with a period of approximately 28 months. The phase of the QBO is known to affect the poleward transport of trace gases and aerosols in the stratosphere [Trepte and Hitchman, 1992].

Indeed Figure 5.14 shows that the QBO is strongly affected by the sulphur aerosol injection, in agreement with a previous study by Aquila et al. [2014]. While the QBO period in the spin up and CONTROL simulations including only stratospheric background aerosol is approximately 28 months (varying between 24 and 32 months as the background aerosol layer builds up), it increases significantly already for the smallest simulated injection rate of 2 $\mathrm{Tg\,S\,yr^{-1}}$. In the 5 $\mathrm{Tg\,S\,yr^{-1}}$ scenario the periodicity disappears, while easterly winds dominate below 25 km and westerly winds dominate above. For the scenarios with 10 $\mathrm{Tg\,S\,yr^{-1}}$ and more, the direction of the propagation inverts from downward to upward, but with a period of approximately one year and with smaller amplitude.

This strong perturbation of the stratospheric dynamics results in a stronger barrier for meridional transport from the tropics to higher latitudes, as can be seen in Figure 5.6b where the sulphate aerosol mass mixing ratio at higher latitudes decreases (in relative terms) for larger injections. The higher aerosol concentrations in the tropics caused by the transport barrier favour particle growth and therefore make larger injections even less efficient. Furthermore, a breakdown of the QBO may also perturb the tropospheric circulation, thereby causing additional unintended side effects on climate.

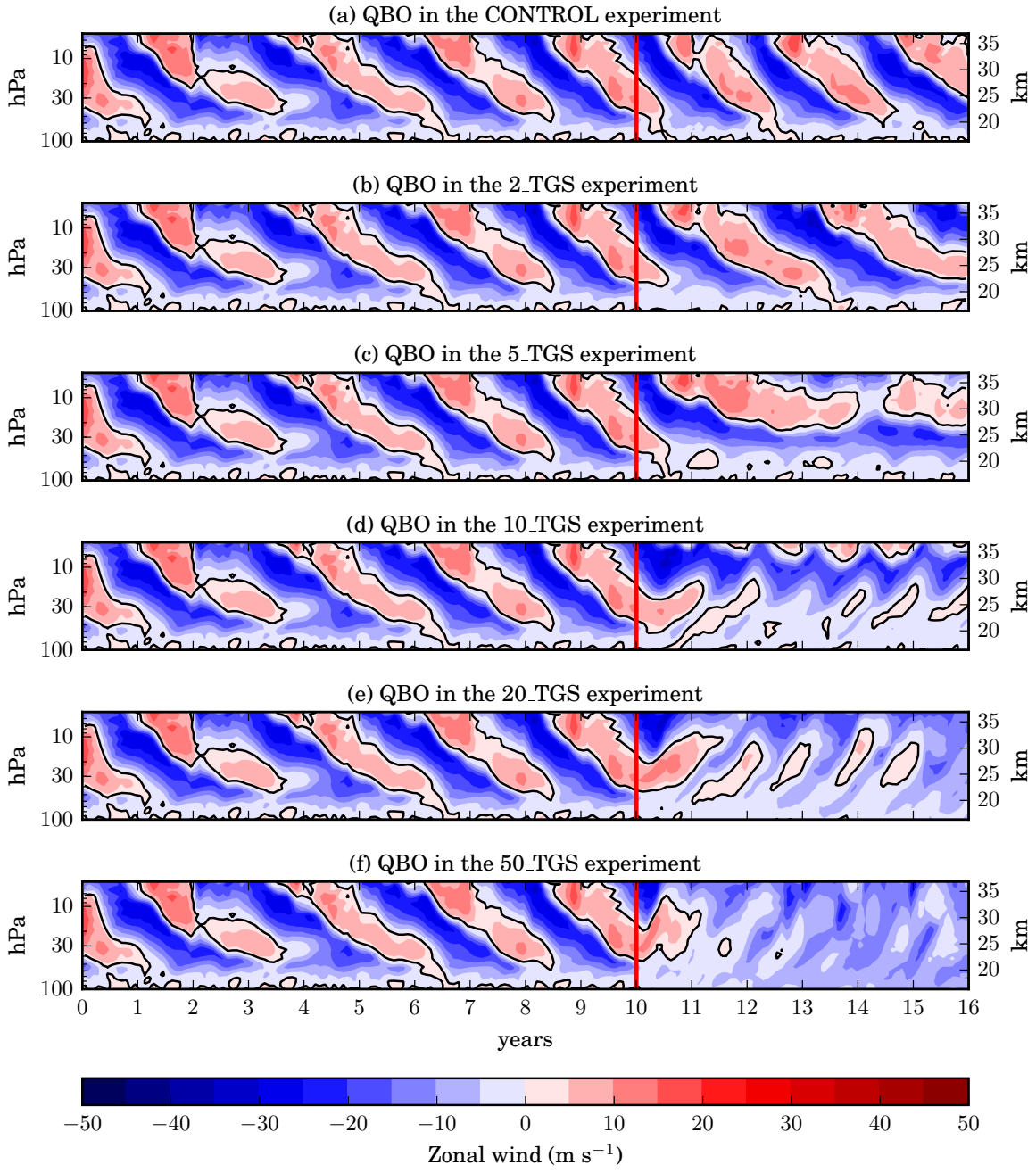

Figure 5.14: Temporal evolution of the vertical profiles of zonal wind (in m s^{-1}), averaged zonally and between 2° N and 2° S. The QBO can be seen in the alternating downward propagation of easterly (blue) and westerly (red) wind direction. All the simulations share the same background aerosol spin up period of 10 years. The onset of the continuous sulphur injections is marked by a red line.

5.9 Rapid adjustments and effective radiative forcing

For a given radiative forcing mechanism, e.g. that due to sulphate aerosols, one can distinguish between an instantaneous radiative forcing (IRF) and the effective radiative forcing (ERF) that results from the IRF and from the so-called *rapid adjustments* of the climate system to the IRF on the time scale of days or weeks [Sherwood et al., 2015] (see Figure 5.15). Slower climate feedbacks, mostly driven by surface temperature changes, are not included in the ERF. In climate model experiments, IRF is normally computed at each time step as the difference in radiative fluxes between a call of the radiation code with the aerosol (or another forcing agent) and one call without it, with everything else (temperature, humidity and cloud profiles, surface properties, ...) kept constant. In contrast, ERF is computed as the difference between a simulation with the aerosol and a control simulation without it, for which identical sea surface temperatures (SSTs) and sea ice cover are prescribed. The rapid adjustments responsible for the difference between IRF and ERF are changes in atmospheric temperature, humidity, cloudiness, and (to a smaller extent) land surface. These rapid adjustments tend to depend on the radiative forcing mechanisms, whereas the climate feedbacks driven by changes in surface temperature are more common to different forcing mechanisms. Sherwood et al. [2015] showed that ERF predicts the global mean surface temperature change better than IRF. Therefore, we will analyse ERF of SAI and the related rapid adjustments in this section, which is based on parts of the publication by Boucher, Kleinschmitt, and Myhre [2017].

In Section 5.2 we have already shown the strong impact of SAI on the stratospheric and upper tropospheric temperature (see Figure 5.3). This is probably the most important rapid adjustment of the climate system to SAI and it has several consequences. The temperature increase at the tropical tropopause cold point allows more water vapour to enter the stratosphere. Figure 5.16 (left panel) shows that the stratospheric water vapour mixing ratio (i.e. humidity) increases by up to 3 ppm in the STANDARD SAI experiment. As water vapour is a GHG, this results in a positive contribution to the ERF. Interestingly, the current global warming due to GHGs is also causing an increase in stratospheric humidity in the order of 1 ppm [Gettelman et al., 2010, Dessler et al., 2013, 2016] and the oxidation of methane (to CO_2 and H_2O) might lead to a further increase by roughly 1 ppm over the 21st century [Revell et al., 2016]. So the simulated increase due to SAI might be larger than the contribution of GHGs, but the two effects would probably not add up, as SAI would suppress the tropospheric warming responsible for a part of the current stratospheric humidity increase.

Another impact of the stratospheric and upper tropospheric heating due to SAI is a decrease in cirrus clouds in the tropics and mid-latitudes (see right panel of Figure 5.16), which agrees with a previous study by Kuebbeler et al. [2012]. This decrease is most probably caused by a stabilisation of the UTLS due to the reduced vertical temperature gradient, i.e. less convection and therefore a reduced formation of cirrus clouds. As

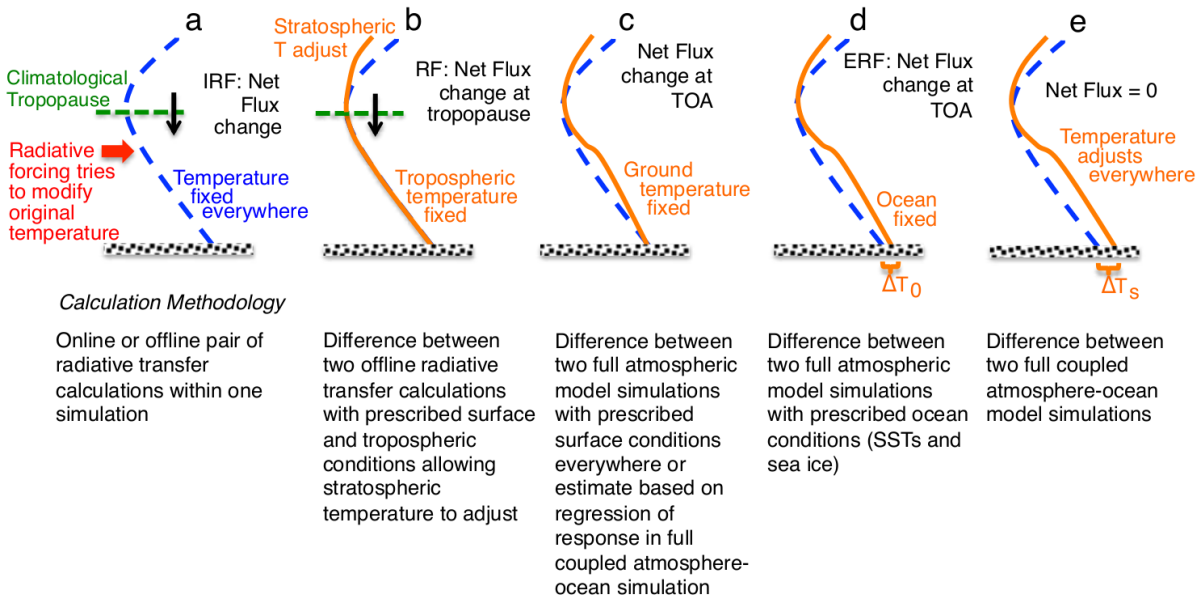

Figure 5.15: Schematic illustrating the difference between instantaneous (IRF), effective (ERF), and other types of radiative forcing (RF). Graphic extracted from Myhre et al. [2013] with the following caption: "Cartoon comparing (a) instantaneous RF, (b) RF, which allows stratospheric temperature to adjust, (c) flux change when the surface temperature is fixed over the whole Earth (a method of calculating ERF), (d) the ERF calculated allowing atmospheric and land temperature to adjust while ocean conditions are fixed and (e) the equilibrium response to the climate forcing agent. The methodology for calculation of each type of forcing is also outlined. ΔT_0 represents the land temperature response, while ΔT_S is the full surface temperature response."

microphysical effects of sulphate particles on cloud formation are not included in our model, they cannot be responsible for the observed change. Anyway, Cirisan et al. [2013] showed that these effects would probably be small, so neglecting them in our model should not be a limitation.

Besides the decrease in cirrus clouds, an increase in polar stratospheric clouds can be observed in Figure 5.16 (right panel). It is largest in the winter and spring season and more pronounced on the Southern Hemisphere. Such stratospheric ice clouds have been observed in the real world, e.g. with satellite instruments [Dessler, 2009]. In the model they form from the additional stratospheric water vapour at relatively low temperatures. The condensation of water vapour in these clouds may also explain why the humidity increase due to SAI is relatively low in the polar stratosphere.

The rapid adjustments of the climate system to the IRF of SAI described above lead to an ERF that is considerably different from the aerosol IRF. Boucher, Kleinschmitt, and Myhre [2017] used radiative kernel calculations [Myhre et al., 2011] to decompose

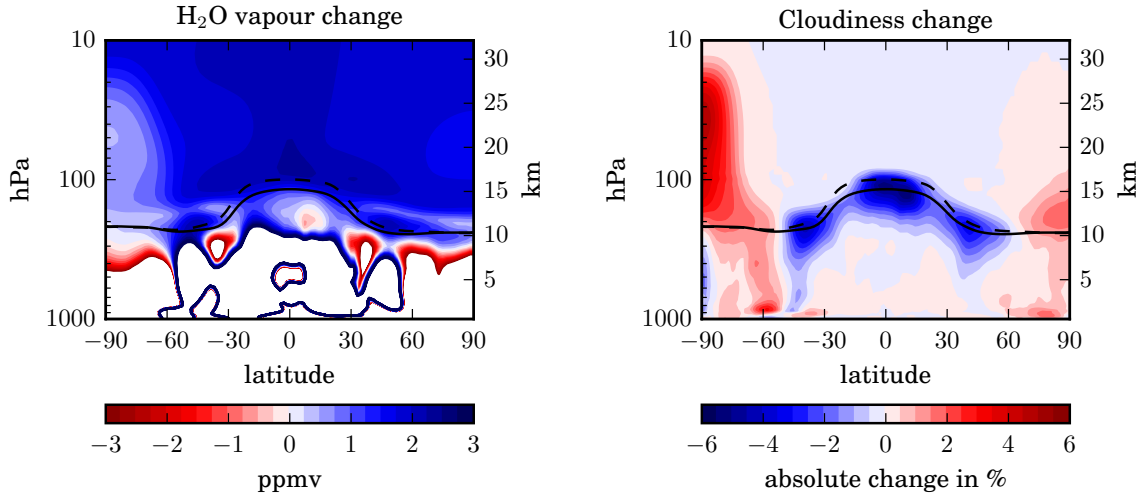

Figure 5.16: Change in water vapour mixing ratio (left, in ppmv) and in cloudiness (right, in %) in the STANDARD experiment, relative to the CONTROL experiment.

the modelled ERF into the IRF and the individual contributions of the different adjustments (for SW and LW components separately, see Table 5.3). Assuming linearity and additivity, this decomposition can be written as

$$ERF = IRF + K_\alpha \Delta\alpha + K_{T^{surf}} \Delta T^{surf} + \sum_j K_{T^{atm},j} \Delta T_j^{atm} + \sum_j K_{w,j} \Delta w_j + \sum_j K_{c,j} \Delta c_j \quad (5.2)$$

where $\Delta\alpha$ is the change in surface albedo, ΔT^{surf} the change in Earth surface temperature, ΔT_j^{atm} the change in atmospheric temperature, Δw_j the change in water vapour (humidity), Δc_j the change in clouds in the vertical model layer j, and the $K_{X(,j)}$ are the radiative response kernels of these individual changes. It may be difficult to calculate the contribution of cloud changes directly due to strong nonlinearities [Soden et al., 2008], but in our case the residual difference between IRF and ERF when accounting for changes in surface temperature, atmospheric temperature, and humidity should be dominated by the changes in cloudiness (as surface albedo changes are small). In practice, the radiative kernels are often computed *offline* with a different radiative transfer code than the IRF and ERF, which are determined with the climate model's radiative transfer code directly. Therefore, the equation does not always hold completely. This is also the case for the radiative kernel computations by Boucher, Kleinschmitt, and Myhre [2017] that we present here.

The result (see Table 5.3) shows that the stratospheric temperature increase contributes most to the difference between IRF and ERF. The increased emission of LW radiation to space by the warmer stratosphere causes a negative RF in the same order as the aerosol extinction. In contrast, the positive RF due to increased humidity and a slightly

Table 5.3: Decomposition of the effective radiative forcing (ERF) into instantaneous radiative forcing (IRF) and rapid adjustments (all quantities given in $W\,m^{-2}$) using the radiative kernel method from Myhre et al. [2011] for the STANDARD SAI experiment. The SW terms due to temperature changes are 0 by construction. The residual change terms are computed as the residual required to explain the SW, LW and net ERF. They can be attributed mostly to cloud changes but also have a contribution from surface albedo changes.

	SW	LW	net
IRF	–4.61	+3.08	–1.52
Change in surface temperature	0.0	+0.13	+0.13
Change in atmospheric temperature	0.0	–1.59	–1.59
Change in atmospheric humidity	+0.02	+0.17	+0.19
Residual change	+0.84	–0.88	–0.05
ERF	–3.75	+0.91	–2.84

decreased Earth surface temperature are small. Although a considerable decrease in cirrus clouds can be observed, the residual RF term (mostly attributable to clouds) is small. This can be explained by a compensation of the negative SW and the positive LW RF of high clouds, which are both rather large. It has to be noted that the relative importance of surface temperature changes would be higher in case of a simulation with a coupled ocean (and not fixed SSTs as used in the presented experiments).

Since the ERF is computed as a difference between two relatively independent experiments (with and without aerosol), it has to be averaged over several years in order to reduce the effect of inter-annual variability. In case of the longer STANDARD experiment we could average over the years 4 to 10 of the simulation (the first three years were excluded as the aerosol layer was still building up). For the other scenarios we use the years 4 to 6 to compute an ERF, which we can compare to the IRF already discussed above (see Figure 5.17).

As in the STANDARD scenario, the ERF efficiency ($W\,m^{-2}$ per $Tg\,S\,yr^{-1}$) is higher than the IRF efficiency for all injection magnitudes and injection heights. The additional negative RF due to rapid adjustments causes the ERF to increase monotonically with the injection magnitude, i.e. the largest injections result in the strongest surface cooling. Thus, the finding of a maximum achievable net IRF does not hold for the ERF, at least for the injections magnitudes simulated. This may be related to the stronger stratospheric heating for larger injections, hence a more important negative RF due to the atmospheric temperature adjustment. In case of different injection heights, we find that the ERF increases up to 21 km, while the IRF saturates already at 17 km. So it might be worth the effort to bring the material above 20 km. The optimal injection height may therefore depend on the metric used to measure the radiative forcing. Ultimately the optimal injection height has to be quantified using fully coupled ocean-atmosphere models so that the efficiency is measured in K per $Tg\,S\,yr^{-1}$ injected.

Finally, we may conclude that the potential of SAI with tropical injections of SO_2 to

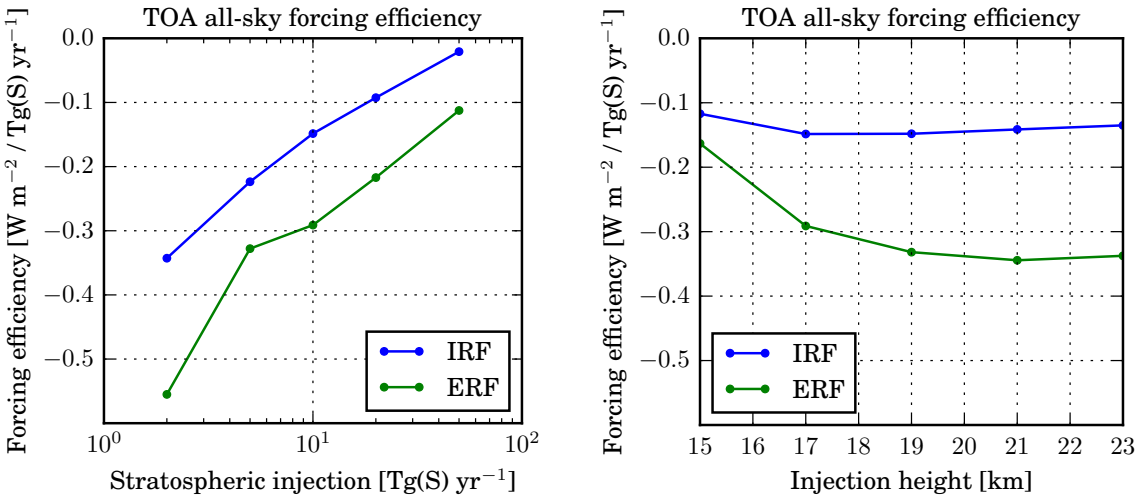

Figure 5.17: Global mean IRF and ERF efficiency in the experiments with different injection magnitudes (left) and different injection heights (right). The forcings were averaged over the years 4, 5, and 6 of the simulations in order to reduce the effect of inter-annual variability.

cool the Earth's surface, for which ERF probably is the better predictor, may be higher than estimated from the resulting IRF. But it has to be noted that the rapid atmospheric adjustments which contribute to the higher ERF represent an additional perturbation of SAI to the climate system. They may therefore result in more and stronger unintended side effects.

5.10 Impact of aerosol optical properties on the results

The LMDZ-S3A model computes the optical properties of the sulphate particles for the simulated local size distribution, but for a fixed temperature and composition (300 K and 75 % H_2SO_4 – 25 % H_2O) because the refractive index has been measured with some accuracy at these conditions. This is a notable limitation of the model in its current state, as temperature typically varies between 180 and 230 K and the modelled H_2SO_4 mass fraction between 60 and 85 % in the lower and mid stratosphere. In order to estimate the impact of this assumption, we performed an additional STANDARD SAI experiment using the refractive index data reported by Hummel et al. [1988] at 215 K and 75 % H_2SO_4 (see Figure 5.18 for a comparison of refractive index values at different temperatures and from different sources). It is important to note that refractive indices were not measured at this temperature by Hummel et al. [1988] but rather inferred from interpolation and extrapolation of earlier measurements at other temperatures. Using 215 K values results in a reduction of the positive LW RF by about 30 % and a

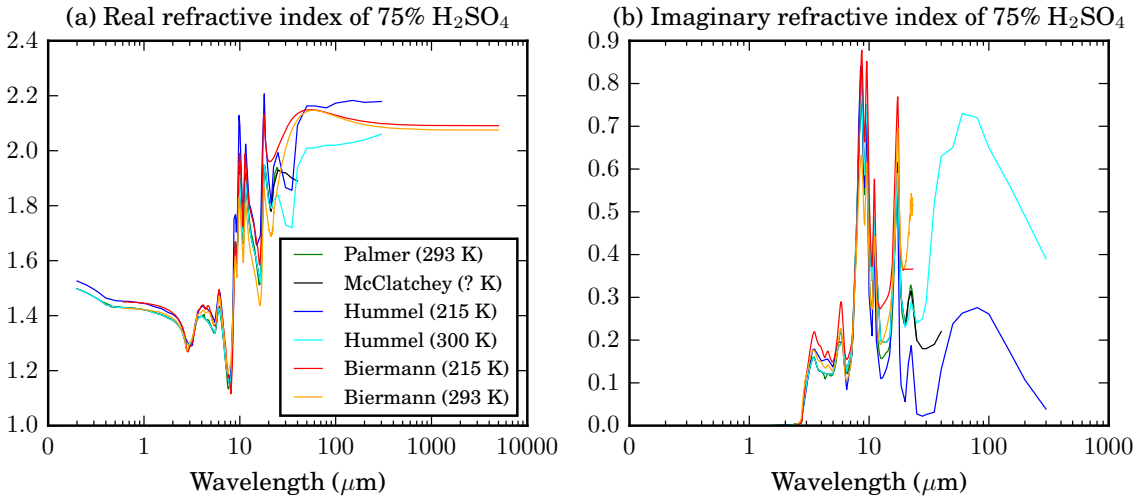

Figure 5.18: Comparison of (a) real and (b) imaginary refractive index of a 75 % H_2SO_4 – 25 % H_2O solution from different sources [Palmer and Williams, 1975, McClatchey et al., 1984, Hummel et al., 1988, Biermann et al., 2000].

reduction of the negative SW RF by 5-10 %. Hence, the net RF increases by almost 50 % relative to the experiment with 300 K refractive index values.

The aerosol models used in previous studies included different refractive index data: English et al. [2012] and Niemeier and Timmreck [2015] used values at 293 K from Palmer and Williams [1975], Jones et al. [2016] used values from McClatchey et al. [1984] (at unspecified temperature), while Heckendorn et al. [2009] and Dykema et al. [2016] used temperature and composition dependent values from Biermann et al. [2000] (see Figure 5.18). These different values agree rather well in the SW, but differ considerably in the infrared. Furthermore, the refractive index changes remarkably with temperature and probably even more with the composition of the solution. Therefore, the use of different refractive index values from different (more or less representative) conditions may be an important cause of disagreement between model results. It is thus important to obtain accurate measurements of refractive indices of sulphuric acid solution (and any other candidate aerosol types) for a range of humidity (and hence chemical composition) and temperatures typical of the stratosphere and to include them in the various aerosol models.

5.11 Sulphate impact at the Earth's surface

The deposition of acids at the land or ocean surface can be harmful to ecosystems. Although the additional input of sulphur species to the Earth system is (at least for the lower emission scenarios) not large compared to the already existing anthropogenic and natural inputs (of about 136 $\mathrm{Tg\,S\,yr^{-1}}$ [Kravitz et al., 2009]) sulphate SAI constitutes an additional and intentional sulphur input. Therefore, it is important to study the deposition fluxes of sulphuric acid due to SAI. Before their deposition, sulphate particles near the surface can also have a negative impact on human health by increasing particle concentrations in ambient air ($PM_{2.5}$).

Due to the relatively short lifetime of the sulphate particles in the troposphere, the relevance and relative importance of the various processes at play are different than in the stratosphere. Therefore, we decided not to activate the microphysical processes of coagulation, nucleation, condensation and evaporation below the tropopause. Thus, the particles do not grow or shrink any more, but they are removed via wet and dry deposition (both independent of the particle size) and sedimentation.

However, our model setup makes it possible to study in first approximation the contribution of SAI to increase particle concentration at the Earth's surface (i.e., in the lowest atmospheric model layer) as well as the deposition rate of aerosols to the ground or sea surface.

The deposition rate of sulphate aerosol coming from the stratosphere to the surface in the STANDARD scenario is shown in Figure 5.19. It is largest in the low and mid-latitudes and over the ocean, where it reaches up to $82\,\mathrm{mg\,S\,m^{-2}\,yr^{-1}}$. This spatial distribution is similar to the one shown by Kravitz et al. [2009]. However, the absolute values of the deposition anomaly shown by Kravitz et al. [2009] are larger than in our simulations because their anomaly includes changes in the deposition of tropospheric sulphur (between two simulations with and without SAI), which is not the case in our model. On a global average, wet deposition contributes 68 %, dry deposition 28 %, and sedimentation 4 % to the total deposition rate at the surface.

For estimating the impact in terms of acidic deposition on ecosystems, we convert the deposition rate of sulphur from $\mathrm{mg\,S\,m^{-2}\,yr^{-1}}$ to $\mathrm{mEq\,m^{-2}\,yr^{-1}}$ (used in critical loading studies like Kuylenstierna et al. [2001], cited by Kravitz et al. [2009]) using a conversion factor of 16 mg S = 1 mEq. With this, the largest additional deposition rates (due to aerosol from SAI) in our simulation are equivalent to $5\,\mathrm{mEq\,m^{-2}\,yr^{-1}}$. This is well below the critical loadings for almost all ecosystems reported by Kuylenstierna et al. [2001] and on the very low side for the most sensitive type of ecosystems (e.g., waterways in Sweden, which have a critical load of 1–44 $\mathrm{mEq\,m^{-2}\,yr^{-1}}$).

Kravitz et al. [2009] gives a global mean value of $270\,\mathrm{mg\,S\,m^{-2}\,yr^{-1}}$ for the present-day deposition rate of tropospheric sulphur. Compared with this large number, our

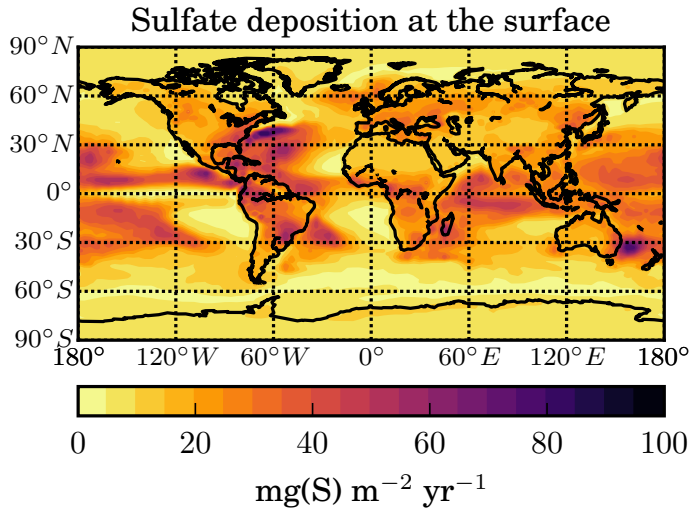

Figure 5.19: Annual mean deposition rate of sulphate aerosol of stratospheric origin at the Earth's surface (in mg S m^{-2} yr^{-1}) in the STANDARD scenario.

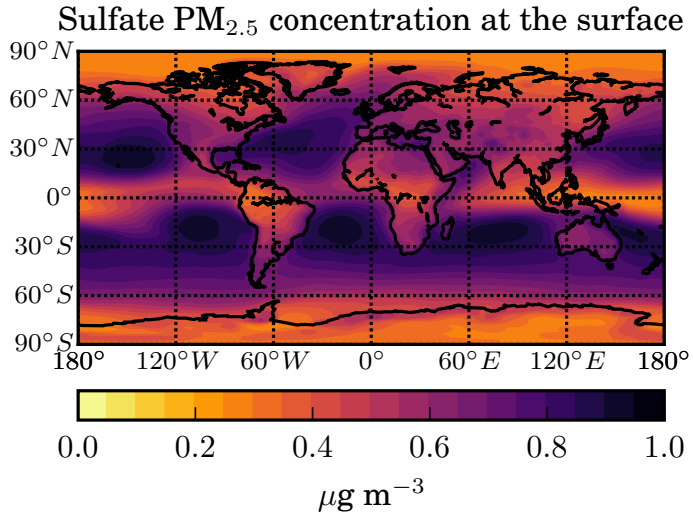

Figure 5.20: Annual mean concentration of sulphate aerosol particles (as ammonium sulphate) of stratospheric origin with dry diameter below 2.5 µm at the Earth's surface (in µg m^{-3}) in the STANDARD scenario.

simulated global mean additional sulphate deposition due to SAI of $18\,\mathrm{mg\,S\,m^{-2}\,yr^{-1}}$, but even the maximum value of $82\,\mathrm{mg\,S\,m^{-2}\,yr^{-1}}$ is rather small.

In order to assess the possible impact on human health, we also compute the concentration of $PM_{2.5}$ at ground level due to aerosol particles coming from the stratosphere. For this we take the sum over the aerosol mass in all size bins with dry diameter lower than 2.5 μm, assuming that they consist of ammonium sulphate with a density of $1.77\,\mathrm{g\,cm^{-3}}$. Due to this choice, we probably overestimate $PM_{2.5}$, because the wet radius of some of these particles is actually above 2.5 μm. Allowing the particles to grow further in the troposphere would also result in smaller concentrations of small particles.

The additional $PM_{2.5}$ concentration at the surface due to SAI is shown in Figure 5.20. It does not exceed $1\,\mathrm{\mu g\,m^{-3}}$ and is largest over the ocean, where the model assumes the lowest dry deposition velocities, thereby increasing the aerosol lifetime in the marine boundary layer. In order to get a rough estimation of the impact of this additional $PM_{2.5}$ on human health, we first compute the product of $PM_{2.5}$ from SAI and human population count (2015 values from SSP1, see Riahi et al. [2017]) at the grid cell level and cumulate these values over the whole Earth. This cumulative sum is $4.2 \cdot 10^9\,\mathrm{\mu g\,m^{-3}}$ person, which is approximately 2% of the value found using present day $PM_{2.5}$ values from van Donkelaar et al. [2016] at $2.4 \cdot 10^{11}\,\mathrm{\mu g\,m^{-3}}$ person. Although previous studies [e.g. Partanen et al., 2013] translated such changes in surface PM concentrations into mortality or morbidity rates, we do not attempt to do so as the health impact of PM is dependent on aerosol size and chemical composition in ways that are unknown.

5.12 Conclusions on the stratospheric aerosol injection simulation results

The model results for various scenarios of stratospheric aerosol injections (SAI) with SO_2 presented in this chapter imply that the net radiative forcing achievable through equatorial SAI might be smaller than previously estimated. One reason is that the radiative heating through the aerosol can disturb the stratospheric dynamics in such a way that the meridional transport is hindered. This results in larger sulphate concentrations in the tropics, which enhances particle growth. The larger particles are responsible for an important positive LW forcing, which can compensate the negative SW forcing (cooling) almost completely for large SO_2 injection rates like $50\,\mathrm{Tg\,S\,yr^{-1}}$ (the maximum rate simulated in this study). We find that it might be impossible to achieve a more negative net instantaneous radiative forcing than $-2\,\mathrm{W\,m^{-2}}$ with equatorial SO_2 injections alone.

We also find that SO_2 injections at higher altitude (in the range 17 to 23 km) do not result in larger (i.e., more negative) radiative forcing, because the particles grow to larger size during their stratospheric lifetime and have less optimal optical properties. This finding contradicts previous studies by English et al. [2013] and Niemeier and Timmreck [2015] but agrees with a recent study by Niemeier and Schmidt [2017].

Enlarging the injection area from one equatorial grid cell to several grid cells between 30°S and 30°N resulted in smaller particles, but also in a smaller global aerosol burden, which in total causes the net radiative forcing to be equal to the one from equatorial injections. Restricting the injections to a shorter period of the year with seasonally varying latitude resulted in a small increase in net radiative forcing, but probably only due to stronger updraft (more heating from larger sulphate concentrations), which might be overestimated by the model.

The simulated impact on stratospheric dynamics through radiative heating by the aerosol agrees with a previous study by Aquila et al. [2014] in that the QBO breaks down for injection rates larger than about $5\,\mathrm{Tg\,S\,yr^{-1}}$. This results in a stronger subtropical transport barrier, which causes the particles to grow even larger than in the case of an unperturbed circulation.

In contrast, the impact of the additional sulphate at the Earth's surface is probably small. In the $10\,\mathrm{Tg\,S\,yr^{-1}}$ scenario, the maximum additional acidic deposition flux is below the critical load for almost all ecosystems and the additional particle concentrations ($PM_{2.5}$) are below $1\,\mu\mathrm{g\,m^{-3}}$, resulting in a small 2 % increase of population-weighted $PM_{2.5}$ relative to present-day conditions.

In our experiments we found that the positive LW forcing can compensate a large part of the negative SW forcing, i.e. 67 % in the STANDARD $10\,\mathrm{Tg\,S\,yr^{-1}}$ and 93 % in the $50\,\mathrm{Tg\,S\,yr^{-1}}$ scenario. This is because the LW absorption scales almost linearly with the aerosol mass, whereas the SW scattering strongly depends on the particle size that changes with the injection magnitude. Therefore, we argue that the LW forcing should always be considered in modelling studies of SAI, which has not often been the case in the past. Considering only the SW forcing of SAI will lead to considerable overestimation of its efficacy.

We also analysed rapid adjustments of the climate system to the instantaneous radiative forcing (IRF) by the aerosol. We found that rapid adjustments significantly enhance the effective radiative forcing (ERF) relative to IRF, mostly because of stratospheric warming and despite a moistening of the stratosphere. The simulated decrease in cirrus clouds has a considerable (opposite) impact on SW and LW radiative fluxes, but its net effect is probably negligible. The cooling potential of SAI, which is more related to ERF, may therefore be higher than estimated from IRF, especially for scenarios with stronger stratospheric warming.

As the simulation results depend largely on the modelled evolution of particle size, radiative heating and stratospheric dynamics (controlling the spatial distribution), it

would be worthwhile to compare them with other models, like we did it in Sec. 5.4. Further intercomparison could increase the robustness of the findings from this study and it could also help to further improve the models by examining differences in more detail.

It has to be noted that the results presented in this chapter are strongly influenced by the choice of the injection scenarios, although we did not find large differences between those scenarios that we simulated. Spreading the injections over larger areas would lower the local concentrations of precursor gases and sulphate and would therefore probably result in less particle growth and more favourable optical properties. Smaller local extinction by the aerosol would also cause less heating and probably less updraft of the particles, which may increase the importance of the initial injection height. Hence, our finding that higher injections do not result in larger radiative forcing (for a given sulphur mass), may not hold for different injection schemes.

The phenomenon of aerosol lifting through local heating and dynamical changes might also be used for the design of better injection strategies, as it could allow technically less demanding injections (e.g. with conventional aircraft) at lower altitudes. But as the larger local sulphate concentrations required for the updraft will probably also enhance particle growth, it is unclear whether such a strategy could be more efficient at all. One could possibly imagine methods to increase the buoyancy of the initial aerosol (or aerosol precursor) plume that have less impact on particle growth.

6 Combining stratospheric aerosol injection (SAI) and marine cloud brightening (MCB)

After having studied the effects of various scenarios of SAI in the previous chapter, we will now widen our focus to examine another proposed SRM technique: marine cloud brightening (MCB), i.e. the idea to increase the albedo of low-level clouds over the ocean by spraying additional cloud condensation nuclei (CCN, e.g. sea salt particles) with a consequent increase in the cloud droplet number concentration [e.g. Latham, 1990, Salter et al., 2008]. The approach of MCB is rather different from SAI. It would not require to bring material to high altitudes, but to spread them in the lower troposphere, although probably in much larger amounts. The radiative effects of MCB would be regionally limited to certain parts of the oceans, and they would not be as persistent as those of SAI due to much shorter residence times of particles in the troposphere compared to the stratosphere. Jones et al. [2011] showed that the different radiative effects of SAI and and MCB would also result in different climate responses. But so far it has not been studied how the effects of both techniques would combine. Such a combination of different SRM techniques could possibly be used if the efficacy of a single method turned out to be insufficient, or in order to reduce the side effects of the excessive deployment of one method. Therefore, we use the newly available tool LMDZ-S3A to perform model experiments of SAI and MCB alone, and of a combination of both for studying how their radiative forcings and the consequent rapid adjustments would interact. The results shown in this chapter are also part of a publication by Boucher, Kleinschmitt, and Myhre [2017].

6.1 Simulation setup

We use the same model configuration of LMDZ-S3A as for the SAI experiments presented in the previous chapter, except one difference related to the simulation of MCB: In LMDZ, the cloud droplet number concentration (CDNC) in liquid clouds is parametrised as a function of the mass concentration of soluble accumulation-mode

aerosol in the following way:

$$\mathrm{CDNC} = 10^{A+B\cdot\log_{10}\sum_i m_i} \tag{6.1}$$

with CDNC in cm^{-3}, m_i the mass concentration of aerosol species i (sea salt, sulphate, organics, and black carbon) in $\mu\mathrm{g\,m}^{-3}$, and the parameters having default values of $A = 1.7$ and $B = 0.2$. But as the effect of elevated aerosol concentrations on CDNC turned out to be surprisingly small with these values, we used the values $A = 2.06$ and $B = 0.48$ reported by Boucher and Lohmann [1995] instead. The model then computes the cloud droplet size from the CDNC and the liquid water content of the cloud. As a recent study by Malavelle et al. [2017] found that the effect of aerosol particles on the cloud liquid water path and precipitation is probably small, we only account for the cloud albedo effect (i.e. a brightening due to smaller droplets) in this experiment. In earlier simulations, the model's simple CDNC parametrisation with default parameters resulted in a present-day aerosol-cloud interaction IRF of about -0.8 $\mathrm{W\,m}^{-2}$ relative to pre-industrial conditions. This is larger than the IPCC best estimate for the ERF of -0.45 $\mathrm{W\,m}^{-2}$ [Boucher et al., 2013], and the modified parameters might increase this overestimation of aerosol-cloud interactions by the LMDZ model. Therefore, in reality higher sea salt aerosol concentrations might be needed to achieve the simulated cloud brightening effect, which would probably also result in a more important direct aerosol-radiation interaction.

In the performed model experiments, MCB is implemented by adding accumulation-mode sea salt aerosol to the model's aerosol climatology over the ocean between 30°S and 30°N. The additional aerosol concentration decreases exponentially (with a scale height of 0.5 km) from 10 $\mu\mathrm{g\,m}^{-3}$ at the ocean surface to 0.5 $\mu\mathrm{g\,m}^{-3}$ at an altitude of 1.5 km. We allow the sea salt aerosol to interact with radiation directly, i.e. through scattering, and indirectly, i.e. through the brightening of clouds, because earlier studies by Alterskjær et al. [2013] and Kravitz et al. [2013b] found that the aerosol direct effect (ADE) of MCB could be about twice as strong as the aerosol indirect effect (AIE). The experiment with this implementation of MCB is called MCB-DI. Originally, we also performed experiments including only the indirect effect of MCB (called MCB-I), but they shall not be further considered here, as the ADE (also called clear-sky radiative effect) of MCB proved to be non-negligible. SAI is implemented in the same way as in the STANDARD experiment of the previous chapter (see Table 5.1), but here with the same modified CDNC parameters as in the MCB experiments. These parameters are also used in the CONTROL experiment with background stratospheric aerosol and climatological tropospheric aerosols. In the SAI+MCB-DI experiment, both SAI and MCB are implemented simultaneously, with direct and indirect effects of MCB and direct effects of SAI. All experiments are run with the same fixed present-day sea surface temperatures and sea ice cover and have a duration of 10 years. This allows to study IRF, rapid adjustments, and ERF, but not the full climate impact of SAI and/or MCB (for which a coupled ocean would be needed). As in the previous chapter, we

exclude the first 3 years from the analysis, as the enhanced stratospheric aerosol layer needs this time to build up.

6.2 Aerosol direct vs. indirect effect in the MCB experiment

The relative contribution of the additional sea salt ADE and AIE to the RF of MCB can be compared to previous studies. In our MCB-DI experiment, the global and annual mean ADE is about –0.7 $W\,m^{-2}$, while the AIE is about –1.0 $W\,m^{-2}$. Hence, both effects are roughly of the same order and the ADE is certainly not negligible compared to the AIE. This agrees qualitatively with earlier studies, although the ratio of ADE and AIE may be different (Alterskjær et al. [2013] and Kravitz et al. [2013b] found an ADE/AIE ratio near 2:1). But this ratio depends considerably on the choice of the additional sea salt concentration distribution and of the CDNC parametrisation. Therefore, the simulated ADE may easily be larger than the AIE for a slightly different choice of these parameters.

6.3 Rapid adjustments and effective radiative forcing of MCB

Compared to the strong rapid adjustments to SAI presented in Section 5.9, the adjustments to MCB are negligible. No significant change in atmospheric temperature can be observed (see Figure 6.1), so that stratospheric water vapour remains unchanged (see Figure 6.2). The small change in cloudiness (see Figure 6.3) may be related to minor changes in tropospheric dynamics as a response to the locally strong IRF of MCB. The resulting ERF of MCB is slightly smaller than the IRF (see Table 6.1) due to a weak positive ERF contribution from regions outside the MCB deployment zone (see Figure 6.4d).

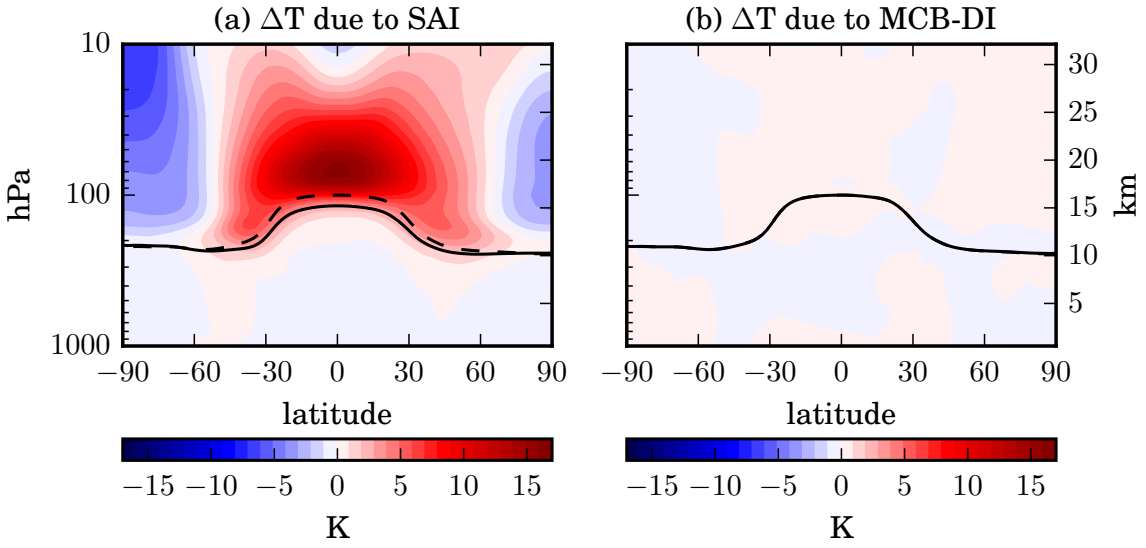

Figure 6.1: Zonal mean of the absolute change in temperature (K) between (a) the SAI and the CONTROL experiments and (b) the MCB-DI and the CONTROL experiments. The mean tropopause levels as diagnosed in the SRM and CONTROL experiments are indicated by a solid and a dashed line, respectively.

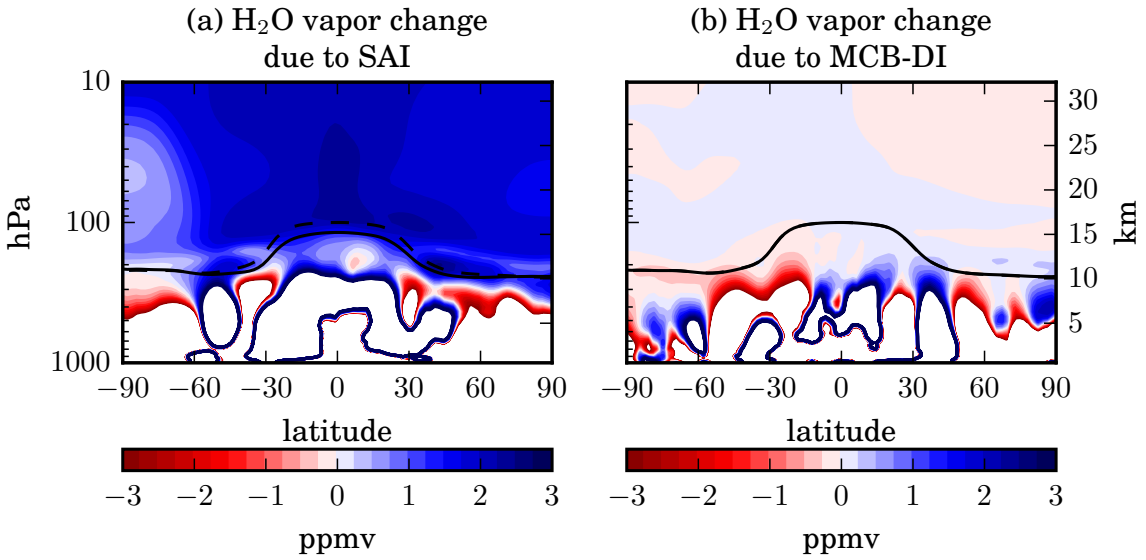

Figure 6.2: Same as Figure 6.1 but for the absolute change in stratospheric water vapour (ppm). White areas correspond to tropospheric changes that are larger than spanned by the color scale.

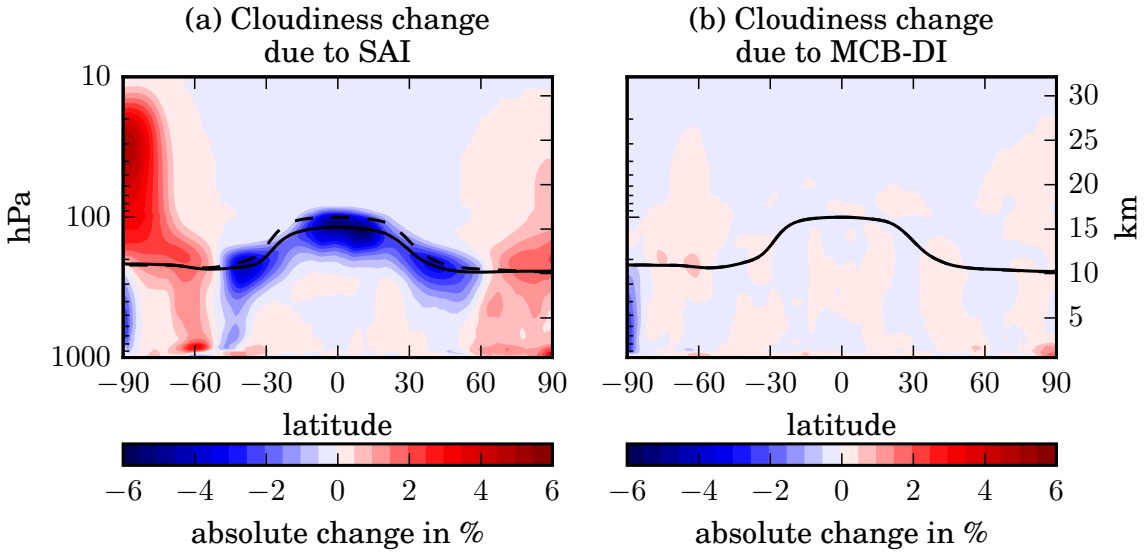

Figure 6.3: Same as Figure 6.1 but for the absolute change in cloudiness (%).

6.4 Spatial differences between instantaneous and effective radiative forcing

The spatial distribution of IRF and ERF in the individual SAI and MCB-DI experiments and in the combined experiment is shown in Figure 6.4. In the case of SAI, the IRF is weakest and regionally even positive (i.e. warming) where surface and/or cloud albedo below the stratospheric aerosol layer are already high. This is especially the case over deserts, ice sheets, and relatively cloudy parts of the tropical oceans. The rapid adjustments to the IRF increase these regional differences, so that the ERF is more negative where IRF is negative, and ERF is more positive where IRF is positive or only slightly negative. In the MCB-DI experiment, regions of significantly negative IRF (i.e. the cloudy parts of the tropical oceans) experience a slightly weaker negative ERF, while regions with negligible IRF have a positive ERF. This might possibly be caused by a slightly increasing vertical transport of water vapour (with a small additional greenhouse effect) outside the simulated MCB deployment area as a response to the increased stratification within the MCB area due to the negative RF of MCB.

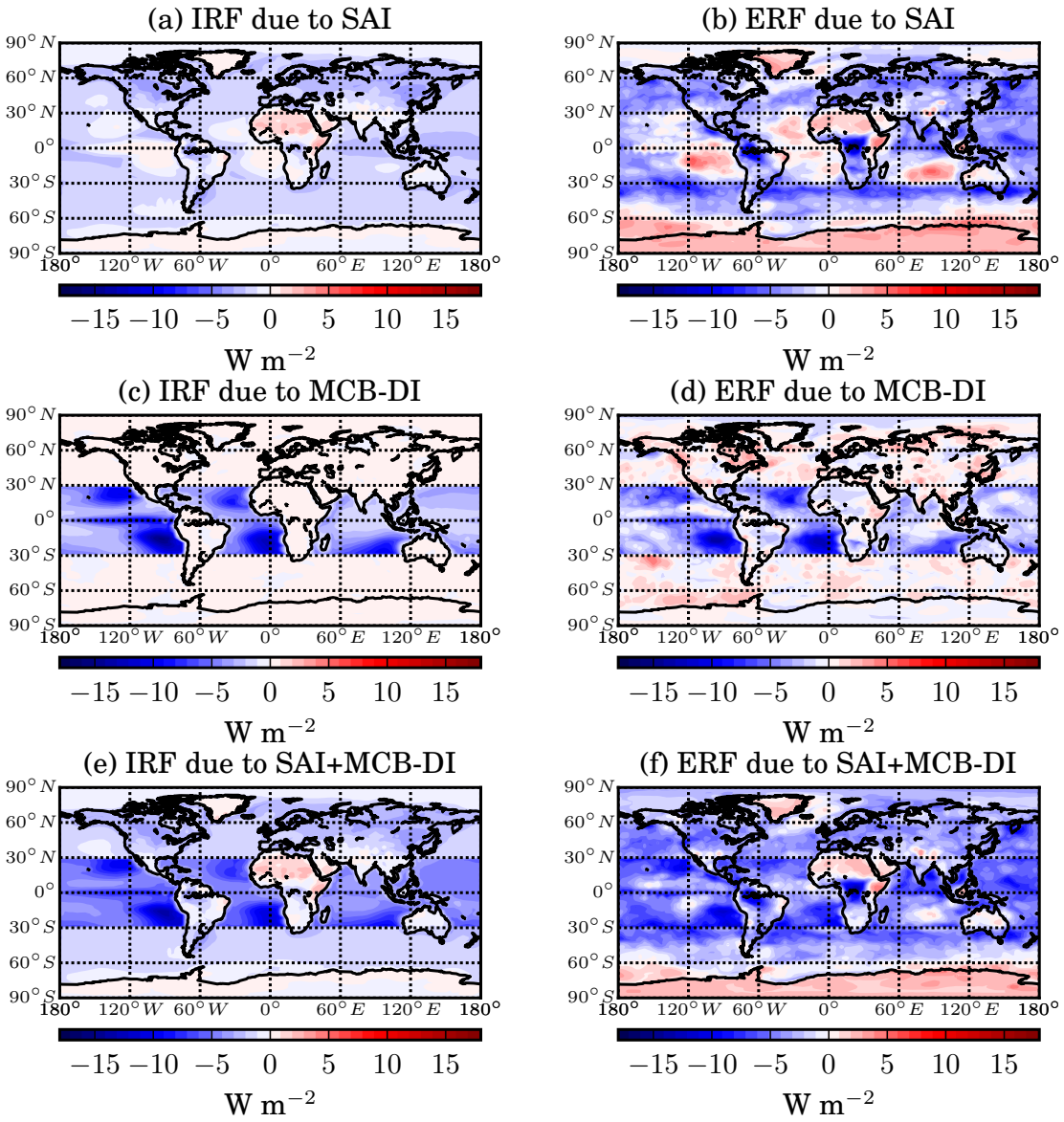

Figure 6.4: Instantaneous top-of-the-atmosphere net radiative forcing (IRF, in W m^{-2}, left column) computed from double radiation call for SAI (a), MCB-DI (c), and SAI+MCB-DI (e) and effective net radiative forcing (ERF, in W m^{-2}, right column) computed from differences in top-of-the-atmosphere radiative fluxes between parallel fixed-SST experiments for SAI (b), MCB-DI (d) and SAI+MCB-DI (f).

Table 6.1: Global mean quantities and their standard deviations from the SRM experiments computed over the years 4 to 10 of the simulations: top-of-atmosphere instantaneous radiative forcing (IRF) and effective radiative forcing (ERF) in $W\,m^{-2}$, surface temperature ($\overline{T_s}$) change in K, and precipitation ($\overline{P}$) change in $mm\,yr^{-1}$. The ERF, temperature changes, and precipitation changes are computed relative to the CONTROL experiment. The standard deviations are computed from the annual means of years 4 to 10.

		SAI	MCB-DI	SAI+MCB-DI (combined exp.)	Sum of SAI and MCB-DI**
IRF ($W\,m^{-2}$)	SW	–4.5 ± 0.04	–1.7 ± 0.01	–6.0 ± 0.05	–6.2 ± 0.04
	LW*	+3.1 ± 0.03	+0.0 ± 0.00	+3.0 ± 0.03	+3.1 ± 0.03
	net	–1.4 ± 0.02	–1.7 ± 0.01	–2.9 ± 0.04	–3.1 ± 0.02
ERF ($W\,m^{-2}$)	SW	–3.5 ± 0.24	–1.5 ± 0.15	–4.9 ± 0.17	–5.0 ± 0.28
	LW	+0.9 ± 0.12	–0.1 ± 0.14	+0.8 ± 0.20	+0.8 ± 0.19
	net	–2.6 ± 0.13	–1.6 ± 0.19	–4.0 ± 0.14	–4.2 ± 0.23
$\overline{T_s}$	(K)	–0.15 ± 0.08	+0.02 ± 0.03	–0.16 ± 0.05	–0.13 ± 0.08
$\overline{P}$	($mm\,yr^{-1}$)	–7.7 ± 2.3	–4.0 ± 2.9	–9.3 ± 2.9	–11.7 ± 3.7

* The LW component of the MCB IRF is 0 by construction.
** The standard deviations for the sum of the two experiments are computed from the sum of the variances for the SAI and MCB experiments assuming independence.

6.5 Additivity and complementarity between SAI and tropical MCB

The global mean values of IRF and ERF (averaged over the years 4 to 10) are shown in Table 6.1. It is remarkable, how close the sum of the values in the individual SAI and MCB-DI experiments is to the value in the combined experiment: the combination has a 7 % lower net IRF and a 4 % lower net ERF than the sum of the individual experiments. We can therefore call the radiative effects of SAI and MCB nearly additive. This is not completely self-evident, as normally RF does not scale linearly with scattering optical depth [e.g., Boucher et al., 1998]. But as the geographical distribution of the annual mean RF of SAI and MCB is rather complementary (see Figure 6.4), in most regions the radiative effect of one technique is small compared to the other, so they hardly interfere. Therefore, the RF is also nearly additive on the grid-box level, as shown in Figure 6.5. The IRF of the combined experiment and the sum of the individual IRFs are highly correlated between 30°S and 30°N with a correlation coefficient of 0.996. For the ERF the correlation between 90°S and 90°N is slightly lower due to the variability of the rapid adjustments, but still high with a correlation coefficient of 0.896. Overall, the complementarity causes the ERF to be spatially surprisingly homogeneous in the SAI+MCB experiment.

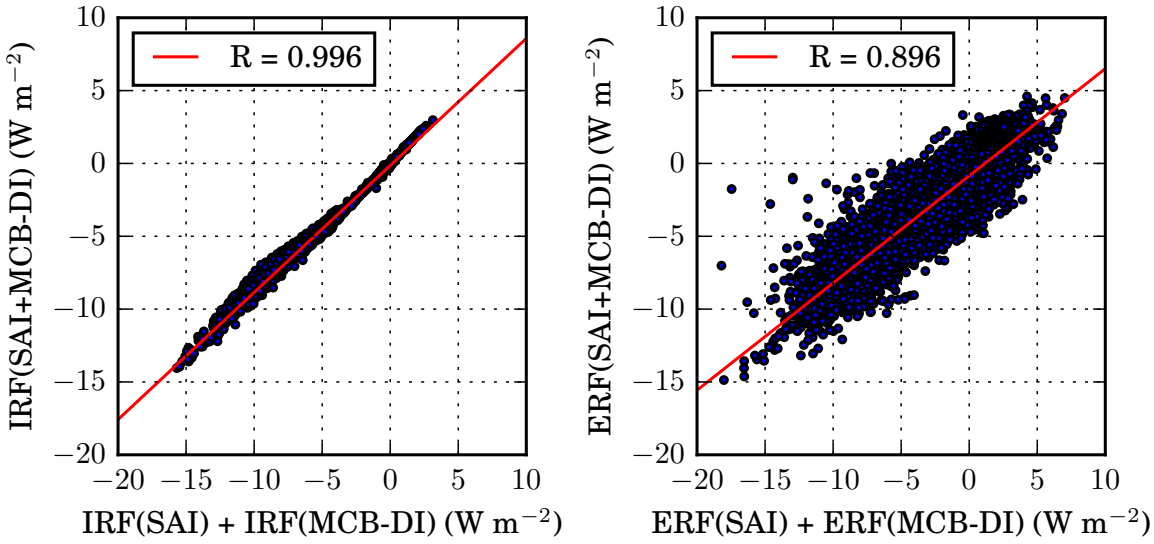

Figure 6.5: Left: IRF in the combined SAI+MCB-DI experiment plotted against the sum of the IRF from the single SAI and MCB-DI experiments for all model grid-boxes between 30°S and 30°N. Right: The same plot for the ERF and all grid-boxes between 90°S and 90°N.

6.6 Conclusions on simulations of SAI and MCB

In the model experiments presented in this chapter, the combination of SAI and MCB was studied for the first time with a climate model. We found that the RF of both techniques is nearly additive, at least partly due to the spatial complementarity of the two RFs. The chosen deployment scenarios result in a fairly homogeneous ERF on the global scale. But it is an open question whether a more homogeneous ERF would translate into a spatially more homogeneous cooling of the Earth's surface, as this also depends on the transport and redistribution of energy in the atmosphere and particularly in the ocean. This would have to be studied with a coupled atmosphere-ocean model. However, we demonstrated that combining two different SRM techniques may allow to have more control over the resulting distribution of radiative forcing and potentially of climate impacts. This result may contribute to the scientific discussion on the controllability of geoengineering impacts [Kravitz et al., 2016].

7 Conclusions

7.1 Summary

In this thesis we first summarised the current state of the science on geoengineering with stratospheric aerosol injections (SAI) in Chapter 2. We showed that there is a need for accurate, interactive stratospheric aerosol models within climate models in order to study the characteristics of the aerosol distribution in size and space that SAI would produce, and in which radiative forcing (RF) this would result. In Chapter 3 we presented the new stratospheric atmosphere-aerosol model LMDZ-S3A which we developed as a tool to study SAI. The model uses a sectional approach for stratospheric sulphate aerosol with a wide range of particle sizes. It includes relevant gaseous precursors, their conversion to sulphate particles, important microphysical aerosol processes, and allows full interaction between the aerosol effects on (solar and terrestrial) radiation and atmospheric dynamics, which are especially well-resolved in the stratosphere. The performance of the LMDZ-S3A model against stratospheric aerosol observations was evaluated in Chapter 4. The model reasonably reproduces aerosol observations in periods of low (background) and high (volcanic) stratospheric sulphate loading, but it tends to overestimate the number of small particles and to underestimate the number of large particles in comparison to available observations. It probably also overestimates the stratospheric heating by the aerosol, at least partly because it does not include a feedback on ozone concentration (which is expected to decrease in the presence of aerosols, resulting in a reduced heating through ozone absorption). Further limitations of LMDZ-S3A are its semi-prescribed sulphur chemistry, which may result in an overestimation of sulphuric acid formation rates in case of very high precursor concentrations, and the use of optical aerosol properties from a fixed set of conditions (300 K, 75 % H_2SO_4 – 25 % H_2O).

Despite these limitations, LMDZ-S3A can be used to study the potential efficacy and impacts of SAI, which we did in Chapter 5. We simulated different scenarios of SAI, varying the magnitude, the height, and the spatio-temporal pattern of the SO_2 injections. We found that the RF achievable with equatorial injections might be smaller than estimated in previous studies. The global mean instantaneous RF (IRF) did not exceed $-2\,W\,m^{-2}$, even when further increasing the injection rate, while the effective RF (ERF), including the radiative effects of rapid adjustments to the aerosol IRF, increased monotonically with injection rate. But for both, IRF and ERF, the forcing efficiency (i.e.

the forcing per $\mathrm{Tg\,S\,yr^{-1}}$ injected) decreased strongly for larger injections. Therefore, it might require enormous effort or even turn out to be impossible to compensate the warming by high GHG concentrations with equatorial injections of SO_2 alone. Increasing the injection height, which previous studies suggested would increase the forcing efficiency, did not result in a larger cooling capacity in our simulations. The same holds for spreading of the injections over a larger area in the tropics and for injections restricted to shorter time periods and with seasonally varying latitude: both scenarios did not result in a larger forcing efficiency. But as these findings are based on a rather limited set of SAI scenarios, they do not exclude the possibility of more efficient injection strategies (especially with the injection of sulphuric acid vapour or other aerosol materials).

Besides the intended direct RF of SAI, which would on average cause a cooling of the Earth's surface, we studied rapid adjustments of the climate system to the aerosol forcing, impacts on stratospheric dynamics, and effects of particles reaching the Earth's surface. The main impact would probably be a heating of the stratosphere and upper troposphere through absorption of SW and LW radiation by the aerosol. This would increase the concentration of water vapour in the stratosphere (with an additional greenhouse effect and probably a negative impact on ozone chemistry), reduce the cirrus cloud cover in low and mid latitudes, and strongly perturb stratospheric transport patterns such as the QBO (thereby hindering the meridional transport of the aerosol). In contrast to these considerable impacts on the atmosphere, the simulated effects of particles reaching the Earth's surface are rather small. The additional concentrations of particulate matter in ambient air due to SAI are much smaller than from current tropospheric air pollution and would mainly occur over the oceans, while the deposited amount of sulphuric acid would be below critical ecosystem loadings practically everywhere.

After studying the effects of SAI, we performed model experiments of another geoengineering technique, marine cloud brightening (MCB), and combined both techniques in one experiment to evaluate their interactions and additivity in Chapter 6. We found that the global mean RF of SAI and MCB is largely additive. Furthermore, their spatial distribution is rather complementary, which minimises non-linear interactions of the forcings. The complementarity results in a spatially more homogeneous ERF, but whether this reduces regional disparities of the climate impact would have to be studied with a coupled ocean-atmosphere model. Nevertheless, designed geoengineering portfolios based on combinations of different SRM techniques might allow to achieve specific global and regional climate goals better than individual techniques.

Overall, this thesis provides additional evidence that solar radiation management with stratospheric sulphate aerosols is still more complicated, probably less effective and may implicate stronger side effects than initially thought. It has to be stated that even if a technically and economically feasible SRM method capable of effectively compensating GHG warming with minimal side effects was developed in the future, it

would still pose a major challenge in terms of governance and ethics. And it would certainly not relieve humanity from the need for strong GHG emission reductions, as SRM could only temporarily mask the GHG-induced warming. Indeed, it would neither abate other GHG effects like ocean acidification nor remove the main cause of global warming.

7.2 Perspectives

A variety of possible future research activities arise from the work presented in this thesis. They can be separated into further evaluation of the model, further model development, and application of the model for further studies of stratospheric aerosols and their impacts.

The performance of LMDZ-S3A could be evaluated against more aerosol observations from background periods or from smaller volcanic eruptions in the recent past. In the case of larger volcanic eruptions in the more distant past (like Tambora in 1815) or scenarios of SAI, for which only few or no observations are available, standardised intercomparisons with other aerosol-climate models could help to find and explain sources of model disagreements (like optical properties, particle growth processes, or resolved atmospheric dynamics). Especially the stratospheric heating by the aerosol would be an interesting and important aspect to compare, as it can have a large impact on the distribution and effects of the aerosol.

The model could also be improved by combining it with existing Earth system model components or by developing new capabilities. Coupling the atmospheric model to an ocean model (NEMO), as can be done in the framework of the IPSL climate model, would allow to study the full impact of stratospheric aerosols on climate, while coupling to a chemistry model (INCA or REPROBUS) could be used to evaluate the impact on ozone and how this changes the modelled stratospheric heating. A smaller step to improve the chemical aspects of the model would be to implement a feedback of the aerosol and its precursors on the availability of oxidants for chemical conversions. This would probably improve the model's reliability when simulating very large volcanic eruptions or sulphur injections. The aerosol optics could be improved by implementing temperature and composition dependent refractive indices, e.g. those measured by Biermann et al. [2000]. Adding a plume model or parametrisation for aerosol formation and growth below the grid-box scale would allow to study the possibly more effective direct injection of sulphuric acid vapour [Pierce et al., 2010]. Also, other types of aerosol could be added to the model in order to study their potential for SAI with reduced side effects compared to sulphate. But this might increase the model's computational cost considerably, as a number of size classes of the new aerosol would have to be added to those of the sulphate aerosol (which would probably still be non-negligible), together with classes of the new aerosol mixed or coated with sulphate.

The LMDZ-S3A model in its current or an enhanced configuration could be used for further modelling studies. Scenarios of SAI with other spatio-temporal injection patterns than those discussed in Chapter 5 could be simulated in order to find out if the forcing efficiency could still be increased. For example, injections spread over much more than the 28 grid boxes in our BROAD scenario could result in more favourable optical properties. Schemes with an injection rate and location more adapted to seasonal variations in insolation and atmospheric chemistry, like those studied by Laakso et al. [2017], could maximise the cooling capacity of a given sulphur mass. LMDZ-S3A in a configuration coupled to an ocean model could be used for simulations of the predefined GeoMIP scenarios [Kravitz et al., 2015] in order to study climate impacts of SAI (e.g. on precipitation patterns, monsoons, vegetation, or sea ice cover) and relate the model's results to those of other climate models. Another interesting case to study would be a volcanic eruption during SAI deployment, as the already present aerosol would probably interact with the volcanic sulphate and change its impact considerably compared to an eruption under unperturbed conditions [Laakso et al., 2016]. Instead of prescribing a predefined SAI scenario one could also define a goal for the resulting RF distribution (or for climate variables like temperature and precipitation when using a coupled atmosphere-ocean model) and let the model find a way to achieve this aim with an optimised strategy for SAI, or by combining different SRM techniques (SAI, MCB, or also cirrus cloud thinning). Of course, the new model could also be used for studies not related to geoengineering, but to the impact of volcanic eruptions. In this context, there also exist model intercomparison projects like VolMIP [Zanchettin et al., 2016] and ISA-MIP [Timmreck et al., 2016] for interactive stratospheric aerosol models, whose predefined scenarios could be simulated with LMDZ-S3A.

Acknowledgements

At the end of this thesis I would like to thank ...

... Olivier Boucher who guided me so intensively over the years of my doctorate, despite the spatial distance that separated us most of the time. This work would not have been possible without all his ideas, critical questions, explanations, and feedback.

... Ulrich Platt who exposed me to the concept of climate engineering in the first place, offered me the opportunity to study it during my doctorate, and supported me through frequent discussions.

... Ulrike Lohmann and Hervé Douville for accepting to review my thesis and Thierry Fouchet and Ulrich Schwarz for being part of the examination committee.

... Slimane Bekki and Yves Balkanski for providing me with their helpful feedback as members of the *comité de thèse*.

... the German Research Foundation (DFG) for funding our project *Limitations of Climate Engineering Efficacy by Different Types of RADiation MANagement* (RADMAN) within the priority programme (SPP) 1689 on climate engineering and for offering opportunities for interdisciplinary exchange through the organisation of retreats and workshops.

... the supercomputing center TGCC for providing computing time under the GENCI projects t2014012201, t2015012201, t2016012201 and t2017012201.

... Tobias Schad, Bernhard Vogel, and Thomas Leisner who worked on the complementary part of our DFG-funded RADMAN project studying marine cloud brightening, for their helpful discussions during the regular project team meetings.

... Gunnar Myhre for performing the radiative kernel calculations presented in Section 5.9.

... the LMDZ and libIGCM development teams, especially Josefine Ghattas for preparing the LMDZORSTRATAER_v6 configuration.

... the members of the Laboratoire de Météorologie Dynamique (LMD) in Paris for their warm welcome and their occasional help during my stay in France, especially Jerónimo Escribano for his help with several programming and organisational issues.

... the members of the Atmosphere and Remote Sensing group at the Institute of Environmental Physics (IUP) in Heidelberg for their pleasant company and the stimulating exchange.

... my family, especially my wife Eszter, for being with me, supporting me, and giving me so much joy over these years.

List of acronyms

AOD	Aerosol optical depth
BDC	Brewer-Dobson circulation
CCN	Cloud condensation nuclei
CCT	Cirrus cloud thinning
CDNC	Cloud droplet number concentration
CE	Climate engineering
CMIP	Coupled Model Intercomparison Project
ECHAM	ECMWF / Hamburg atmospheric general circulation model
ECMWF	European Centre for Medium-Range Weather Forecasts
ERF	Effective radiative forcing
GCM	General circulation model
IPSL	Institut Pierre-Simon Laplace
IRF	Instantaneous radiative forcing
LIDAR	Light detection and ranging
LMDZ	Laboratoire de Météorologie Dynamique zoom model
LW	Longwave (terrestrial radiation)
MCB	Marine cloud brightening
MMR	Mass mixing ratio
MSU	Microwave sounding unit
NEMO	Nucleus for European Modelling of the Ocean
OPC	Optical particle counter
ORCHIDEE	ORganizing Carbon and Hydrology in Dynamic EcosystEms
PM	Particulate matter
QBO	Quasi-biennial oscillation
RCP	Representative Concentration Pathway
REPROBUS	Reactive Processes Ruling the Ozone Budget in the Stratosphere
RF	Radiative forcing
S3A	Sectional stratospheric sulphate aerosol module
SAGE	Stratospheric Aerosol and Gas Experiment
SAI	Stratospheric aerosol injection
SAOD	Stratospheric aerosol optical depth
SST	Sea surface temperature
SW	Shortwave (solar radiation)
TOA	Top of the atmosphere
TTL	Tropical tropopause layer
UTLS	Upper troposphere and lower stratosphere
WACCM	Whole Atmosphere Community Climate Model
WMO	World Meteorological Organisation

Publications

1. **Kleinschmitt, C.**, Boucher, O., Bekki, S., Lott, F., and Platt, U.: The Sectional Stratospheric Sulfate Aerosol module (S3A-v1) within the LMDZ general circulation model: description and evaluation against stratospheric aerosol observations, Geoscientific Model Development, 10, 3359–3378, doi:10.5194/gmd-10-3359-2017, 2017a.
2. **Kleinschmitt, C.**, Boucher, O., and Platt, U.: Sensitivity of the radiative forcing by stratospheric sulfur geoengineering to the amount and strategy of the SO_2 injection studied with the LMDZ-S3A model, Atmospheric Chemistry and Physics Discussions, doi:10.5194/acp-2017-722, in review, 2017b.
3. Boucher, O., **Kleinschmitt, C.**, and Myhre, G.: Quasi-additivity of the radiative effects of marine cloud brightening and stratospheric sulfate aerosol injection, Geophysical Research Letters, in press, 2017.

These three publications are all used in this thesis. Large parts of the text and all the figures of Kleinschmitt et al. [2017a] are included in Chapter 3 and Chapter 4. The same holds for Kleinschmitt et al. [2017b] in Chapter 5. Results from Boucher, Kleinschmitt, and Myhre [2017] are shown and discussed in Section 5.9 and in Chapter 6.

Bibliography

Alterskjær, K., Kristjánsson, J. E., Boucher, O., Muri, H., Niemeier, U., Schmidt, H., Schulz, M., and Timmreck, C.: Sea-salt injections into the low-latitude marine boundary layer: The transient response in three Earth system models, Journal of Geophysical Research: Atmospheres, 118, 12,195–12,206, doi:10.1002/2013JD020432, 2013.

Aquila, V., Oman, L. D., Stolarski, R. S., Colarco, P. R., and Newman, P. A.: Dispersion of the volcanic sulfate cloud from a Mount Pinatubo–like eruption, Journal of Geophysical Research: Atmospheres, 117, D06 216, doi:10.1029/2011JD016968, 2012.

Aquila, V., Garfinkel, C. I., Newman, P., Oman, L., and Waugh, D.: Modifications of the quasi-biennial oscillation by a geoengineering perturbation of the stratospheric aerosol layer, Geophysical Research Letters, 41, 1738–1744, doi:10.1002/2013GL058818, 2014.

Ayers, G. P., Gillett, R. W., and Gras, J. L.: On the vapor pressure of sulfuric acid, Geophysical Research Letters, 7, 433–436, doi:10.1029/GL007i006p00433, 1980.

Bekki, S.: Oxidation of volcanic SO_2: A sink for stratospheric OH and H_2O, Geophysical Research Letters, 22, 913–916, doi:10.1029/95GL00534, 1995.

Bekki, S. and Pyle, J. A.: Two-dimensional assessment of the impact of aircraft sulphur emissions on the stratospheric sulphate aerosol layer, Journal of Geophysical Research: Atmospheres, 97, 15 839–15 847, doi:10.1029/92JD00770, 1992.

Bekki, S. and Pyle, J. A.: Potential impact of combined NOx and SOx emissions from future high speed civil transport aircraft on stratospheric aerosols and ozone, Geophysical Research Letters, 20, 723–726, doi:10.1029/93GL00853, 1993.

Biermann, U. M., Luo, B. P., and Peter, T.: Absorption Spectra and Optical Constants of Binary and Ternary Solutions of H_2SO_4, HNO_3, and H_2O in the Mid Infrared at Atmospheric Temperatures, The Journal of Physical Chemistry A, 104, 783–793, doi:10.1021/jp992349i, 2000.

Bluth, G. J. S., Doiron, S. D., Schnetzler, C. C., Krueger, A. J., and Walter, L. S.: Global tracking of the SO_2 clouds from the June, 1991 Mount Pinatubo eruptions, Geophysical Research Letters, 19, 151–154, doi:10.1029/91GL02792, 1992.

Boucher, O.: Atmospheric Aerosols: Properties and Climate Impacts, Springer Netherlands, Dordrecht, doi:10.1007/978-94-017-9649-1, 2015.

Boucher, O. and Lohmann, U.: The sulfate-CCN-cloud albedo effect, Tellus B: Chemical and Physical Meteorology, 47, 281–300, doi:10.3402/tellusb.v47i3.16048, 1995.

Boucher, O., Schwartz, S. E., Ackerman, T. P., Anderson, T. L., Bergstrom, B., Bonnel, B., Chýlek, P., Dahlback, A., Fouquart, Y., Fu, Q., Halthore, R. N., Haywood, J. M., Iversen, T., Kato, S., Kinne, S., Kirkevåg, A., Knapp, K. R., Lacis, A., Laszlo, I., Mishchenko, M. I., Nemesure, S., Ramaswamy, V., Roberts, D. L., Russell, P., Schlesinger, M. E., Stephens, G. L., Wagener, R., Wang, M., Wong, J., and Yang, F.: Intercomparison of models representing direct shortwave radiative forcing by sulfate aerosols, Journal of Geophysical Research: Atmospheres, 103, 16 979–16 998, doi:10.1029/98JD00997, 1998.

Boucher, O., Randall, D., Artaxo, P., Bretherton, C., Feingold, G., Forster, P., Kerminen, V.-M., Kondo, Y., Liao, H., Lohmann, U., Rasch, P., Satheesh, S., Sherwood, S., Stevens, B., and Zhang, X.: Clouds and Aerosols, in: Climate Change 2013: The Physical Science Basis. Contribution of Working Group I to the Fifth Assessment Report of the Intergovernmental Panel on Climate Change, edited by Stocker, T., Qin, D., Plattner, G.-K., Tignor, M., Allen, S., Boschung, J., Nauels, A., Xia, Y., Bex, V., and Midgley, P., chapter 7, 571–658, Cambridge University Press, Cambridge, United Kingdom and New York, NY, USA, doi:10.1017/CBO9781107415324.016, 2013.

Boucher, O., Kleinschmitt, C., and Myhre, G.: Quasi-additivity of the radiative effects of marine cloud brightening and stratospheric aerosol injection, Geophysical Research Letters, in press, 2017.

Braun, C., Merk, C., Pönitzsch, G., Rehdanz, K., and Schmidt, U.: Public perception of climate engineering and carbon capture and storage in Germany: survey evidence, Climate Policy, 0, 1–14, doi:10.1080/14693062.2017.1304888, 2017.

Budyko, M. I.: Climatic Changes, American Geophysical Union, doi:10.1029/SP010, 1977.

Cao, L., Duan, L., Bala, G., and Caldeira, K.: Simultaneous stabilization of global temperature and precipitation through cocktail geoengineering, Geophysical Research Letters, 44, 7429–7437, doi:10.1002/2017GL074281, 2017.

Chan, T. W. and Mozurkewich, M.: Measurement of the coagulation rate constant for sulfuric acid particles as a function of particle size using tandem differential mobility analysis, Journal of Aerosol Science, 32, 321–339, doi:10.1016/S0021-8502(00)00081-1, 2001.

Chin, M. and Davis, D. D.: A reanalysis of carbonyl sulfide as a source of stratospheric background sulfur aerosol, Journal of Geophysical Research: Atmospheres, 100, 8993–9005, doi:10.1029/95JD00275, 1995.

Cirisan, A., Spichtinger, P., Luo, B. P., Weisenstein, D. K., Wernli, H., Lohmann, U., and Peter, T.: Microphysical and radiative changes in cirrus clouds by geoengineering the stratosphere, Journal of Geophysical Research: Atmospheres, 118, 4533–4548, doi:10.1002/jgrd.50388, 2013.

Collins, M., Knutti, R., Arblaster, J., Dufresne, J.-L., Fichefet, T., Friedlingstein, P., Gao, X., Gutowski, W., Johns, T., Krinner, G., Shongwe, M., Tebaldi, C., Weaver, A., and Wehner, M.: Long-term Climate Change: Projections, Commitments and Irreversibility, in: Climate Change 2013: The Physical Science Basis. Contribution of Working Group I to the Fifth Assessment Report of the Intergovernmental Panel on Climate Change, edited by Stocker, T., Qin, D., Plattner, G.-K., Tignor, M., Allen, S., Boschung, J., Nauels, A., Xia, Y., Bex, V., and Midgley, P., chapter 12, 1029–1136, Cambridge University Press, Cambridge, United Kingdom and New York, NY, USA, doi:10.1017/CBO9781107415324.024, 2013.

Crutzen, P. J.: Albedo enhancement by stratospheric sulfur injections: A contribution to resolve a policy dilemma?, Climatic Change, 77, 211–219, doi:10.1007/s10584-006-9101-y, 2006.

Cziczo, D. J., Thomson, D. S., and Murphy, D. M.: Ablation, Flux, and Atmospheric Implications of Meteors Inferred from Stratospheric Aerosol, Science, 291, 1772–1775, doi:10.1126/science.1057737, 2001.

de la Cámara, A., Lott, F., and Abalos, M.: Climatology of the middle atmosphere in LMDz: Impact of source-related parameterizations of gravity wave drag, Journal of Advances in Modeling Earth Systems, 1507–1525, doi:10.1002/2016MS000753, 2016.

Deshler, T.: A review of global stratospheric aerosol: Measurements, importance, life cycle, and local stratospheric aerosol, Atmospheric Research, 90, 223–232, doi:10.1016/j.atmosres.2008.03.016, 2008.

Deshler, T., Hervig, M. E., Hofmann, D. J., Rosen, J. M., and Liley, J. B.: Thirty years of in situ stratospheric aerosol size distribution measurements from Laramie, Wyoming (41°N), using balloon-borne instruments, Journal of Geophysical Research: Atmospheres, 108, 4167, doi:10.1029/2002JD002514, 2003.

Dessler, A., Ye, H., Wang, T., Schoeberl, M., Oman, L., Douglass, A., Butler, A., Rosenlof, K., Davis, S., and Portmann, R.: Transport of ice into the stratosphere and the humidification of the stratosphere over the 21st century, Geophysical Research Letters, 43, 2323–2329, doi:10.1002/2016GL067991, 2016.

Dessler, A. E.: Clouds and water vapor in the Northern Hemisphere summertime stratosphere, Journal of Geophysical Research: Atmospheres, 114, D00H09, doi:10.1029/2009JD012075, 2009.

Dessler, A. E., Schoeberl, M. R., Wang, T., Davis, S. M., and Rosenlof, K. H.: Stratospheric water vapor feedback, Proceedings of the National Academy of Sciences, 110, 18 087–18 091, doi:10.1073/pnas.1310344110, 2013.

Dhomse, S. S., Emmerson, K. M., Mann, G. W., Bellouin, N., Carslaw, K. S., Chipperfield, M. P., Hommel, R., Abraham, N. L., Telford, P., Braesicke, P., Dalvi, M., Johnson, C. E., O'Connor, F., Morgenstern, O., Pyle, J. A., Deshler, T., Zawodny, J. M., and Thomason,

L. W.: Aerosol microphysics simulations of the Mt. Pinatubo eruption with the UM-UKCA composition-climate model, Atmospheric Chemistry and Physics, 14, 11 221–11 246, doi:10.5194/acp-14-11221-2014, 2014.

Dufresne, J.-L., Foujols, M.-A., Denvil, S., Caubel, A., Marti, O., Aumont, O., Balkanski, Y., Bekki, S., Bellenger, H., Benshila, R., Bony, S., Bopp, L., Braconnot, P., Brockmann, P., Cadule, P., Cheruy, F., Codron, F., Cozic, A., Cugnet, D., de Noblet, N., Duvel, J.-P., Ethé, C., Fairhead, L., Fichefet, T., Flavoni, S., Friedlingstein, P., Grandpeix, J.-Y., Guez, L., Guilyardi, E., Hauglustaine, D., Hourdin, F., Idelkadi, A., Ghattas, J., Joussaume, S., Kageyama, M., Krinner, G., Labetoulle, S., Lahellec, A., Lefebvre, M.-P., Lefevre, F., Levy, C., Li, Z. X., Lloyd, J., Lott, F., Madec, G., Mancip, M., Marchand, M., Masson, S., Meurdesoif, Y., Mignot, J., Musat, I., Parouty, S., Polcher, J., Rio, C., Schulz, M., Swingedouw, D., Szopa, S., Talandier, C., Terray, P., Viovy, N., and Vuichard, N.: Climate change projections using the IPSL-CM5 Earth System Model: from CMIP3 to CMIP5, Climate Dynamics, 40, 2123–2165, doi:10.1007/s00382-012-1636-1, 2013.

Dutton, E. G. and Christy, J. R.: Solar radiative forcing at selected locations and evidence for global lower tropospheric cooling following the eruptions of El Chichón and Pinatubo, Geophysical Research Letters, 19, 2313–2316, doi:10.1029/92GL02495, 1992.

Dykema, J. A., Keith, D. W., Anderson, J. G., and Weisenstein, D.: Stratospheric controlled perturbation experiment: a small-scale experiment to improve understanding of the risks of solar geoengineering, Philosophical Transactions of the Royal Society of London A: Mathematical, Physical and Engineering Sciences, 372, 2031, doi:10.1098/rsta.2014.0059, 2014.

Dykema, J. A., Keith, D. W., and Keutsch, F. N.: Improved aerosol radiative properties as a foundation for solar geoengineering risk assessment, Geophysical Research Letters, 43, 7758–7766, doi:10.1002/2016GL069258, 2016.

English, J. M., Toon, O. B., Mills, M. J., and Yu, F.: Microphysical simulations of new particle formation in the upper troposphere and lower stratosphere, Atmospheric Chemistry and Physics, 11, 9303–9322, doi:10.5194/acp-11-9303-2011, 2011.

English, J. M., Toon, O. B., and Mills, M. J.: Microphysical simulations of sulfur burdens from stratospheric sulfur geoengineering, Atmospheric Chemistry and Physics, 12, 4775–4793, doi:10.5194/acp-12-4775-2012, 2012.

English, J. M., Toon, O. B., and Mills, M. J.: Microphysical simulations of large volcanic eruptions: Pinatubo and Toba, Journal of Geophysical Research: Atmospheres, 118, 1880–1895, doi:10.1002/jgrd.50196, 2013.

Escribano, J., Boucher, O., Chevallier, F., and Huneeus, N.: Subregional inversion of North African dust sources, Journal of Geophysical Research: Atmospheres, 121, 8549–8566, doi:10.1002/2016JD025020, 2016.

Eyring, V., Bony, S., Meehl, G. A., Senior, C. A., Stevens, B., Stouffer, R. J., and Taylor, K. E.: Overview of the Coupled Model Intercomparison Project Phase 6 (CMIP6) experimental design and organization, Geoscientific Model Development, 9, 1937–1958, doi:10.5194/gmd-9-1937-2016, 2016.

Ferraro, A. J., Highwood, E. J., and Charlton-Perez, A. J.: Stratospheric heating by potential geoengineering aerosols, Geophysical Research Letters, 38, L24 706, doi:10.1029/2011GL049761, 2011.

Fiocco, G. and Grams, G.: Observations of the Aerosol Layer at 20 km by Optical Radar, Journal of the Atmospheric Sciences, 21, 323–324, doi:10.1175/1520-0469(1964)021<0323:OOTALA>2.0.CO;2, 1964.

Flato, G., Marotzke, J., Abiodun, B., Braconnot, P., Chou, S., Collins, W., Cox, P., Driouech, F., Emori, S., Eyring, V., Forest, C., Gleckler, P., Guilyardi, E., Jakob, C., Kattsov, V., Reason, C., and Rummukainen, M.: Evaluation of Climate Models, in: Climate Change 2013: The Physical Science Basis. Contribution of Working Group I to the Fifth Assessment Report of the Intergovernmental Panel on Climate Change, edited by Stocker, T., Qin, D., Plattner, G.-K., Tignor, M., Allen, S., Boschung, J., Nauels, A., Xia, Y., Bex, V., and Midgley, P., chapter 9, 741–866, Cambridge University Press, Cambridge, United Kingdom and New York, NY, USA, doi:10.1017/CBO9781107415324.020, 2013.

Fouquart, Y. and Bonnel, B.: Computations of solar heating of the earth's atmosphere-A new parameterization, Beitraege zur Physik der Atmosphaere, 53, 35–62, 1980.

Garcia, R. R., Marsh, D. R., Kinnison, D. E., Boville, B. A., and Sassi, F.: Simulation of secular trends in the middle atmosphere, 1950–2003, Journal of Geophysical Research: Atmospheres, 112, D09 301, doi:10.1029/2006JD007485, 2007.

Gettelman, A., Hegglin, M. I., Son, S.-W., Kim, J., Fujiwara, M., Birner, T., Kremser, S., Rex, M., Añel, J. A., Akiyoshi, H., Austin, J., Bekki, S., Braesike, P., Brühl, C., Butchart, N., Chipperfield, M., Dameris, M., Dhomse, S., Garny, H., Hardiman, S. C., Jöckel, P., Kinnison, D. E., Lamarque, J. F., Mancini, E., Marchand, M., Michou, M., Morgenstern, O., Pawson, S., Pitari, G., Plummer, D., Pyle, J. A., Rozanov, E., Scinocca, J., Shepherd, T. G., Shibata, K., Smale, D., Teyssèdre, H., and Tian, W.: Multimodel assessment of the upper troposphere and lower stratosphere: Tropics and global trends, Journal of Geophysical Research: Atmospheres, 115, D00M08, doi:10.1029/2009JD013638, 2010.

Giauque, W., Hornung, E., Kunzler, J., and Rubin, T.: The thermodynamic properties of aqueous sulfuric acid solutions and hydrates from 15 to 300 K., Journal of the American Chemical Society, 82, 62–70, doi:10.1021/ja01486a014, 1960.

Giorgetta, M. A., Manzini, E., Roeckner, E., Esch, M., and Bengtsson, L.: Climatology and Forcing of the Quasi-Biennial Oscillation in the MAECHAM5 Model, Journal of Climate, 19, 3882–3901, doi:10.1175/JCLI3830.1, 2006.

Gmitro, J. I. and Vermeulen, T.: Vapor-liquid equilibria for aqueous sulfuric acid, AIChE Journal, 10, 740–746, doi:10.1002/aic.690100531, 1964.

Govindasamy, B., Caldeira, K., and Duffy, P.: Geoengineering Earth's radiation balance to mitigate climate change from a quadrupling of CO_2, Global and Planetary Change, 37, 157–168, doi:10.1016/S0921-8181(02)00195-9, 2003.

Hamill, P., Turco, R., Kiang, C., Toon, O., and Whitten, R.: An analysis of various nucleation mechanisms for sulfate particles in the stratosphere, Journal of Aerosol Science, 13, 561–585, doi:10.1016/0021-8502(82)90021-0, 1982.

Haywood, J. M., Jones, A., Clarisse, L., Bourassa, A., Barnes, J., Telford, P., Bellouin, N., Boucher, O., Agnew, P., Clerbaux, C., Coheur, P., Degenstein, D., and Braesicke, P.: Observations of the eruption of the Sarychev volcano and simulations using the HadGEM2 climate model, Journal of Geophysical Research: Atmospheres, 115, D21 212, doi:10.1029/2010JD014447, 2010.

Heckendorn, P., Weisenstein, D., Fueglistaler, S., Luo, B. P., Rozanov, E., Schraner, M., Thomason, L. W., and Peter, T.: The impact of geoengineering aerosols on stratospheric temperature and ozone, Environmental Research Letters, 4, 045 108, doi:10.1088/1748-9326/4/4/045108, 2009.

Hourdin, F. and Armengaud, A.: The Use of Finite-Volume Methods for Atmospheric Advection of Trace Species. Part I: Test of Various Formulations in a General Circulation Model, Monthly Weather Review, 127, 822–837, doi:10.1175/1520-0493(1999)127<0822:TUOFVM>2.0.CO;2, 1999.

Hourdin, F., Musat, I., Bony, S., Braconnot, P., Codron, F., Dufresne, J.-L., Fairhead, L., Filiberti, M.-A., Friedlingstein, P., Grandpeix, J.-Y., Krinner, G., LeVan, P., Li, Z.-X., and Lott, F.: The LMDZ4 general circulation model: climate performance and sensitivity to parametrized physics with emphasis on tropical convection, Climate Dynamics, 27, 787–813, doi:10.1007/s00382-006-0158-0, 2006.

Hourdin, F., Foujols, M.-A., Codron, F., Guemas, V., Dufresne, J.-L., Bony, S., Denvil, S., Guez, L., Lott, F., Ghattas, J., Braconnot, P., Marti, O., Meurdesoif, Y., and Bopp, L.: Impact of the LMDZ atmospheric grid configuration on the climate and sensitivity of the IPSL-CM5A coupled model, Climate Dynamics, 40, 2167–2192, doi:10.1007/s00382-012-1411-3, 2013.

Hummel, J. R., Shettle, E. P., and Longtin, D. R.: A new background stratospheric aerosol model for use in atmospheric radiation models, Tech. rep., DTIC Document, `www.researchgate.net/profile/Eric_Shettle/publication/235105132_A_New_Background_Stratospheric_Aerosol_Model_for_Use_in_Atmospheric_Radiation_Models/links/00b4952618db29470c000000.pdf`, 1988.

IPCC: Climate Change 2013: The Physical Science Basis. Contribution of Working Group I to the Fifth Assessment Report of the Intergovernmental Panel on Climate

Change, Cambridge University Press, Cambridge, United Kingdom and New York, NY, USA, doi:10.1017/CBO9781107415324, 2013.

Irvine, P. J., Kravitz, B., Lawrence, M. G., and Muri, H.: An overview of the Earth system science of solar geoengineering, Wiley Interdisciplinary Reviews: Climate Change, 7, 815–833, doi:10.1002/wcc.423, 2016.

Jacobson, M. Z., Turco, R. P., Jensen, E. J., and Toon, O. B.: Modeling coagulation among particles of different composition and size, Atmospheric Environment, 28, 1327–1338, doi:10.1016/1352-2310(94)90280-1, 1994.

Jones, A., Haywood, J., and Boucher, O.: A comparison of the climate impacts of geoengineering by stratospheric SO_2 injection and by brightening of marine stratocumulus cloud, Atmospheric Science Letters, 12, 176–183, doi:10.1002/asl.291, 2011.

Jones, A., Haywood, J. M., Alterskjær, K., Boucher, O., Cole, J. N. S., Curry, C. L., Irvine, P. J., Ji, D., Kravitz, B., Kristjánsson, J. E., Moore, J. C., Niemeier, U., Robock, A., Schmidt, H., Singh, B., Tilmes, S., Watanabe, S., and Yoon, J.-H.: The impact of abrupt suspension of solar radiation management (termination effect) in experiment G2 of the Geoengineering Model Intercomparison Project (GeoMIP), Journal of Geophysical Research: Atmospheres, 118, 9743–9752, doi:10.1002/jgrd.50762, 2013.

Jones, A. C., Haywood, J. M., and Jones, A.: Climatic impacts of stratospheric geoengineering with sulfate, black carbon and titania injection, Atmospheric Chemistry and Physics, 16, 2843–2862, doi:10.5194/acp-16-2843-2016, 2016.

Junge, C. E., Chagnon, C. W., and Manson, J. E.: Stratospheric aerosols, Journal of Meteorology, 18, 81–108, doi:10.1175/1520-0469(1961)018<0081:SA>2.0.CO;2, 1961.

Jäger, H.: Long-term record of lidar observations of the stratospheric aerosol layer at Garmisch-Partenkirchen, Journal of Geophysical Research: Atmospheres, 110, D08 106, doi:10.1029/2004JD005506, 2005.

Kawatani, Y. and Hamilton, K.: Weakened stratospheric quasibiennial oscillation driven by increased tropical mean upwelling, Nature, 497, 478–481, doi:10.1038/nature12140, 2013.

Keith, D. W., Weisenstein, D. K., Dykema, J. A., and Keutsch, F. N.: Stratospheric solar geoengineering without ozone loss, Proceedings of the National Academy of Sciences, 113, 14 910–14 914, doi:10.1073/pnas.1615572113, 2016.

Kleinschmitt, C., Boucher, O., Bekki, S., Lott, F., and Platt, U.: The Sectional Stratospheric Sulfate Aerosol module (S3A-v1) within the LMDZ general circulation model: description and evaluation against stratospheric aerosol observations, Geoscientific Model Development, 10, 3359–3378, doi:10.5194/gmd-10-3359-2017, 2017a.

Kleinschmitt, C., Boucher, O., and Platt, U.: Sensitivity of the radiative forcing by stratospheric sulfur geoengineering to the amount and strategy of the SO_2 injection studied with the LMDZ-S3A model, Atmospheric Chemistry and Physics Discussions, doi:10.5194/acp-2017-722, in review, 2017b.

Kokkola, H., Hommel, R., Kazil, J., Niemeier, U., Partanen, A.-I., Feichter, J., and Timmreck, C.: Aerosol microphysics modules in the framework of the ECHAM5 climate model – intercomparison under stratospheric conditions, Geoscientific Model Development, 2, 97–112, doi:10.5194/gmd-2-97-2009, 2009.

Kovilakam, M. and Deshler, T.: On the accuracy of stratospheric aerosol extinction derived from in situ size distribution measurements and surface area density derived from remote SAGE II and HALOE extinction measurements, Journal of Geophysical Research: Atmospheres, 120, 8426–8447, doi:10.1002/2015JD023303, 2015.

Kravitz, B., Robock, A., Oman, L., Stenchikov, G., and Marquardt, A. B.: Sulfuric acid deposition from stratospheric geoengineering with sulfate aerosols, Journal of Geophysical Research: Atmospheres, 114, D14 109, doi:10.1029/2009JD011918, 2009.

Kravitz, B., Robock, A., Boucher, O., Schmidt, H., Taylor, K. E., Stenchikov, G., and Schulz, M.: The Geoengineering Model Intercomparison Project (GeoMIP), Atmospheric Science Letters, 12, 162–167, doi:10.1002/asl.316, 2011.

Kravitz, B., Caldeira, K., Boucher, O., Robock, A., Rasch, P. J., Alterskjær, K., Karam, D. B., Cole, J. N. S., Curry, C. L., Haywood, J. M., Irvine, P. J., Ji, D., Jones, A., Kristjánsson, J. E., Lunt, D. J., Moore, J. C., Niemeier, U., Schmidt, H., Schulz, M., Singh, B., Tilmes, S., Watanabe, S., Yang, S., and Yoon, J.-H.: Climate model response from the Geoengineering Model Intercomparison Project (GeoMIP), Journal of Geophysical Research: Atmospheres, 118, 8320–8332, doi:10.1002/jgrd.50646, 2013a.

Kravitz, B., Forster, P. M., Jones, A., Robock, A., Alterskjær, K., Boucher, O., Jenkins, A. K. L., Korhonen, H., Kristjánsson, J. E., Muri, H., Niemeier, U., Partanen, A.-I., Rasch, P. J., Wang, H., and Watanabe, S.: Sea spray geoengineering experiments in the geoengineering model intercomparison project (GeoMIP): Experimental design and preliminary results, Journal of Geophysical Research: Atmospheres, 118, 11,175–11,186, doi:10.1002/jgrd.50856, 2013b.

Kravitz, B., MacMartin, D. G., Robock, A., Rasch, P. J., Ricke, K. L., Cole, J. N. S., Curry, C. L., Irvine, P. J., Ji, D., Keith, D. W., Kristjánsson, J. E., Moore, J. C., Muri, H., Singh, B., Tilmes, S., Watanabe, S., Yang, S., and Yoon, J.-H.: A multi-model assessment of regional climate disparities caused by solar geoengineering, Environmental Research Letters, 9, 074 013, doi:10.1088/1748-9326/9/7/074013, 2014.

Kravitz, B., Robock, A., Tilmes, S., Boucher, O., English, J. M., Irvine, P. J., Jones, A., Lawrence, M. G., MacCracken, M., Muri, H., Moore, J. C., Niemeier, U., Phipps, S. J., Sillmann, J., Storelvmo, T., Wang, H., and Watanabe, S.: The Geoengineering Model Intercomparison Project Phase 6 (GeoMIP6): simulation design and preliminary

results, Geoscientific Model Development, 8, 3379–3392, doi:10.5194/gmd-8-3379-2015, 2015.

Kravitz, B., MacMartin, D. G., Wang, H., and Rasch, P. J.: Geoengineering as a design problem, Earth System Dynamics, 7, 469–497, doi:10.5194/esd-7-469-2016, 2016.

Kremser, S., Thomason, L. W., von Hobe, M., Hermann, M., Deshler, T., Timmreck, C., Toohey, M., Stenke, A., Schwarz, J. P., Weigel, R., Fueglistaler, S., Prata, F. J., Vernier, J.-P., Schlager, H., Barnes, J. E., Antuña-Marrero, J.-C., Fairlie, D., Palm, M., Mahieu, E., Notholt, J., Rex, M., Bingen, C., Vanhellemont, F., Bourassa, A., Plane, J. M. C., Klocke, D., Carn, S. A., Clarisse, L., Trickl, T., Neely, R., James, A. D., Rieger, L., Wilson, J. C., and Meland, B.: Stratospheric aerosol—Observations, processes, and impact on climate, Reviews of Geophysics, 54, 278–335, doi:10.1002/2015RG000511, 2016.

Krinner, G., Viovy, N., de Noblet-Ducoudré, N., Ogée, J., Polcher, J., Friedlingstein, P., Ciais, P., Sitch, S., and Prentice, I. C.: A dynamic global vegetation model for studies of the coupled atmosphere-biosphere system, Global Biogeochemical Cycles, 19, GB1015, doi:10.1029/2003GB002199, 2005.

Kuebbeler, M., Lohmann, U., and Feichter, J.: Effects of stratospheric sulfate aerosol geo-engineering on cirrus clouds, Geophysical Research Letters, 39, L23 803, doi:10.1029/2012GL053797, 2012.

Kuylenstierna, J. C. I., Rodhe, H., Cinderby, S., and Hicks, K.: Acidification in Developing Countries: Ecosystem Sensitivity and the Critical Load Approach on a Global Scale, Ambio, 30, 20–28, doi:10.1579/0044-7447-30.1.20, 2001.

Laakso, A., Kokkola, H., Partanen, A.-I., Niemeier, U., Timmreck, C., Lehtinen, K. E. J., Hakkarainen, H., and Korhonen, H.: Radiative and climate impacts of a large volcanic eruption during stratospheric sulfur geoengineering, Atmospheric Chemistry and Physics, 16, 305–323, doi:10.5194/acp-16-305-2016, 2016.

Laakso, A., Korhonen, H., Romakkaniemi, S., and Kokkola, H.: Radiative and climate effects of stratospheric sulfur geoengineering using seasonally varying injection areas, Atmospheric Chemistry and Physics, 17, 6957–6974, doi:10.5194/acp-17-6957-2017, 2017.

Latham, J.: Control of global warming?, Nature, 347, 339–340, doi:10.1038/347339b0, 1990.

Le Quéré, C., Andrew, R. M., Canadell, J. G., Sitch, S., Korsbakken, J. I., Peters, G. P., Manning, A. C., Boden, T. A., Tans, P. P., Houghton, R. A., Keeling, R. F., Alin, S., Andrews, O. D., Anthoni, P., Barbero, L., Bopp, L., Chevallier, F., Chini, L. P., Ciais, P., Currie, K., Delire, C., Doney, S. C., Friedlingstein, P., Gkritzalis, T., Harris, I., Hauck, J., Haverd, V., Hoppema, M., Klein Goldewijk, K., Jain, A. K., Kato, E., Körtzinger, A., Landschützer, P., Lefèvre, N., Lenton, A., Lienert, S., Lombardozzi, D., Melton, J. R.,

Metzl, N., Millero, F., Monteiro, P. M. S., Munro, D. R., Nabel, J. E. M. S., Nakaoka, S.-I., O'Brien, K., Olsen, A., Omar, A. M., Ono, T., Pierrot, D., Poulter, B., Rödenbeck, C., Salisbury, J., Schuster, U., Schwinger, J., Séférian, R., Skjelvan, I., Stocker, B. D., Sutton, A. J., Takahashi, T., Tian, H., Tilbrook, B., van der Laan-Luijkx, I. T., van der Werf, G. R., Viovy, N., Walker, A. P., Wiltshire, A. J., and Zaehle, S.: Global Carbon Budget 2016, Earth System Science Data, 8, 605–649, doi:10.5194/essd-8-605-2016, 2016.

Lefèvre, F., Brasseur, G. P., Folkins, I., Smith, A. K., and Simon, P.: Chemistry of the 1991–1992 stratospheric winter: Three-dimensional model simulations, Journal of Geophysical Research: Atmospheres, 99, 8183–8195, doi:10.1029/93JD03476, 1994.

Lefèvre, F., Figarol, F., Carslaw, K. S., and Peter, T.: The 1997 Arctic Ozone depletion quantified from three-dimensional model simulations, Geophysical Research Letters, 25, 2425–2428, doi:10.1029/98GL51812, 1998.

Lelieveld, J., Evans, J. S., Fnais, M., Giannadaki, D., and Pozzer, A.: The contribution of outdoor air pollution sources to premature mortality on a global scale, Nature, 525, 367–371, doi:10.1038/nature15371, 2015.

Lohmann, U. and Gasparini, B.: A cirrus cloud climate dial?, Science, 357, 248–249, doi:10.1126/science.aan3325, 2017.

Lott, F. and Guez, L.: A stochastic parameterization of the gravity waves due to convection and its impact on the equatorial stratosphere, Journal of Geophysical Research: Atmospheres, 118, 8897–8909, doi:10.1002/jgrd.50705, 2013.

Lott, F., Denvil, S., Butchart, N., Cagnazzo, C., Giorgetta, M. A., Hardiman, S. C., Manzini, E., Krismer, T., Duvel, J.-P., Maury, P., Scinocca, J. F., Watanabe, S., and Yukimoto, S.: Kelvin and Rossby-gravity wave packets in the lower stratosphere of some high-top CMIP5 models, Journal of Geophysical Research: Atmospheres, 119, 2156–2173, doi:10.1002/2013JD020797, 2014.

MacMartin, D. G., Kravitz, B., Long, J. C. S., and Rasch, P. J.: Geoengineering with stratospheric aerosols: What do we not know after a decade of research?, Earth's Future, 4, 543–548, doi:10.1002/2016EF000418, 2016.

Madec, G.: NEMO ocean engine, Note du Pôle de modélisation, Institut Pierre-Simon Laplace (IPSL), France, No 27, ISSN No 1288-1619, `www.nemo-ocean.eu/wp-content/uploads/NEMO_book.pdf`, 2008.

Malavelle, F. F., Haywood, J. M., Jones, A., Gettelman, A., Clarisse, L., Bauduin, S., Allan, R. P., Karset, I. H. H., Kristjánsson, J. E., Oreopoulos, L., Cho, N., Lee, D., Bellouin, N., Boucher, O., Grosvenor, D. P., Carslaw, K. S., Dhomse, S., Mann, G. W., Schmidt, A., Coe, H., Hartley, M. E., Dalvi, M., Hill, A. A., Johnson, B. T., Johnson, C. E., Knight, J. R., O'Connor, F. M., Partridge, D. G., Stier, P., Myhre, G., Platnick, S., Stephens, G. L.,

Takahashi, H., and Thordarson, T.: Strong constraints on aerosol–cloud interactions from volcanic eruptions, Nature, 546, 485–491, doi:10.1038/nature22974, 2017.

Mann, G. W., Carslaw, K. S., Spracklen, D. V., Ridley, D. A., Manktelow, P. T., Chipperfield, M. P., Pickering, S. J., and Johnson, C. E.: Description and evaluation of GLOMAP-mode: a modal global aerosol microphysics model for the UKCA composition-climate model, Geoscientific Model Development, 3, 519–551, doi:10.5194/gmd-3-519-2010, 2010.

McClatchey, R., Bolle, H., Kondratyev, K. Y., Joseph, J., McCormick, M., Raschke, E., Pollack, J., Spänkuch, D., and Mateer, C.: A preliminary cloudless standard atmosphere for radiation computation, World Climate Program, NCAR, Boulder, Colorado, USA, Report, `http://library.wmo.int/pmb_ged/wmo-td_24_en.pdf`, 1984.

McClellan, J., Keith, D. W., and Apt, J.: Cost analysis of stratospheric albedo modification delivery systems, Environmental Research Letters, 7, 034 019, doi:10.1088/1748-9326/7/3/034019, 2012.

McCormick, M.: Sage II: An overview, Advances in Space Research, 7, 219–226, doi:10.1016/0273-1177(87)90151-7, 1987.

Mills, M. J., Toon, O. B., and Solomon, S.: A 2D microphysical model of the polar stratospheric CN layer, Geophysical Research Letters, 26, 1133–1136, doi:10.1029/1999GL900187, 1999.

Mills, M. J., Schmidt, A., Easter, R., Solomon, S., Kinnison, D. E., Ghan, S. J., Neely, R. R., Marsh, D. R., Conley, A., Bardeen, C. G., and Gettelman, A.: Global volcanic aerosol properties derived from emissions, 1990–2014, using CESM1(WACCM), Journal of Geophysical Research: Atmospheres, 121, 2332–2348, doi:10.1002/2015JD024290, 2016.

Mitchell, D. L. and Finnegan, W.: Modification of cirrus clouds to reduce global warming, Environmental Research Letters, 4, 045 102, doi:10.1088/1748-9326/4/4/045102, 2009.

Mlawer, E. J., Taubman, S. J., Brown, P. D., Iacono, M. J., and Clough, S. A.: Radiative transfer for inhomogeneous atmospheres: RRTM, a validated correlated-k model for the longwave, Journal of Geophysical Research: Atmospheres, 102, 16 663–16 682, doi:10.1029/97JD00237, 1997.

Murphy, D. M., Cziczo, D. J., Hudson, P. K., and Thomson, D. S.: Carbonaceous material in aerosol particles in the lower stratosphere and tropopause region, Journal of Geophysical Research: Atmospheres, 112, D04 203, doi:10.1029/2006JD007297, 2007.

Myhre, G., Shine, K., Rädel, G., Gauss, M., Isaksen, I., Tang, Q., Prather, M., Williams, J., van Velthoven, P., Dessens, O., Koffi, B., Szopa, S., Hoor, P., Grewe, V., Borken-Kleefeld, J., Berntsen, T., and Fuglestvedt, J.: Radiative forcing due to changes in

ozone and methane caused by the transport sector, Atmospheric Environment, 45, 387–394, doi:10.1016/j.atmosenv.2010.10.001, 2011.

Myhre, G., Shindell, D., Bréon, F.-M., Collins, W., Fuglestvedt, J., Huang, J., Koch, D., Lamarque, J.-F., Lee, D., Mendoza, B., Nakajima, T., Robock, A., Stephens, G., Takemura, T., and Zhang, H.: Anthropogenic and Natural Radiative Forcing, in: Climate Change 2013: The Physical Science Basis. Contribution of Working Group I to the Fifth Assessment Report of the Intergovernmental Panel on Climate Change, edited by Stocker, T., Qin, D., Plattner, G.-K., Tignor, M., Allen, S., Boschung, J., Nauels, A., Xia, Y., Bex, V., and Midgley, P., chapter 8, 659–740, Cambridge University Press, Cambridge, United Kingdom and New York, NY, USA, doi:10.1017/CBO9781107415324.018, 2013.

Niemeier, U. and Schmidt, H.: Changing transport processes in the stratosphere by radiative heating of sulfate aerosols, Atmospheric Chemistry and Physics Discussions, 2017, 1–24, doi:10.5194/acp-2017-470, 2017.

Niemeier, U. and Timmreck, C.: What is the limit of climate engineering by stratospheric injection of SO_2?, Atmospheric Chemistry and Physics, 15, 9129–9141, doi:10.5194/acp-15-9129-2015, 2015.

Niemeier, U., Schmidt, H., and Timmreck, C.: The dependency of geoengineered sulfate aerosol on the emission strategy, Atmospheric Science Letters, 12, 189–194, doi:10.1002/asl.304, 2011.

Niemeier, U., Schmidt, H., Alterskjær, K., and Kristjánsson, J. E.: Solar irradiance reduction via climate engineering: Impact of different techniques on the energy balance and the hydrological cycle, Journal of Geophysical Research: Atmospheres, 118, 11,905–11,917, doi:10.1002/2013JD020445, 2013.

Oman, L., Robock, A., Stenchikov, G. L., Thordarson, T., Koch, D., Shindell, D. T., and Gao, C.: Modeling the distribution of the volcanic aerosol cloud from the 1783–1784 Laki eruption, Journal of Geophysical Research: Atmospheres, 111, D12 209, doi:10.1029/2005JD006899, 2006.

Palmer, K. F. and Williams, D.: Optical Constants of Sulfuric Acid; Application to the Clouds of Venus?, Applied Optics, 14, 208–219, doi:10.1364/AO.14.000208, 1975.

Partanen, A. I., Laakso, A., Schmidt, A., Kokkola, H., Kuokkanen, T., Pietikäinen, J.-P., Kerminen, V.-M., Lehtinen, K. E. J., Laakso, L., and Korhonen, H.: Climate and air quality trade-offs in altering ship fuel sulfur content, Atmospheric Chemistry and Physics, 13, 12 059–12 071, doi:10.5194/acp-13-12059-2013, 2013.

Pierce, J. R., Weisenstein, D. K., Heckendorn, P., Peter, T., and Keith, D. W.: Efficient formation of stratospheric aerosol for climate engineering by emission of condensible vapor from aircraft, Geophysical Research Letters, 37, L18 805, doi:10.1029/2010GL043975, 2010.

Pinto, J. P., Turco, R. P., and Toon, O. B.: Self-limiting physical and chemical effects in volcanic eruption clouds, Journal of Geophysical Research: Atmospheres, 94, 11 165–11 174, doi:10.1029/JD094iD08p11165, 1989.

Pitari, G., Mancini, E., Rizi, V., and Shindell, D. T.: Impact of Future Climate and Emission Changes on Stratospheric Aerosols and Ozone, Journal of the Atmospheric Sciences, 59, 414–440, doi:10.1175/1520-0469(2002)059<0414:IOFCAE>2.0.CO;2, 2002.

Pitari, G., Aquila, V., Kravitz, B., Robock, A., Watanabe, S., Cionni, I., Luca, N. D., Genova, G. D., Mancini, E., and Tilmes, S.: Stratospheric ozone response to sulfate geoengineering: Results from the Geoengineering Model Intercomparison Project (GeoMIP), Journal of Geophysical Research: Atmospheres, 119, 2629–2653, doi:10.1002/2013JD020566, 2014.

Preston, C. J.: Ethics and geoengineering: reviewing the moral issues raised by solar radiation management and carbon dioxide removal, Wiley Interdisciplinary Reviews: Climate Change, 4, 23–37, doi:10.1002/wcc.198, 2013.

Pruppacher, H. R. and Klett, J. D.: Microphysics of Clouds and Precipitation, Springer, Dordrecht, doi:10.1007/978-0-306-48100-0, 2010.

Rampino, M. R. and Self, S.: Historic eruptions of Tambora (1815), Krakatau (1883), and Agung (1963), their stratospheric aerosols, and climatic impact, Quaternary Research, 18, 127–143, doi:10.1016/0033-5894(82)90065-5, 1982.

Randel, W. J., Wu, F., Russell, J. M., Waters, J. W., and Froidevaux, L.: Ozone and temperature changes in the stratosphere following the eruption of Mount Pinatubo, Journal of Geophysical Research: Atmospheres, 100, 16 753–16 764, doi:10.1029/95JD01001, 1995.

Read, W. G., Froidevaux, L., and Waters, J. W.: Microwave limb sounder measurement of stratospheric SO_2 from the Mt. Pinatubo Volcano, Geophysical Research Letters, 20, 1299–1302, doi:10.1029/93GL00831, 1993.

Reichler, T., Dameris, M., and Sausen, R.: Determining the tropopause height from gridded data, Geophysical Research Letters, 30, 2042, doi:10.1029/2003GL018240, 2003.

Revell, L., Stenke, A., Luo, B., Kremser, S., Rozanov, E., Sukhodolov, T., and Peter, T.: Chemistry-climate model simulations of the Mt. Pinatubo eruption using CCMI and CMIP6 stratospheric aerosol data, Atmospheric Chemistry and Physics Discussions, doi:10.5194/acp-2017-633, in press, 2017.

Revell, L. E., Stenke, A., Rozanov, E., Ball, W., Lossow, S., and Peter, T.: The role of methane in projections of 21st century stratospheric water vapour, Atmospheric Chemistry and Physics, 16, 13 067–13 080, doi:10.5194/acp-16-13067-2016, 2016.

Riahi, K., van Vuuren, D. P., Kriegler, E., Edmonds, J., O'Neill, B. C., Fujimori, S., Bauer, N., Calvin, K., Dellink, R., Fricko, O., Lutz, W., Popp, A., Cuaresma, J. C., KC, S., Leimbach, M., Jiang, L., Kram, T., Rao, S., Emmerling, J., Ebi, K., Hasegawa, T., Havlik, P., Humpenöder, F., Silva, L. A. D., Smith, S., Stehfest, E., Bosetti, V., Eom, J., Gernaat, D., Masui, T., Rogelj, J., Strefler, J., Drouet, L., Krey, V., Luderer, G., Harmsen, M., Takahashi, K., Baumstark, L., Doelman, J. C., Kainuma, M., Klimont, Z., Marangoni, G., Lotze-Campen, H., Obersteiner, M., Tabeau, A., and Tavoni, M.: The Shared Socioeconomic Pathways and their energy, land use, and greenhouse gas emissions implications: An overview, Global Environmental Change, 42, 153–168, doi:10.1016/j.gloenvcha.2016.05.009, 2017.

Ricke, K. L., Morgan, M. G., and Allen, M. R.: Regional climate response to solar-radiation management, Nature Geoscience, 3, 537–541, doi:10.1038/ngeo915, 2010.

Ridley, D. A., Solomon, S., Barnes, J. E., Burlakov, V. D., Deshler, T., Dolgii, S. I., Herber, A. B., Nagai, T., Neely, R. R., Nevzorov, A. V., Ritter, C., Sakai, T., Santer, B. D., Sato, M., Schmidt, A., Uchino, O., and Vernier, J. P.: Total volcanic stratospheric aerosol optical depths and implications for global climate change, Geophysical Research Letters, 41, 7763–7769, doi:10.1002/2014GL061541, 2014.

Salter, S., Sortino, G., and Latham, J.: Sea-going hardware for the cloud albedo method of reversing global warming, Philosophical Transactions of the Royal Society of London A, 366, 3989–4006, doi:10.1098/rsta.2008.0136, 2008.

Santer, B. D., Wehner, M. F., Wigley, T. M. L., Sausen, R., Meehl, G. A., Taylor, K. E., Ammann, C., Arblaster, J., Washington, W. M., Boyle, J. S., and Brüggemann, W.: Contributions of Anthropogenic and Natural Forcing to Recent Tropopause Height Changes, Science, 301, 479–483, doi:10.1126/science.1084123, 2003.

Sato, M.: Forcings in GISS Climate Model: Stratospheric Aerosol Optical Thickness, `http://data.giss.nasa.gov/modelforce/strataer/`, 2012.

Schulz, M., Textor, C., Kinne, S., Balkanski, Y., Bauer, S., Berntsen, T., Berglen, T., Boucher, O., Dentener, F., Guibert, S., Isaksen, I. S. A., Iversen, T., Koch, D., Kirkevåg, A., Liu, X., Montanaro, V., Myhre, G., Penner, J. E., Pitari, G., Reddy, S., Seland, Ø., Stier, P., and Takemura, T.: Radiative forcing by aerosols as derived from the AeroCom present-day and pre-industrial simulations, Atmospheric Chemistry and Physics, 6, 5225–5246, doi:10.5194/acp-6-5225-2006, 2006.

Schäfer, S., Lawrence, M., Stelzer, H., Born, W., Low, S., Aaheim, A., Adriázola, P., Betz, G., Boucher, O., Carius, A., Devine-Right, P., Gullberg, A. T., Haszeldine, S., Haywood, J., Houghton, K., Ibarrola, R., Irvine, P., Kristjansson, J.-E., Lenton, T., Link, J. S. A., Maas, A., Meyer, L., Muri, H., Oschlies, A., Proelß, A., Rayner, T., Rickels, W., Ruthner, L., Scheffran, J., Schmidt, H., Schulz, M., Scott, V., Shackley, S., Tänzler, D., Watson, M., and Vaughan, N.: The European Transdisciplinary Assessment of Climate Engineering (EuTRACE): Removing Greenhouse Gases from

the Atmosphere and Reflecting Sunlight away from Earth, www.eutrace.org, funded by the European Union's Seventh Framework Programme under Grant Agreement 306993, 2015.

Seinfeld, J. H. and Pandis, S. N.: Atmospheric chemistry and physics: from air pollution to climate change, John Wiley & Sons, Hoboken, NJ, USA, 2006.

Seitz, R.: Bright water: hydrosols, water conservation and climate change, Climatic Change, 105, 365–381, doi:10.1007/s10584-010-9965-8, 2011.

Sekiya, T., Sudo, K., and Nagai, T.: Evolution of stratospheric sulfate aerosol from the 1991 Pinatubo eruption: Roles of aerosol microphysical processes, Journal of Geophysical Research: Atmospheres, 121, 2911–2938, doi:10.1002/2015JD024313, 2016.

Sheng, J.-X., Weisenstein, D. K., Luo, B.-P., Rozanov, E., Stenke, A., Anet, J., Bingemer, H., and Peter, T.: Global atmospheric sulfur budget under volcanically quiescent conditions: Aerosol-chemistry-climate model predictions and validation, Journal of Geophysical Research: Atmospheres, 120, 256–276, doi:10.1002/2014JD021985, 2015.

Sherwood, S. C., Bony, S., Boucher, O., Bretherton, C., Forster, P. M., Gregory, J. M., and Stevens, B.: Adjustments in the forcing-feedback framework for understanding climate change, Bulletin of the American Meteorological Society, 96, 217–228, doi:10.1175/BAMS-D-13-00167.1, 2015.

Soden, B. J., Wetherald, R. T., Stenchikov, G. L., and Robock, A.: Global Cooling After the Eruption of Mount Pinatubo: A Test of Climate Feedback by Water Vapor, Science, 296, 727–730, doi:10.1126/science.296.5568.727, 2002.

Soden, B. J., Held, I. M., Colman, R., Shell, K. M., Kiehl, J. T., and Shields, C. A.: Quantifying Climate Feedbacks Using Radiative Kernels, Journal of Climate, 21, 3504–3520, doi:10.1175/2007JCLI2110.1, 2008.

Spencer, R. W. and Christy, J. R.: Precision Lower Stratospheric Temperature Monitoring with the MSU: Technique, Validation, and Results 1979–1991, Journal of Climate, 6, 1194–1204, doi:10.1175/1520-0442(1993)006<1194:PLSTMW>2.0.CO;2, 1993.

Steele, H. M. and Hamill, P.: Effects of temperature and humidity on the growth and optical properties of sulphuric acid—water droplets in the stratosphere, Journal of Aerosol Science, 12, 517–528, doi:10.1016/0021-8502(81)90054-9, 1981.

Stier, P., Feichter, J., Kinne, S., Kloster, S., Vignati, E., Wilson, J., Ganzeveld, L., Tegen, I., Werner, M., Balkanski, Y., Schulz, M., Boucher, O., Minikin, A., and Petzold, A.: The aerosol-climate model ECHAM5-HAM, Atmospheric Chemistry and Physics, 5, 1125–1156, doi:10.5194/acp-5-1125-2005, 2005.

Tabazadeh, A., Toon, O. B., Clegg, S. L., and Hamill, P.: A new parameterization of H_2SO_4/H_2O aerosol composition: Atmospheric implications, Geophysical Research Letters, 24, 1931–1934, doi:10.1029/97GL01879, 1997.

Thomason, L. and Peter, T.: SPARC Assessment of Stratospheric Aerosol Properties (ASAP), Tech. rep., SPARC, `www.sparc-climate.org/publications/sparc-reports/`, 2006.

Thomason, L. W., Burton, S. P., Luo, B.-P., and Peter, T.: SAGE II measurements of stratospheric aerosol properties at non-volcanic levels, Atmospheric Chemistry and Physics, 8, 983–995, doi:10.5194/acp-8-983-2008, 2008.

Tilmes, S., Müller, R., and Salawitch, R.: The Sensitivity of Polar Ozone Depletion to Proposed Geoengineering Schemes, Science, 320, 1201–1204, doi:10.1126/science.1153966, 2008.

Tilmes, S., Garcia, R. R., Kinnison, D. E., Gettelman, A., and Rasch, P. J.: Impact of geoengineered aerosols on the troposphere and stratosphere, Journal of Geophysical Research: Atmospheres, 114, D12 305, doi:10.1029/2008JD011420, 2009.

Timmreck, C.: Three-dimensional simulation of stratospheric background aerosol: First results of a multiannual general circulation model simulation, Journal of Geophysical Research: Atmospheres, 106, 28 313–28 332, doi:10.1029/2001JD000765, 2001.

Timmreck, C., Mann, G., Aquila, V., Bruehl, C., Chin, M., Dohmse, S., English, J., Lee, L., Mills, M., Hommel, R., Neely, R., Schmidt, A., Sheng, J., Toohey, M., and Weisenstein, D.: ISA-MIP: A co-ordinated intercomparison of Interactive Stratospheric Aerosol models, vol. 18 of *Geophysical Research Abstracts*, Vienna, EGU General Assembly, `http://meetingorganizer.copernicus.org/EGU2016/EGU2016-13766.pdf`, 2016.

Tompkins, A. M.: A revised cloud scheme to reduce the sensitivity to vertical resolution, ECMWF Research Department Memorandum, 2005.

Toon, O. B., Turco, R. P., Westphal, D., Malone, R., and Liu, M.: A Multidimensional Model for Aerosols: Description of Computational Analogs, Journal of the Atmospheric Sciences, 45, 2123–2144, doi:10.1175/1520-0469(1988)045<2123:AMMFAD>2.0.CO;2, 1988.

Trepte, C. R. and Hitchman, M. H.: Tropical stratospheric circulation deduced from satellite aerosol data, Nature, 355, 626–628, doi:10.1038/355626a0, 1992.

Turco, R. P., Hamill, P., Toon, O. B., Whitten, R. C., and Kiang, C. S.: A One-Dimensional Model Describing Aerosol Formation and Evolution in the Stratosphere: I. Physical Processes and Mathematical Analogs, Journal of the Atmospheric Sciences, 36, 699–717, doi:10.1175/1520-0469(1979)036<0699:AODMDA>2.0.CO;2, 1979.

van Donkelaar, A., Martin, R. V., Brauer, M., Hsu, N. C., Kahn, R. A., Levy, R. C., Lyapustin, A., Sayer, A. M., and Winker, D. M.: Global Estimates of Fine Particulate Matter using a Combined Geophysical-Statistical Method with Information from Satellites, Models, and Monitors, Environmental Science & Technology, 50, 3762–3772, doi:10.1021/acs.est.5b05833, 2016.

Vehkamäki, H., Kulmala, M., Napari, I., Lehtinen, K. E. J., Timmreck, C., Noppel, M., and Laaksonen, A.: An improved parameterization for sulfuric acid–water nucleation rates for tropospheric and stratospheric conditions, Journal of Geophysical Research: Atmospheres, 107, 4622, doi:10.1029/2002JD002184, 2002.

Vernier, J. P., Pommereau, J. P., Garnier, A., Pelon, J., Larsen, N., Nielsen, J., Christensen, T., Cairo, F., Thomason, L. W., Leblanc, T., and McDermid, I. S.: Tropical stratospheric aerosol layer from CALIPSO lidar observations, Journal of Geophysical Research: Atmospheres, 114, D00H10, doi:10.1029/2009JD011946, 2009.

Vernier, J.-P., Thomason, L. W., Pommereau, J.-P., Bourassa, A., Pelon, J., Garnier, A., Hauchecorne, A., Blanot, L., Trepte, C., Degenstein, D., and Vargas, F.: Major influence of tropical volcanic eruptions on the stratospheric aerosol layer during the last decade, Geophysical Research Letters, 38, L12 807, doi:10.1029/2011GL047563, 2011.

Vignati, E., Wilson, J., and Stier, P.: M7: An efficient size-resolved aerosol microphysics module for large-scale aerosol transport models, Journal of Geophysical Research: Atmospheres, 109, D22 202, doi:10.1029/2003JD004485, 2004.

Visioni, D., Pitari, G., and Aquila, V.: Sulfate geoengineering: a review of the factors controlling the needed injection of sulfur dioxide, Atmospheric Chemistry and Physics, 17, 3879–3889, doi:10.5194/acp-17-3879-2017, 2017.

Weisenstein, D. K., Penner, J. E., Herzog, M., and Liu, X.: Global 2-D intercomparison of sectional and modal aerosol modules, Atmospheric Chemistry and Physics, 7, 2339–2355, doi:10.5194/acp-7-2339-2007, 2007.

Weisenstein, D. K., Keith, D. W., and Dykema, J. A.: Solar geoengineering using solid aerosol in the stratosphere, Atmospheric Chemistry and Physics, 15, 11 835–11 859, doi:10.5194/acp-15-11835-2015, 2015.

Winker, D., Vaughan, M., and Hunt, B.: The CALIPSO mission and initial results from CALIOP, in: Society of Photo-Optical Instrumentation Engineers (SPIE) Conference Series, vol. 6409, 640902, doi:10.1117/12.698003, 2006.

Wiscombe, W. J.: Mie scattering calculations: advances in technique and fast, vector-speed computer codes, Atmospheric Analysis and Prediction Division, National Center for Atmospheric Research, `http://opensky.ucar.edu/islandora/object/technotes%3A232/datastream/PDF/download/citation.pdf`, 1979.

Zanchettin, D., Khodri, M., Timmreck, C., Toohey, M., Schmidt, A., Gerber, E. P., Hegerl, G., Robock, A., Pausata, F. S. R., Ball, W. T., Bauer, S. E., Bekki, S., Dhomse, S. S., LeGrande, A. N., Mann, G. W., Marshall, L., Mills, M., Marchand, M., Niemeier, U., Poulain, V., Rozanov, E., Rubino, A., Stenke, A., Tsigaridis, K., and Tummon, F.: The Model Intercomparison Project on the climatic response to Volcanic forcing (VolMIP): experimental design and forcing input data for CMIP6, Geoscientific Model Development, 9, 2701–2719, doi:10.5194/gmd-9-2701-2016, 2016.

Zhang, X., Zheng, X., Yang, C., and Luo, S.: A new weighting function for estimating microwave sounding unit channel 4 temperature trends simulated by CMIP5 climate models, Advances in Atmospheric Sciences, 30, 779–789, doi:10.1007/s00376-013-2152-x, 2013.